



Balkan Journal of Electrical & Computer Engineering

An International Peer Reviewed, Referred, Indexed and Open Access Journal

www.bajece.com

Vol : 6
No : 1
Year : 2018
ISSN : 2147 - 284X



This journal is supported by the Istanbul Technical University. It is abstracted and indexed in, Index Google Scholarship, the PSCR, Cross ref, DOAJ, Research Bible, Indian Open Access Journals (OAJ), Institutional Repositories (IR), J-Gate (Informatics India), Ulrich's, International Society of Universal Research in Sciences, DRJI, EyeSource, Cosmos Impact Factor, Cite Factor, SIS SIS Scientific Indexing Service, IJIF, iiiFactor. ULAKBİM-TR Dizin.



General Publication Director & Editor-in-Chief
Ş.Serhat Seker, Istanbul Technical University, Turkey

Associate Editors

Abdoulkader Ibrahim Idriss, University of Djibouti, Djibouti
Amir Tokić, University of Tuzla, Bosnia and Herzegovina
Veselina Nedeva, Trakia University, Bulgaria

Scientific Committee

Abhishek Shukla (India)
Abraham Lomi (Indonesia)
Aleksandar Georgiev (Bulgaria)
Arunas Lipnickas (Lithuania)
Audrius Senulis (Lithuania)
Belle R. Upadhyaya (USA)
Brijender Kahanwal (India)
Chandar Kumar Chanda (India)
Daniela Dzhonova-Atanasova (Bulgaria)
Deris Stiawan (Indonesia)
Emel Onal (Turkey)
Emine Ayaz (Turkey)
Enver Hatimi (Kosovo)
Ferhat Sahin (USA)
Gursel Alici (Australia)
Hakan Temeltaş (Turkey)
Ibrahim Akduman (Turkey)
Jan Izykowski (Poland)
Javier Bilbao Landatxe (Spain)
Jelena Dikun (Lithuania)
Karol Kyslan (Slovakia)
Kunihiko Nabeshima (Japan)
Lambros Ekonomou (Greece)
Lazhar Rahmani (Algerie)
Marcel Istrate (Romania)
Marija Eidukeviciute (Lithuania)
Milena Lazarova (Bulgaria)
Muhammad Hadi (Australia)
Muhamed Turkanović (Slovenia)
Mourad Houabes (Algerie)
Murari Mohan Saha (Sweden)
Nick Papanikolaou (Greece)
Okay Kaynak (Turkey)
Osman Nuri Ucan (Turkey)
Ozgur E. Mustecaplioglu (Turkey)
Padmanaban Sanjeevikumar (India)
Ramazan Caglar (Turkey)
Rumen Popov (Bulgaria)
Tarek Bouktir (Algeria)
Sead Berberovic (Croatia)
Seta Bogosyan (USA)
Savvas G. Vassiliadis (Greece)
Suwarno (Indonesia)
Tulay Adali (USA)
Yogeshwarsing Calleecharan (Mauritius)
YangQuan Chen (USA)
Youcef Soufi (Algeria)

Aim & Scope

The journal publishes original papers in the extensive field of Electrical-Electronics and Computer engineering. It accepts contributions which are fundamental for the development of electrical engineering, computer engineering and its applications, including overlaps to physics. Manuscripts on both theoretical and experimental work are welcome. Review articles and letters to the editors are also included.

Application areas include (but are not limited to): Electrical & Electronics Engineering, Computer Engineering, Software Engineering, Biomedical Engineering, Electrical Power Engineering, Control Engineering, Signal and Image Processing, Communications & Networking, Sensors, Actuators, Remote Sensing, Consumer Electronics, Fiber-Optics, Radar and Sonar Systems, Artificial Intelligence and its applications, Expert Systems, Medical Imaging, Biomedical Analysis and its applications, Computer Vision, Pattern Recognition, Robotics, Industrial Automation.



ISSN: 2147- 284X
Vol: 6
No: 1
Year: February 2018

CONTENTS

A. Tarhan, and M.A. Sağ , COSMIC Solver: A Tool for Functional Sizing of Java Business Applications, **1-8**

A.Serbes, A Method for Estimating Chirp Rate of a Linear Frequency Modulated Signal, **9-12**

I.Turker, Evaluation of the Turkish Highway Network Analysis with Traffic Data, **13-19**

O. Coşkun, and K. Avci, FPGA Schematic Implementations and Comparison of FIR Digital Filter Structures, **20-28**

M. A. Şen, and M. Kalyoncu, Optimal Tuning of PID Controller Using Grey Wolf Optimizer Algorithm for Quadruped Robot, **29-35**

S. Muratoğlu Çürük, Performance of MAP Channel Estimator in Power Line Communication with OFDM under Impulsive Noise, **36-41**

N. Ekren, Researches on Anti-reflection Coating (ARC) Methods Used in PV Systems, **42-46**

S. Bircik, Design of Unified Power Quality Conditioner for Power Quality Improvement in Distribution Network, **47-52**

J. Dasedemir, Quaternion-Based Robust Satellite Attitude Tracking Control, **53-61**

A. Ugur, and M. Yilmaz, A GaN-Based Synchronous Buck Converter for High Power Laser Diode Drive Applications, **62-68**

BALKAN JOURNAL OF ELECTRICAL & COMPUTER ENGINEERING
(An International Peer Reviewed, Indexed and Open Access Journal)

Contact
Istanbul Technical University
Department of Electrical Engineering
Ayazaga Campus, Maslak, Istanbul-Turkey

Web: <https://www.bajece.com>
<http://dergipark.gov.tr/bajece>
e-mail: editor@bajece.com

COSMIC Solver: A Tool for Functional Sizing of Java Business Applications

A. Tarhan, and M.A. Sağ

Abstract—Functional Size Measurement (FSM) provides a ground during software project life-cycle to estimate planning parameters and track progress. Since it is time-consuming, costly, and error-prone when functional size is measured manually, automating the process of measurement has come to the fore. The literature includes studies that automate FSM from software artifacts such as requirements specifications, design models, and software code. In this study we focus on automation of FSM from software code, and share our experience towards developing a tool called ‘COSMIC Solver’ for COSMIC FSM of Java Business Applications (JBAs). The tool automates the following steps: (i) Eliciting textual representations of UML sequence diagrams from functional execution traces of a JBA, (ii) tagging of these textual representations with the help of AspectJ technology to measure COSMIC functional size, and (iii) calculating functional size of user scenarios run in the JBA from the information on the tags according to COSMIC FSM rules. In this paper we explain features and measurement method of COSMIC Solver (v1.0), and the share results obtained from functional sizing of an open source JBA by using the tool.

Index Terms—Functional size, function points, automation, tool, COSMIC FSM, software code, UML, sequence diagram, AspectJ.

I. INTRODUCTION

SINCE ALBRECHT introduced the concept of ‘functional size’ as a new dimension to size software products [1], it has been favored important for estimating and tracking cost of software projects [2, 3]. Widely known for its function point (FP) metric, functional size can be measured earlier in project life-cycle and as independent of design technology, programming language, or developer skills. Because of these properties, it provides a solid ground to estimate planning parameters and track progress during software life-cycle. The term Functional Size Measurement (FSM) has emerged and been defined as “the process of measuring software’s functional size derived by quantifying the functional user requirements that describe what the software shall do in terms of tasks and services” [4]. Several FSM methods that have been adopted as ISO standards in the last two decades, which include Mk II FPA

[5], NESMA FSM [6], FISMA FSM [7], IFPUG FSM [8], and COSMIC FSM [9]. FSM can be useful to track software development progress by using earned value based on functional size [10–13]. Earned value enables software practitioners to track the actual value achieved (earned) during the project in comparison to the planned value [14]. Function points, in this regard, is a valuable metric as the base to calculate the planned and earned values as independent of programming language or developer. The benefits of FSM is more prominent in iterative development [15–17] or agile development [18–20], where practitioners can identify the amount of functionality delivered to customer by software releases and create or revise work plans accordingly. FSM of completed products (e.g., software code) can also be useful for software organizations in building their historical size databases, based on which project estimations can be developed. Due to mentioned benefits, FSM is useful for wider and cost-effective adoption of size-based project management practices by software community.

Since it is significant that functional size be measured correctly, timely, and practically, automating the process of FSM has come to the fore as a solution. FSM automation is claimed to minimize human errors and decrease costs [21–23]. A recent survey on FSM based on code [24] reveals that FSM is considered an important tool for decision making in software projects (with agreement of 87% of the respondents). The same survey indicates that FSM automation is perceived as important but difficult to realize, and that automating FSM directly from source code can help measurement specialists and decision makers. These findings show there is awareness in community that FSM is a valuable practice but the means (e.g., methods and tools) to apply it in a useful way, typically as part of daily project routine, are not yet mature enough. Emerging research on automated FSM might be helpful to create the base for effective and efficient (i.e., target-oriented and resource-economic) adoption of FSM, and narrow the gap between software project management theory and practice.

The literature includes studies that automate FSM from early software artifacts such as analysis and design models [25–29] as well as the ones that automate FSM from software code [23, 30–33]. In this study, we focus on automation of FSM from software code. In a previous work of ours [32] covered by a thorough review of studies on this topic [34], we introduced an automation prototype for COSMIC FSM [9] and evaluated its accuracy on a toy application that we developed. In this paper

✉ A. TARHAN, is with Department of Computer Engineering, Hacettepe University, Ankara, Turkey, (e-mail: atarhan@hacettepe.edu.tr) 

M.A. SAĞ, is with Turkish Academic Network and Information Center (ULAKBIM) of the Scientific and Technological Research Council of Turkey (TUBITAK), Ankara, Turkey, (e-mail: muhammetalisag@gmail.com)

Manuscript received August 9, 2017; accepted Dec 21, 2017.

DOI: [10.17694/bajece.401986](https://doi.org/10.17694/bajece.401986)

we explain features and design of an improved version of the prototype which has evolved into a tool called COSMIC Solver (v1.0). We also elaborate on the results from functional sizing of an open source Java Business Application (JBA) using the tool, and from the evaluation of measurement accuracy of the tool with respect to a verification protocol aimed for automated FSM tools [35].

The remainder of this study is organized as follows. Section 2 provides background on COSMIC FSM and AspectJ. Section 3 summarizes related studies by claiming similarities and contribution of our proposal in comparison to theirs. Section 4 explains attributes and user requirements of COSMIC Solver as well as its measurement method and components. Section 5 overviews results from manual and automated functional sizing of the open source JBA, evaluates the results, and highlights opportunities for improving the tool. Finally, Section 6 closes the study by providing general conclusions and plans for future work.

II. BACKGROUND

A. COSMIC FSM method

ISO/IEC 19761 (COSMIC FSM) [9] defines principles and rules to decompose a system into layers, and to size layered software based on a generic software model identifying *functional processes*, *data groups*, and *data movements* in response to *functional user requirements (FURs)*.

Functional processes can be defined as independent data movements of a FUR. A functional process is a series of data movements of four types:

- *Entry (E)* moves a data group from a functional user across the boundary into a functional process;
- *Exit (X)* moves a data group from a functional process across the boundary of the application to a functional user;
- *Read (R)* moves a data group from persistent storage through a functional process; and
- *Write (W)* moves a data group lying inside a functional process to persistent storage.

The COSMIC Function Points (CFP) measurement method states that the number of data movements is proportional to functional size of the measured software [36]. FURs are related with data transfer, transformation, persistence, and data retrieval. Functional process is the base component of a FUR and is triggered by events (i.e., an Entry data movement) that take place in user's world. It then executes in response to the triggering event. A functional process includes an Entry data movement and either a Write or an Exit data movement – i.e., it includes at least two data movement types. Each data movement in a functional process is counted as one CFP.

COSMIC FSM method [36] defines three measurement phases as we explain in the following paragraphs.

(1) In *Measurement Strategy Phase*, the purpose and the scope of measurement, functional users of the application to measure, and the level of granularity of measurement are specified. The purpose clarifies why the measurement is done and for which reason its results will be used. Specification of

measurement purpose is also important for identifying the scope and the functional users. Scope means the requirements of the functional users who will be incorporated into the measurement. Functional users are the users who receive or send data for a software unit in the defined FURs. Finally, the level of granularity indicates the detail level at which the measurement will be done. Measurements should be made at the same granularity level to compare with each other.

(2) In *Mapping Phase*, event masses (i.e., functional processes) that are triggered by the user are identified. Then, data groups and data qualifications related with these processes are determined. A data group is the data that provides same *object of interest* with a holistic view and that clusters for an ad hoc query. If the query interacts with multiple object of interests, number of all interacted object of interests will be taken into account in calculating CFP.

(3) In *Measurement Phase*, data movements are detected for all functional processes, the measurement function is implemented, and the results are consolidated. Sub-processes consist of data movements and data manipulations. Data manipulations are not taken into account within the scope of COSMIC FSM method. The total size is calculated by consolidating the data movements. While calculating the consolidated size; if the same level of granularity is used for measurement, the values obtained on the basis of functional processes are summed mathematically. Otherwise, they are added after they are scaled to the same level.

B. Aspect-oriented programming and AspectJ

Typical enterprise and web applications today have to address 'concerns' as security, transactional behavior, and logging. The subsystems that provide these services can be implemented in a modular way. However, to use these services, the duplicate code fragments must be inserted into various places in the application to invoke them. For example, to produce logs for certain operations in an application, log writing procedures must be inserted into the beginning of every method as needed. Aside from the redundancy issue, it would be difficult and error-prone to modify or replace this logging approach later, should that become necessary. In addition, the application code is mixed up with the code for logging concern, which both compromises clarity and makes it hard to reuse the code in another context.

To solve mentioned problems, Aspect-Oriented Programming (AOP) was proposed [37]. AOP addresses the 'cross-cutting concerns' that compromise the modularity of object-oriented systems by modularizing the concerns as aspects and by providing mechanisms to combine aspect and object modules to compose applications [37, 38]. Concerns (or *crosscutting concerns*) like logging or authentication, typically cut across a number of application module boundaries (e.g., classes). That is, the points of intersection are defined once, in one place, making them more understandable, rectifiable, and usable. The other modules require no modifications to be advised by the aspects.

It is important to explain four terms in AOP [38] as the key to our solution in this study:

- *Join point* is a well-defined point in the execution of an application.
- *Pointcut* is a way of specifying a join point by means of configuration or code. Pointcuts allow a programmer to specify join points (in the execution of a program like method call, object instantiation, or variable access) in program flow.
- *Advice* is a way of expressing a cross cutting action that needs to occur. Advices allow a programmer to specify code to run at a join point matched by a pointcut.
- *Weaving* consists of executing the aspect advice to produce only a set of generated classes that have the aspect implementation code woven into it [38].

The implementation of AOP in Java environment is enabled by AspectJ as a seamless extension to Java. AspectJ is designed to encapsulate the previously mentioned crosscutting concerns and thereby restore overall system modularity. These concerns or aspects are identified, modularized, independently developed, and then combined with the main object model in a structured way to compose the application through weaving [39]. AspectJ performs weaving during program compilation or load time. In our proposal, we use load-time weaving (LTW) which presents an opportunity to work with byte code. As a result, even though the source code is unreachable, we could perform weaving operations with LTW. AspectJ LTW technology is using ‘java agent’, which holds the key to monitoring and profiling ‘Java Virtual Machine’, and is able to modify Java classes dynamically as they are being loaded.

While weaving target application at runtime, ‘pointcuts’ catch specified signature and ‘advices’ decide what to do after the catch. AspectJ divides an advice into three sections according to its runtime: The one that runs *before* its join point, the one runs *after* its join point, and the one that runs in the exact place of (or *around*) its join point. While generating sequence diagrams, the use of ‘before’ and ‘after’ advices are sufficient in our measurement method. In other words, the actions in advices are being performed before and after the specified ‘join point’. With qualified pointcuts, javaagent, and AspectJ technology, we can catch and tag the candidate functional processes at runtime.

III. RELATED WORK

In this section we summarize related studies that inspired our proposal in certain features, and highlight similarities and contribution of our proposal in comparison to theirs. Interested readers may refer to [34] for a wider set of studies on FSM automation from software code.

Kusumoto et al. [40] refer to traditional functional size calculations and evaluate the possibility of automatic calculation of function points from source code by applying statistical analysis. By focusing on screen transitions, the authors propose a method that counts data and transaction functions of web applications. The study demonstrates the feasibility of automated measurement of function points from source code within IFPUG measurement program, and shows that UML models can be successfully used for FSM. Bévo et al. [25] map the concepts in UML class diagrams and use case diagrams onto the abstractions of COSMIC FSM model to

measure functional size based on high-level specifications of software. Jenner [41] discusses the granularity aspect of use cases in the proposal of Bévo et al [25]. Each functional process is represented by a sequence diagram as an adequate abstraction level of a use case. Both of these proposals focus on finding an appropriate mapping between UML model elements and FSM concepts. Levesque et al. [26] also apply COSMIC FSM method to measure functional size from use case diagrams and sequence diagrams. The authors group functional processes in two categories as data movement and manipulation types, and focus on the deduction of COSMIC functional size by using actor-object flow diagrams while considering UML message exchanges.

In our proposal, we have been inspired by the studies of Jenner [41] and Lévesque et al. [26], which show the feasibility of mapping between sequence diagrams and COSMIC FSM concepts. According to Lévesque et al. [26], data movements can be mapped to messages in a UML sequence diagram and consequently, it becomes easy to calculate the functional size by aggregating all messages exchanged in the sequence diagram.

Our proposal is also in parallel with Kusumoto et al.’s proposal [40] that is considered successful yet having lack of elasticity in being generic. We offer a more flexible and adaptable method in getting the sequence diagrams with the help of aspect-orientation and AspectJ technology.

Bévo et al. [25] and Jenner [41], on the other hand, provide different interpretations of a functional process because the concept of a ‘triggering event’ is not explicitly presented in UML. Triggering event problem is widely known in UML assisted FSM methods, and our proposal handles this problem by finding and tagging the methods of user interface components in the mapping phase of automated measurement. In addition, source code or binary code of JBAs can be taken as input to our proposal for calculating CFP.

IV. COSMIC SOLVER

COSMIC Solver is aimed to automate FSM from software code of JBAs in accordance to COSMIC FSM method [9]. In the following sub-sections, we provide an overview of COSMIC Solver with respect to attributes and user requirements that we see critical for automation, and explain the details of automated measurement.

A. Attributes and User Requirements

In a recent study involving the first author [34], a set of attributes have been proposed for automating COSMIC FSM from software code based on previous experiences. The proposed attributes are trigger handling, functional process identification, external interface definition, data persistence interface definition, data group identification, domain class identification, scope identification, and technology identification. These attributes are described in Table I together with any support by the current implementation (v1.0) of COSMIC Solver. Most of the attributes are supported by the tool, and the only missing attribute is domain class identification. In addition, functional process identification and data group identification are embedded in automation software and cannot be tailored by measurer.

TABLE I.
ATTRIBUTES OF COSMIC SOLVER FOR FSM AUTOMATION FROM SOFTWARE CODE

Attribute	Description	Support by COSMIC Solver (v1.0)
Trigger handling	The specific identification of triggering events that start functional processes.	√
Functional process identification	The identification of a functional process which is a unique, cohesive and independently executable set of data movement types.	√
External interface (E/X) definition	The identification of external interfaces where information is exchanged with functional users, and which will be used to catch Entry and Exit data movements.	√
Data persistence (R/W) interface definition	The identification of data persistence interfaces, which will be used to catch Read and Write data movements.	√
Data group identification	The identification of a data group that is a set of attributes that describe particular aspect of an object of interest.	√
Domain class identification	The identification of objects that are of interest to its functional users (i.e., domain classes) and the exclusion of classes that are implemented for only design purposes.	
Scope identification	The identification of measurement boundary and the selection of functional user requirements to measure.	√
Technology identification	The identification of specific architecture and technology of target applications.	√

User requirements of COSMIC Solver to measure the functional size of a JBA are shown in Fig. 1 by a UML use case diagram that includes three main use cases: (1) Export Pointcuts, (2) Compile and Run Pointcuts, and (3) Calculate CFP. The last use case further includes four use cases, which are Parse Sequence, Process Sequence, Find Duplicate Sequences, and Find Conflicted Sequences, executed internally by the tool. The ‘sequence’ here indicates a number of data movements that make up a functional process. The first two use cases, “Export Pointcuts” and “Compile and Run Pointcuts”, serve for preparing the pointcuts for CFP calculation, and should be carried out consecutively prior to execution of the third use case “Calculate CFP”. In addition, while the third use case is typically executed by a Standard User who wants to size a JBA, the first two use cases should be carried out by a Measurement Specialist who has knowledge about Java, AspectJ, and COSMIC FSM method.

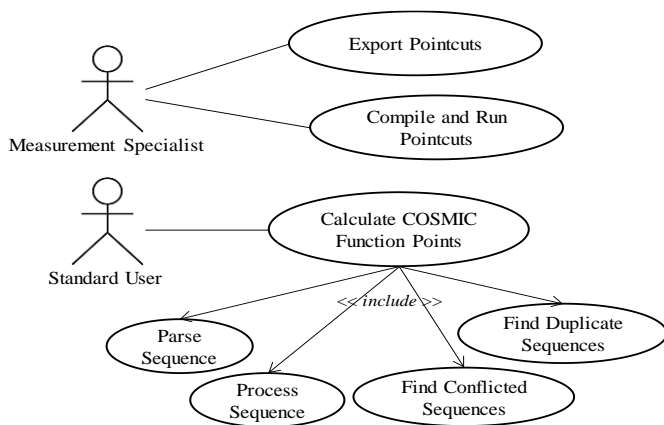


Fig. 1. User Requirements of COSMIC Solver by a UML Use Case Diagram

B. Measurement Method

We use black-box approach to automate FSM from source or binary code of a two- or three-tier JBA without a need to modify its code. A two- or three-tier architecture means a client-server architecture in which the presentation, the application

processing and the data management are logically separate processes. We identify and presume a constant mapping between technology elements of the JBA and the COSMIC FSM data movements, but we enable some degree of tailoring for the measurer based on selected technologies.

The tool first elicits textual representations of user scenarios from functional execution traces of a JBA, which correspond to sequence diagrams in Unified Modeling Language (UML). It then tags these textual representations of execution traces by considering four data movement types (Entry, Exit, Read, and Write) in COSMIC FSM method with the help of AOP concepts, more specifically by using AspectJ technology. It finally calculates functional size of the user scenarios executed at runtime from their tagged representations.

The phases and components of the automated measurement process are shown in Fig. 2. As it is seen from the figure, COSMIC Solver has two components, which are *Tracer* and *Calculator*. ‘Tracer’ component retrieves sequence diagrams during dynamic execution of a JBA with the help of AspectJ. ‘Calculator’ component, on the other hand, applies COSMIC FSM rules to calculate the function points.

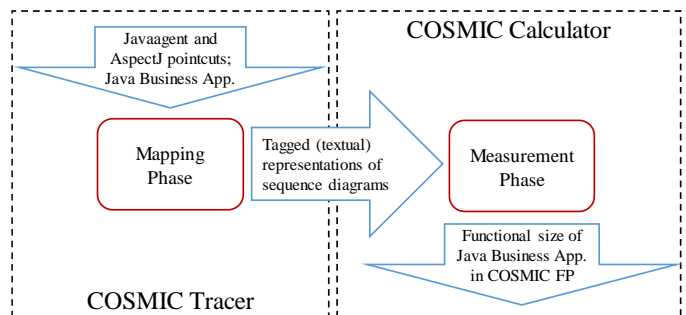


Fig. 2. Phases of Automated Measurement Process

We use AspectJ technology and related concepts of pointcuts and advices in order to set and observe the stated mappings, and allow the measurer to revise the pointcuts which are indeed the basic constructs for observing data movements in candidate

functional processes. The pointcuts are created statically in the measuring software which then monitors the JBA and calculates its functional size at runtime. AspectJ catches execution traces of user scenarios and transform these traces into behavioral specifications by tagging. Tagging is performed to prepare the execution traces of the scenarios for measuring CFP according to COSMIC FSM rules. Once the traces are transformed into textual specifications, CFP is automatically calculated at runtime for the executed user scenarios.

1) *COSMIC Tracer*

Tracer component provides a useful framework to capture interactions (messages) between classes while executing functional processes. To do that, it uses ‘before’ and ‘after’ advices and pre-defined ‘pointcuts’. Almost half of the measurement operation is implemented via this component. Tracer component captures all join point executions and calls, in order to construct the structured text versions of sequence diagrams. These executions and calls use some specific method signatures to get neat and optimal sequence diagrams which do not contain every system call and execution but include only required ones that belong to developer space.

In order to get textual representations of sequence diagrams with tags (e.g., SWING, DIALOG, JDBC) for specifying entry points, dialog box operations, database calls, and etc., we use specific method signatures and object references. For example, to catch JDBC operations we use two pointcut patterns as:

```
execution(* java.sql.Statement.exec*(..))
call(* java.sql.Statement.exec*(..))
```

Apparently, a JBA can contain function types other than the ones specified. To handle them, appropriate pointcuts should be defined in Tracer component, which is possible by extending its current implementation. Then, with the help of advices, specified tags could be appended to support the identification of data movement types; and a piece of code, which constitutes an advice, runs at defined join point that is picked out by the related pointcut.

Kind of an advice determines the behavior of the running code, and how it interacts with the join point. Using these advices before and after every call/execution, we can intercept processes. Then, we call a specific function to write the method signature as shown in Table II (a). These advices produce output archetypes given in Table II (b).

TABLE II.
‘BEFORE’ & ‘AFTER’ ASPECT ADVICES AND TRACE LOG

(a) Advices	<pre>before() : jdbcCall() jdbcExecution() { [Start: {tag}>] <print signature> } after() : jdbcCall() jdbcExecution() { [End: {tag}>] <print signature> }</pre>
(b) Trace Log	<pre><Start:tag>> returnType PackageName. ClassName. MethodName([Parameters]) [(if exist)SQL Statement] <End:tag>> returnType PackageName. ClassName. MethodName([Parameters])</pre>

As a result, for every user interaction on target JBA, a textual and tagged representation of a sequence diagram is generated with the help of pointcuts and advices. The generated sequence

diagram has tree style; in which every node has ‘Start’ and ‘End’ tags and might contain another method call or execution. This information is processed with Calculator component to identify functional size in CFP.

2) *COSMIC Calculator*

Calculator component calculates functional size of the JBA by applying COSMIC FSM rules to tagged (textual) representations of UML sequence diagrams. The basic steps to calculate CFP are (1) Analyze Candidate FURs, (2) Identify Application Boundary, (3) Evaluate Functional Processes, and (4) Calculate CFP. We explain the key points for each in the following paragraphs.

(1) While generating sequence diagrams, there may be multiple interactions with the same functional processes. This brings out duplicate sequences that should be ignored. Occasionally, some functional processes might have the same trigger but different flows. This causes a more complicated problem than duplication. If there is a situation like that the functional size is measured by an approximation approach.

(2) Application boundary indicates the border between the JBA being measured and external applications or user domain. It determines which functions will be included or not in counting the function points. To deal with ‘triggering event’ problem, we specify user interface components of the target application and search for specific method signatures. For example, if an application uses Swing or AWT libraries for user interface, we define events via these interface components as the starting points of functional processes.

(3) The COSMIC FSM method states that a FUR is considered as a functional process if it is independently executable and triggered by an event in the world of functional users. Using the tags and COSMIC FSM rules, we identify if a user operation initiates and leads to a functional process.

(4) For each functional process identified, data movement types are also detected from the tags. CFP is then calculated by summing the number of data movements for all functional processes in all FURs.

V. FSM OF AN OPEN SOURCE JBA

Measurement validity of COSMIC Solver was initially tested for its prototype on a toy (personnel and payment database) application, and it was found that manual and automated measurement results were very convergent with an error rate of 1/32 [32]. After the prototype has been evolved into a tool with some generic features such as creating and compiling pointcuts, we aimed to evaluate the performance of COSMIC Solver on an open source JBA that meets measurement constraints of the tool. Consequently, we performed a case study to answer the following research questions (RQs):

- RQ-1: How effective is COSMIC Solver in measuring CFP of an open source JBA?
- RQ-2: How efficient is COSMIC Solver in measuring CFP of the JBA in comparison to manual measurement?

The steps that we followed to answer these RQs are explained in the sub-sections below.

A. Application Selection and Information Gathering

We searched for JBAs in the open source software repositories such as GitHub, SourceForge and Google Code, and identified candidate applications that meet the measurement constraints of COSMIC Solver.

More specifically, we checked the following criteria: The application has been developed in Java programming language and by using Java Platform, Standard Edition (Java SE) 1.5 or later; the application has a two- or three-tier software architecture; the user interface layer of the application has been developed using Java Swing; the application is rich in Create, Read, Update, Delete, and List (CRUDL) operations; the libraries used by the application are compatible with the standards of Java API for XML-based RPC (JAX-RPC), JPA, and JDBC; and the application conforms to the principles of the Software Context Model and Software Generic Model defined in Appendix D of COSMIC FSM method [36].

TABLE III.
PROPERTIES OF NYAGUA AQUARIUM MANAGEMENT JBA

Operation Platform	Runs on every O.S. that can run Java applications
Licence	It has GNU GPL v.2 licence; it can be freely used.
Java Version	Java SE 1.7
GUI	Java Swing
Database	SQLITE
JDBC/Persistence	Native JDBC
JDBC URL	jdbc:sqlite://localhost/<file>
Dev. Platform	NetBeans Standard IDE
Libraries Used	sqlite-jdbc-3.7; Jcalendar – 1.4; JDK 1.7

Among the candidate applications identified according to these criteria, we selected ‘Nyagua Aquarium Management Application’ in the SourceForge repository. General and technical properties of the application, which best satisfied expected criteria, are shown in Table III. The application has its source code and no other documents in the repository. Therefore, manual identification of functional processes and CFP measurement were done by navigating use cases of the application at runtime, and reviewing its source code.

B. Manual and Automated Measurement Results

To frame and equate the scopes of manual and automated measurements, we navigated user interfaces of the Nyagua Aquarium JBA prior to measurement, and identified use case groups (FURs) and objects of interest candidate for COSMIC FSM. As a result, we selected 12 FURs for functional sizing to verify operational performance of COSMIC Solver.

An expert who succeeded COSMIC foundation examination manually measured CFP of Nyagua Aquarium JBA in the framed scope, and recorded manual measurement effort. Then, we automatically measured CFP of the JBA for the same scope by using COSMIC Solver, and recorded the duration of automated measurement. Table IV summarizes manual and automated measurement results. Manually measured size was 356 CFP regarding 76 functional processes identified in 12 FURs targeted for FSM, and duration of manual measurement was 6 hours. For automated measurement, we ran 12 FURs in the framed scope, and calculated COSMIC functional size as 273 CFP regarding 49 functional processes identified

automatically by COSMIC Solver in almost 30 minutes. The duration of automated measurement included the time for preparing the application for automated measurement (e.g., creating and compiling the pointcuts, and transforming the application to include AspectJ features).

TABLE IV.
RESULTS OF MANUAL AND AUTOMATED MEASUREMENTS

	Manually	Automated
FURs measured	12 FURs	12 FURs
Functional Processes identified	76 Func.Proc.	49 Func.Proc.
CFP measured	356 CFP	273 CFP
Duration of measurement	6 hours	½ hours

C. Evaluation of Results

We compared the results of manual and automated measurements by following a verification protocol proposed by Soubra et al. [35] for tools that automate COSMIC FSM method [9]. The aim of the protocol is to ensure that the whole measurement chain produces the right measurement results. According to the protocol, measurement accuracy of a tool is verified in three phases. *Phase-1* requires a comparison of measurement results (i.e., CFP) calculated by tool and obtained manually. *Phase-2* requires a detailed comparison of these results (e.g., at levels of functional processes and data movement types) to understand reasons of deviations, if any. *Phase-3* requires verification of automation tool and inputs to determine which module of the tool is responsible for error.

In Phase 1 of the protocol, we compared the results of manual and automated measurements. We found that in the former we measured 356 CFP while in the latter COSMIC Solver calculated 273 CFP, which resulted in an automation accuracy rate of 77%. This is less than 94% in [23] and 92% in [31], both requiring measurement code insertion into JBA, and 81% in [33] that does not handle triggering events. Since our tool measures CFP from the JBA as is without a need for code insertion and handles the triggering events, we consider its rate successful as an initial result on a third party JBA.

In Phase 2 of the protocol, we compared the number of functional processes and data movements and found that neither of them were identical. The number of functional processes identified was 76 in manual measurement and 49 in automated measurement. Table V shows the FURs and objects of interest in the sample frame, together with numbers of functional processes and CFP values that were measured manually and by using the tool. As observed from the table, the manual and automated numbers of functional processes or CFP values showed deviation for each FUR.

In Phase-3 of the protocol, we investigated the reasons of these deviations. From the logs of manual and automated measurements it was clear that Tracer component was only partially effective in tagging the manually identified functional processes. This was mainly because: (i) we could not define all pointcuts to handle the variety in the triggering events (e.g., for retrieving hidden objects of interest), and (ii) Tracer component could not identify different functional processes started by the same triggering event. These findings indicated a need for reviewing and improving the mapping phase of the automation, especially for the pre-defined pointcuts.

TABLE V.
USE CASE GROUPS, OBJECTS OF INTEREST, AND FUNCTIONAL PROCESSES FOR COSMIC FSM

Use case group (FUR) No	Object of Interest	# Functional Processes		Calculated CFP		Manually Calculated CFP for Automatically Identified Functional Processes
		Manual	Automated	Manual	Automated	
1	Aquarium	4	4	18	18	15
2	Maintenance	6	4	29	21	21
3	FishBase	7	4	30	24	17
4	InvertBase	7	4	30	27	21
5	PlantBase	7	4	30	24	21
6	Fish	7	4	34	16	23
7	Plant	7	4	34	16	23
8	Inverts	7	4	34	16	23
9	Expense	6	4	49	30	24
10	Reading	5	4	22	16	19
11	Device	7	4	25	16	16
12	Schedule	6	5	21	37	15
TOTAL		76	49	356	273	238

To understand the reasons of deviations in the level of data movement types, we also manually calculated CFP values in the scope of automatically identified functional processes, as shown in the rightmost column of Table V. The totals of manually and automatically measured CFP values in this narrowed scope were closer (238 and 273 with an automation accuracy rate of %85) but still not equal. This finding implied that there were also deviations in the types or numbers of the data movements identified. When we checked the logs of manual and automated measurements we noticed that for the same functional processes, a greater number of Read and Exit data movements were identified in some cases (e.g., for retrieving objects of interest that were part of the main ones, and returning error messages or reports) in manual measurement. In some other cases, however, Calculator component counted a greater number of Entry and Exit data movements, which was led by redundant tagging via Tracer component.

Based on the findings and related investigations mentioned above, we identified the following opportunities for improving COSMIC Solver at the end of the case study implementation:

- Pointcuts pre-defined in COSMIC Solver (SWING, JDBC, JPA, DIALOG, JAX-RPC) should be revised and extended to catch additional function types (e.g., standard file read/write operations, and seldom used Swing components);
- Tracer component should be revised to handle: (i) different functional processes initiated by the same triggering event, (ii) hidden objects of interest that are part of the main ones (e.g., aquarium image); and (iii) redundant tagging of Entry/Exit data movements.

D. Potential Threats to Validity

There is a number of validity threads to discuss for the case study implementation, as suggested by Yin [42]. *Construct validity* is related to identifying correct operational measures and avoiding subjective judgements. We followed COSMIC FSM method [36] in measurements and used a three-stage verification protocol [35] to cope with subjectivity. *Internal validity* requires seeking to establish a causal relationship as distinguished from a spurious one. The fact that the second author who developed COSMIC Solver participated in the case study can be considered an internal thread, and its effect on evaluation was mitigated by supervision of the case study by the first author and also by manual measurement of CFP by a

COSMIC FSM expert. *External validity* is about defining the context to which a study's findings can be generalized. We cannot yet argue that COSMIC Solver would be effective and efficient in FSM of other JBAs, and we plan further studies to deal with this threat. As the last test, *reliability* is related to repeatability of the operations in a case study, which is possible by following the steps in sub-sections 5.A thru 5.C.

VI. CONCLUSION

The progressing state of FSM in software industry reveal the utmost importance of its automation. Consequently, in this article we focused on automated measurement of CFP from software code of JBAs. We introduced a tool called COSMIC Solver, presented the results of a case study on evaluating the performance of the tool from sizing of an open source JBA, and identified opportunities for improving the tool.

For the case study, we identified two research questions. RQ-1 was related to the effectiveness of COSMIC Solver in measuring CFP of the JBA. The evaluation results showed that CFPs measured manually and automatically were convergent by 77%. This indicated that COSMIC Solver was effective in functional sizing of the JBA when compared to the features and success rates of the previous proposals (e.g., [23], [31] and [33]). The RQ-2 was related to the efficiency of the tool in measuring CFP in comparison to manual measurement. The durations recorded during manual and automated measurements were 6 hours and 30 minutes, respectively. Therefore, COSMIC Solver was 12 times more efficient than manual measurement in functional sizing of the JBA.

In future work, we plan to revise the current version (1.0) of the tool by considering improvement opportunities identified by the case study, and the requirements of Automated Function Points specification [43]. We also plan to perform further case studies, especially to cope with the validity threads regarding the generalizability of the automated measurement results and the independence of the measurer.

ACKNOWLEDGMENT

The authors thank Onat Ege Adalı for manual functional sizing of Nyagua Aquarium Management Application.

REFERENCES

1. Albrecht AJ (1979) Measuring application development productivity. In: IBO Conf. Appl. Dev. pp 83–92
2. Jones C (2004) Project Management Practices : Success versus Failure. Crosstalk 5–9.
3. Jorgensen M, Shepperd M (2007) A Systematic Review of Software Development Cost Estimation Studies. IEEE Trans Softw Eng 33:33–53. doi: 10.1109/TSE.2007.256943
4. ISO/IEC (2011) ISO/IEC 14143/1: Information technology – software measurement – FSM. Part 1 Definition of concepts.
5. ISO/IEC (2002) ISO/IEC 20968: Software engineering - Mk II Function Point Analysis - Counting Practices Manual.
6. ISO/IEC (2005) ISO/IEC 24570: Software engineering - NESMA functional size measurement method version 2.1 - Definitions and counting guidelines for the application of Function Point Analysis.
7. ISO/IEC (2008) ISO/IEC 29881: Information technology – Software and systems engineering – FiSMA 1.1 functional size measurement method.
8. ISO/IEC (2009) ISO/IEC 20926: Software and systems engineering - Software measurement - IFPUG functional size measurement method.
9. ISO/IEC (2011) ISO/IEC 19761: Software engineering - COSMIC: A functional size measurement method.
10. Brandon DM (1998) Earned Value Easily and Effectively. Proj. Manag. J. 29:2
11. Garcia CAL, Hirata CM (2008) Integrating functional metrics, COCOMO II and earned value analysis for software projects using PMBoK. In: Proc. 2008 ACM Symp. Appl. Comput. - SAC. p 820
12. Jin-hua L, Chang-jiang W, Jing L, Qiong L (2008) Earned value project management of model-centric software development. In: Wirel. Commun. Netw. Mob. Comput. WiCOM '08. 4th Int. Conf. pp 1–4
13. Lu X, Bai X, Wang S (2008) Earned value analysis for software project based on function point method. In: 2nd Int. Conf. Manag. Sci. Eng. Manag. pp 301–308
14. Fleming Q, Koppelman J (1998) Earned Value Project Management. CROSSTALK J Def Softw Eng 19–23. doi: 10.1016/j.drudis.2010.11.015
15. Pow-sang JA, Jolay-vasquez E (2006) An Approach of a Technique for Effort Estimation of Iterations in Software Projects. In: Proc. 20th Asia-Pacific Softw. Eng. Conf. pp 367–376
16. Balbin D, Ocrosopoma M, Soto E, Antonio Pow-Sang J (2009) TUPUX: An Estimation Tool for Incremental Software Development Projects. In: AST 2009 Int. E-CONFERENCE Adv. Sci. Technol. Proc. pp 39–43
17. Pow-sang JA, Imbert R (2012) Effort Estimation in Incremental Software Development Projects Using Function Points. In: Comput. Appl. Softw. Eng. Disaster Recover. Bus. Contin. pp 458–465
18. Hussain I, Kosseim L, Ormandjieva O (2010) Towards Approximating COSMIC Functional Size from User Requirements in Agile Development Processes Using Text Mining. In: Proc. Nat. Lang. Process. Inf. Syst. 15th Int. Conf. Appl. Nat. Lang. to Inf. Syst. pp 80–91
19. Santana C, Leoneo F, Vasconcelos A, Gusmão C (2011) Using Function Points in Agile Projects. In: Agil. Process. Softw. Eng. XP. pp 176–191
20. Hussain I, Kosseim L, Ormandjieva O (2013) Approximation of COSMIC functional size to support early effort estimation in Agile. Data Knowl Eng 85:2–14. doi: 10.1016/j.datak.2012.06.005
21. Robiolo G (2011) How Simple is It to Measure Software Size and Complexity for an IT Practitioner? Online Inf Rev 33:40–48.
22. Akca AA, Tarhan A (2013) Run-time measurement of COSMIC functional size for Java business applications: Is it worth the cost? In: Proc. - Jt. Conf. 23rd Int. Work. Softw. Meas. 8th Int. Conf. Softw. Process Prod. Meas. IWSM-MENSURA 2013. pp 54–59
23. Gonultas R, Tarhan A (2015) Run-Time Calculation of COSMIC Functional Size via Automatic Installment of Measurement Code into Java Business Applications. In: Softw. Eng. Adv. Appl. (SEAA), 2015 41st Euromicro Conf. pp 112–118
24. Huijgens H, Bruntink M, Van Deursen A, et al (2016) An Exploratory Study on Functional Size Measurement based on Code. In: Int. Conf. Softw. Syst. Process. pp 56–65
25. Bévo V, Lévesque G, Abran A (1999) Application de la méthode FFP à partir d'une spécification selon la notation UML : COMPTE RENDU DES PREMIERS ESSAIS D'APPLICATION ET QUESTIONS. In: Proc. 9th Int. Work. Softw. Meas. pp 230–242
26. Levesque G, Bevo V, Cao DT (2008) Estimating software size with UML models. In: Proc. C3S2E Conf. pp 81–87
27. Lavazza L, Del Bianco V (2009) A case study in COSMIC functional size measurement: The rice cooker revisited. In: LNCS 5891. pp 101–121
28. Fehlmann TM, Kranich E (2011) COSMIC Functional Sizing based on UML Sequence Diagrams. In: Proceedigns Metr. 2011. p 16
29. Bianco V, Lavazza L, Liu G, Morasca S (2013) Model-based Simplified Functional Size Measurement – an Experimental Evaluation with COSMIC Function Points. In: Proc. EESSMOD/MODELS. pp 13–22
30. Ho VT, Abran A (1999) A Framework for Automatic Function Point Counting from Source Code. In: Proc. IWSM. pp 249–255
31. Akca AA, Tarhan A (2012) Run-time Measurement of COSMIC Functional Size for Java Business Applications: Initial Results. In: 2012 Jt. Conf. 22nd Int. Work. Softw. Meas. 2012 Seventh Int. Conf. Softw. Process Prod. Meas. pp 226–231
32. Sag MA, Tarhan A (2014) Measuring COSMIC software size from functional execution traces of java business applications. In: Proc. - 2014 Jt. Conf. Int. Work. Softw. Meas. IWSM 2014 Int. Conf. Softw. Process Prod. Meas. Mensura 2014. pp 272–281
33. Demirel H, Özkan B (2015) Üç Katmanlı Nesne-İlişkisel Eşleme Mimarisi İçin Otomatik Fonksiyonel Büyüklük Ölçümü (Automated Functional Size Measurement for Three-Tiered Architecture Object-Relational Mapping) - in Turkish. In: Proc. 9th Natl. Softw. Eng. Symp. (9. Ulus. Yazılım Mühendisliği Sempozyumu -UYMS). pp 242–256
34. Tarhan A, Baris O, Icoz GC (2016) A Proposal on Requirements for COSMIC FSM Automation from Source Code. In: Iwsm-Mensura, 5-7 Oct 2016, Berlin. pp 195–200
35. Soubra H, Abran A, Ramdane-Cherif A (2014) Verifying the accuracy of automation tools for the measurement of software with COSMIC - ISO 19761 including an AUTOSAR-based example and a case study. Proc - 2014 Jt Conf Int Work Softw Meas IWSM 2014 Int Conf Softw Process Prod Meas Mensura 2014 23–31. doi: 10.1109/IWSM.Mensura.2014.26
36. Abran A, Fagg P, Woodward C (2015) The COSMIC Functional Size Measurement Method, Version 4.0.1. 98.
37. Kiczales G, Lamping J, Mendhekar A, et al (1997) Aspect Oriented Programming. In: Akçsit M, Matsuoka S (eds) Proc. 11th Eur. Conf. Object-Oriented Program. Springer Berlin Heidelberg, Berlin, Heidelberg, pp 220–242
38. Wang Y, Zhao J (2007) Specifying pointcuts in AspectJ. In: Proc. - Int. Comput. Softw. Appl. Conf. pp 5–10
39. Paton K (1999) Automatic Function Point Counting Using Static and Dynamic Code Analysis. In: Int. Work. Softw. Meas. p 6
40. Kusumoto S, Imagawa M, Inoue K, et al (2002) Function point measurement from Java programs. In: Proc. Int. Conf. Softw. Eng. pp 576–582
41. Jenner MS (2001) COSMIC-FFP 2.0 and UML: Estimation of the Size of a System Specified in UML - Problems of Granularity. In: Proc. 4th Eur. Conf. Soft. Meas. ICT Control. pp 173–184
42. Yin RK (2013) Case Study Research: Design and Methods. Sage Publications, Inc; 5th ed.
43. OMG (2014) Automated Function Points (AFP). 32.

BIOGRAPHIES



AYÇA TARHAN received the B.S. and M.S. degrees in computer engineering from Ege University in 1995 and from Dokuz Eylül University in 1999, and the Ph.D. degree in information systems from Informatics Institute of Middle East Technical University (METU) in 2006.

She was a visiting researcher in 2013–2015 in the Department of Industrial Engineering and Innovation Sciences of Eindhoven University of Technology. Her research interests include internal and external software quality, software metrics, software development methodologies, process maturity, and business process management. Since 2007, she has been working as a Lecturer and an Assistant Professor in Computer Engineering Department of Hacettepe University in Ankara, Turkey.



MUHAMMET ALİ SAĞ received the B.S. and M.S. degrees in computer engineering from Hacettepe University in 2010 and 2014. In 2010–2012, he worked as a software engineer and researcher in Software Technologies Research Institute of the Scientific and Technological Research Council of Turkey (TUBITAK).

Since 2012, he has been working as a system engineer and researcher in Turkish Academic Network and Information Center (ULAKBIM) of TUBITAK.

A Method for Estimating Chirp Rate of a Linear Frequency Modulated Signal

A. Serbes

Abstract—This paper proposes a fast and accurate chirp-rate estimation algorithm in noisy environment. The proposed method searches the inverse maximum magnitude of the angle-sweep fractional Fourier domain and finds the optimum angle, which provides an estimate for the chirp-rate. In order to accelerate the search process, we propose to use the Fibonacci search algorithm, which provides a sub-optimal search scheme in terms of computational complexity. Simulation results show the efficiency of the proposed algorithm.

Index Terms—Fractional Fourier transform, chirp-rate, linear frequency modulated signals, estimation, Cramer-Rao lower bound.

I. INTRODUCTION

LINEAR frequency modulated (LFM) signals are employed in a relatively diverse areas, such as radar [1], sonar [2], automotive [3], aerospace [4], ultrasound [5], and communications [6]. One of the most important problems when dealing with LFM signals is to estimate one, or all of its parameters. An LFM signal in a noisy environment can be modeled as

$$c(t) = A \exp[j\pi(mt^2 + 2f_0t)] + w(t), \quad (1)$$

where m is the chirp rate, f_0 is the frequency-shift, and A is the complex amplitude. In this problem, the noise $w(t)$ is assumed to be a complex circular additive white Gaussian with variance σ_w^2 .

Radar return signals of a moving object can be modeled by an LFM signal. Therefore, estimating chirp rates of the radar signals provide an estimate of the relative velocity of the target. Moreover, LFM CW radars emit LFM-type signals in order to estimate both velocity and the distance at the same time. Therefore, estimating the chirp-rate of an LFM signal play a critical role in many applications. The asymptotic Cramer-Rao lower bound for estimating the chirp rate of a single LFM signal can be expressed by

$$\text{var}(\hat{m}) = \frac{90}{\pi^2 N^5 T_s^4 \gamma}, \quad (2)$$

where \hat{m} is the estimated chirp rate and γ is the signal-to-noise ratio (SNR).

A. SERBES, is with Department of Electronics and Communications Engineering of Yildiz Technical University, Istanbul, Turkey, (e-mail: aserbes@yildiz.edu.tr) 

Manuscript received August 16, 2017; accepted Dec 23, 2017.
DOI: 10.17694/bajece.369239

Here, the LFM signal sampled with a sampling period T_s and N samples are taken. The maximum likelihood estimators [7-8] for estimating parameters of the LFM signal requires a multi-dimensional parameter search algorithm in the search space. Therefore it is computationally inefficient. Wigner distribution-based methods [9-10] are also of high performance; however they also lack computational ease. Maximum amplitude method [11] can also be used to estimate the chirp rate of a signal.

In this paper, we present a novel, fast and accurate chirp-rate estimation algorithm based on the fractional Fourier transform (FrFT) and the Fibonacci search. The FrFT is a very-well known transform and has found itself many application areas, when the frequency of the signal of interest varies linearly in time. The FrFT is a natural domain for LFM signals, since the kernel of the FrFT itself is constituted of LFM signals. Throughout the FrFT domains, there exists a special domain, in which the energy of the LFM signals are most concentrated [11-13]. Using the energy preservation property of the FrFT, which states that the signal's amplitude increases when the energy concentrates, we propose a novel method for estimating the optimum transformation angle of an LFM signal. Since the optimum transformation angle is related to the chirp rate, the problem of estimating the chirp rate is then reduced to a single-dimensional search in the FrFT domains. In order to accelerate the search process, we propose to use the celebrated Fibonacci search [14], which requires far less computations. Simulation results show that the proposed method performs very well with less computational requirements.

The rest of the paper is organized as follows, Section II introduces the FrFT briefly and concludes with how the maximum magnitude method can be used for chirp rate estimation. Section III discloses the proposed method for estimating the chirp-rate and the Fibonacci search algorithm that accelerates the search process. Computer simulations are given in Section IV. The paper concludes in Section V.

II. PRELIMINARIES

In this section, we first give a preliminary definition of the FrFT and the section is concluded after the discussion relationship between the chirp rate of an LFM signal and the FrFT.

A. The Fractional Fourier Transform

The FrFT [15] is a linear and unitary transform. If $f(u)$ is a square integrable function, then the FrFT of this function is defined by

$$\mathcal{F}^\alpha\{f\}(u) = \sqrt{1 - j \cot(\alpha)} \int_{-\infty}^{\infty} f(\mu) \exp[j\pi(\cot(\alpha)\mu^2 - 2 \csc(\alpha)u\mu + \cot(\alpha)u^2)] d\mu, \quad (3)$$

where α is the transformation angle. The FrFT becomes the conventional FT for $\alpha = \pi/2$ and inverse FT for $\alpha = -\pi/2$. Therefore, FT is only a special case of the FrFT and for the other values of angles; the FrFT can be considered as an interpolation between the original signal, and the FT. For example, if $\alpha = 2\pi$ and $\alpha = \pi$, the transform appears to be the identity transform and the counter-identity transform, respectively. The FrFT is an energy-preserving transform as implied by the unitarity. Two consecutive FrFTs with angles α_1 and α_2 yield a single FrFT with the angle $\alpha_1 + \alpha_2$, where the FrFT transformation angle α is periodic with 2π .

One of the most interesting properties of the FrFT is that it rotates the transformed signal in the time-frequency domain, i.e., the Wigner distribution of the resultant signal is rotated with the transform angle α , in the clockwise direction. In other words, the FrFT rotates the time frequency axis in the counter-clockwise direction. This property is illustrated in Fig. 1.

From (3), it can be seen that the basis functions of the FrFT are the chirp functions. Therefore, the FrFT is the natural domain for LFM-type signals. In the optimum angle, the FrFT converts an LFM signal into a Dirac-delta distributed signal, where it is well-known [12-13] that the optimum angle α_{opt} is

$$\alpha_{opt} = \arctan(m) + \frac{\pi}{2} + k\pi, \quad (4)$$

where m is the actual chirp rate of the LFM signal of interest and k is any integer. Since the transform angle is a continuous function of the transform, it generally requires a search in the FrFT domain to find out the optimum transformation angle, which is generally computationally demanding.

B. Chirp Rate Estimation in the Fractional Fourier Domains

It is a very well-known fact that the FrFT can be used as a powerful tool for estimating the chirp rate of an LFM signal. The most widely used algorithm for estimating the chirp rate is the maximum magnitude method. This method searches for the angle that produces the maximum magnitude throughout all the angles between $[0, \pi]$ expressed by

$$\hat{\alpha}_{opt} = \underset{\alpha}{\operatorname{argmax}} P(\alpha), \quad (5)$$

where $P(\alpha)$ is the maximum of the magnitude square FrFT at the angle α , given by,

$$P(\alpha) = \max\{|\mathcal{F}^\alpha\{c\}(u)|^2\}. \quad (6)$$

The expected value of the resultant estimate $\hat{\alpha}$ is known to give the optimum transform angle, α_{opt} . Therefore, an estimate of the chirp rate can be found by

$$\hat{m} = \tan\left(\hat{\alpha}_{opt} - \frac{\pi}{2}\right). \quad (7)$$

As the maximum magnitude method searches through the angles, the LFM signal gets more and more compact when the search angle gets closer to the optimum angle. As a result of the preservation of the energy, the magnitude increases in order to make the total energy constant in the transform domain. The magnitude attains its maximum at the optimum transform domain, which converts the signal into an impulse, making the maximum magnitude method an optimum chirp-rate estimation method.

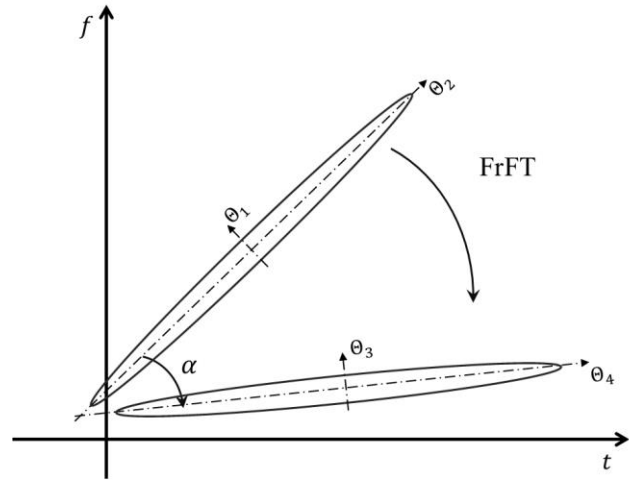


Fig. 1. Illustration of the rotation property of the FrFT in the time-frequency domain.

The only limiting factor of the usage of FrFT-based methods for estimating the chirp rate is its relatively high computational cost of digital computation of the FrFT. In the FrFT-domain, only a one-dimensional search is required to estimate the chirp-rate by using the maximum magnitude method. However, digital calculation of a single FrFT requires $\mathcal{O}(N \log N)$ complex multiplications and additions. Therefore, fast angle search algorithms are required. In the next section we propose a method that employs the FrFT to estimate the chirp-rate of an LFM signal based on.

III. PROPOSED METHOD

A. Minimum Inverse Magnitude

We propose that, instead of using the maximum magnitude method, minimum inverse magnitude method can also be used as a substitute. In the minimum inverse magnitude, an estimate of the optimum angle is found by,

$$\hat{\alpha}_{opt} = \min_{\alpha} J(\alpha), \quad (8)$$

where,

$$J(\alpha) = \frac{1}{P(\alpha)}, \quad (9)$$

which simply finds the minimum of the inverse of the maximum magnitude. However, calculating each point in the search space requires $\mathcal{O}(N \log N)$ complex multiplications and additions to calculate the FrFT. Therefore, instead of employing a brute-search algorithm, we propose to use the Fibonacci search.

B. Fibonacci Search

Fibonacci search is one of the well-known near-optimum search methods. In this method, a local search for the minimum of a cost function is evaluated cost-effective. The Fibonacci search algorithm finds a minimum of a cost function $f(x)$ in the interval of $[a, b]$.

In the Fibonacci algorithm, we select two points x_1 and x_2 in the range $[a, b]$ and evaluate the function at these two points

$f(x_1)$ and $f(x_2)$, where $x_1 < x_2$ and $(x_1 - a) = (b - x_2)$. Here, we assume that $f(a)$ and $f(b)$ are already known. If $f(x_1) < f(x_2)$, then we confine the new search interval to $[a, x_2]$. Otherwise, the new search interval is $[x_1, b]$. After updating the new interval, only a new point x_3 is selected inside the new interval and the other two points can be used. For example, if the new interval is $[a, x_2]$, the new point is selected such that $a < x_3 < x_2$. Then, $f(x_3)$ is evaluated. If $f(x_3) < f(x_1)$, then we confine the new interval as $[a, x_3]$. Otherwise, the new search interval is set to $[x_3, x_2]$. The beauty of the Fibonacci search method comes from the way of selecting internal points. The search points are selected such that only a single evaluation of the cost function is required at each iteration, except for the first iteration, which requires two evaluations. The algorithm stops when the search interval is smaller than a tolerance value ϵ . The proposed Fibonacci search algorithm for finding the minimum of inverse maximum magnitude is summarized in Algorithm 1, where $F_k = F_{k-1} + F_{k-2}$ is the k -th Fibonacci number of the order $k > 1$.

In our realizations, we choose $a = 0$ and $b = 2\pi$, so that the whole FrFT domain is our search domain. The number of required iterations is determined by the tolerance value ϵ . It is a well-known fact that a Fibonacci number can be approximated by $F_k \approx \frac{\sqrt{5}}{2} r^{k+1}$ for $k \geq 3$, where $r \approx 1.618$ is the golden ratio. Therefore, the required number of FrFTs can be found as,

Algorithm 1: The employed Fibonacci search method that finds an estimate of the chirp-rate, where the search is performed in the FrFT angles between 0 and 2π .

```

 $n \leftarrow \operatorname{argmin}_n \left\{ F_n \leq \frac{(b-a)}{\epsilon} \right\}$ 
 $\alpha_1 \leftarrow a + \frac{F_{n-2}}{F_n} (b-a)$ 
 $\alpha_2 \leftarrow a + \frac{F_{n-1}}{F_n} (b-a)$ 
while  $k < n - 1$ 
  if  $J(\alpha_1) > J(\alpha_2)$ 
     $a \leftarrow \alpha_1$ ;
     $\alpha_1 \leftarrow \alpha_2$ ;
     $\alpha_2 \leftarrow a + \frac{F_{n-k-1}}{F_{n-k}} (b-a)$ ;
  else
     $b \leftarrow \alpha_2$ ;
     $\alpha_2 \leftarrow \alpha_1$ ;
     $\alpha_1 \leftarrow a + \frac{F_{n-k-2}}{F_{n-k}} (b-a)$ ;
  end
   $k \leftarrow k + 1$ ;
end
 $\hat{\alpha}_{opt} \leftarrow \frac{\alpha_1 + \alpha_2}{2}$ ;
 $\hat{m} = \tan \left( \hat{\alpha}_{opt} - \frac{\pi}{2} \right)$ 

```

$$N_{FrFT} = \left\lceil \log_r \left(\frac{2}{\sqrt{5}} \frac{b-a}{\epsilon} \right) - 2 \right\rceil, \quad (10)$$

where $\lceil \cdot \rceil$ denotes the ceil operator. For a setting of $\epsilon = 10^{-5}$, $b = \pi$, and $a = 0$, the number of required FrFTs is only 26. As the computational complexity of digital computation of the FrFT is of $\mathcal{O}(N \log N)$ [16], our proposed algorithm is of $\mathcal{O}(N_{FrFT} N \log N)$ computational cost.

The next section discusses the estimation performance of the proposed chirp-rate estimator.

IV. SIMULATIONS AND RESULTS

In order to evaluate the performance of the proposed method, we generate a discrete-chirp signal,

$$c[n] = A \exp\{j\pi[m \times (nT_s)^2 + 2f_0(nT_s)]\} + w[n], \quad (11)$$

$n = 0, 1, \dots, N-1,$

where we take the sampling rate $T_s = 1/\sqrt{N}$, chirp rate $m = 0.2$, frequency shift $f_0 = 0.1$, and amplitude $A = 1$, and the number of the samples $N = 1024$. $w[n]$ is the additive white Gaussian noise with variance σ_w^2 .

In the noiseless case, the cost function $J(\alpha)$ for the LFM signal is plotted in Figure 2. It is clear that the cost function is an almost unimodal function attaining its minimum at the optimum angle $\alpha_{opt} = \arctan(m) + \pi/2$.

In the noisy case, estimation performance is compared to the CRLB in Figure 3. Performance criteria is taken as the MSE of the chirp-rate estimation, given by

$$MSE = \frac{1}{M} \sum_{k=1}^M (\hat{m} - m), \quad (12)$$

where \hat{m} is the estimated chirp rate and m is the actual chirp rate of the signal. M is the number of Monte-Carlo simulations, which we take as 10^4 .

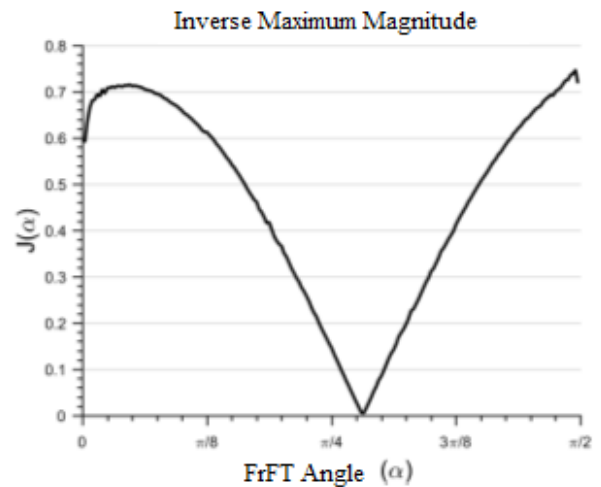


Figure 2. Inverse maximum magnitude cost function of a chirp signal.

Estimation performance of a the LFM chirp rate is plotted in Figure 3, which shows that MSE gets closer to the CRLB after a specific value of SNR. For the SNR values below the

threshold, estimation performance is highly degraded, which is also known as the maximum likelihood threshold. For this simulation we choose the Fibonacci parameter as $\epsilon = \frac{10^{-5}}{\pi}$. For this value of ϵ , only 26 iterations are required to estimate the chirp-rate. Therefore, the computational cost of our proposed estimator is only in the order of $\mathcal{O}(26N \log N)$.

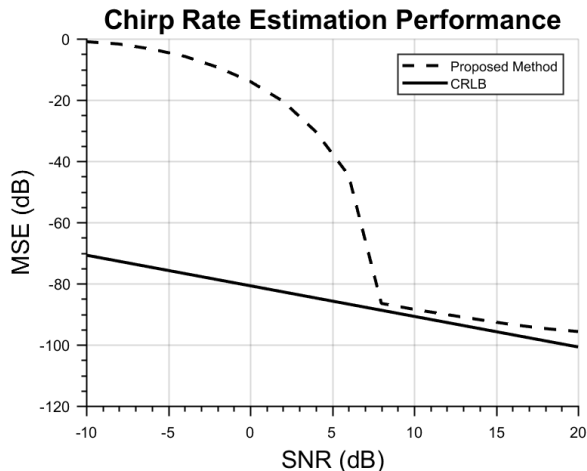


Figure 3. Estimation performance of the chirp rate \hat{m} .

Figure 3 also shows that, for SNR values greater than 7dB, MSE of the estimation are very low. For most of the applications, this kind of estimation accuracy is highly satisfactory.

V. CONCLUSIONS

In this work, we have presented a fast and accurate way to estimate the chirp-rate of an LFM signal. The problem of estimating the chirp-rate is reduced to finding the minimum of a cost function, $J(\alpha)$. Taking the advantage of the relationship between the index that minimizes $J(\alpha)$ and the chirp rate, chirp-rate of the LFM signal is estimated. Instead of a brute-search, we propose to use the celebrated Fibonacci search in order to accelerate the search process. Simulation results show that the proposed method produces highly accurate estimation results.

REFERENCES

- [1] A.G. Stove, "Linear FMCW radar techniques," Proc. Inst. Elect. Eng., pt. F, pp. 343–350, Oct. 1992.
- [2] P.R. Atkins, T. Collins, K.G. Foote, "Transmit–signal design and processing strategies for sonar target phase measurement," IEEE J. Sel. Topics Signal Process., vol. 1, no. 1, Jun. 2007.
- [3] S. Patole, M. Torlak, D. Wang, and M. Ali, "Automotive radars: A review of signal processing techniques," IEEE Signal Proc. Mag., col. 34, no. 2, 2017.
- [4] J. Muoz–Ferraras, F. Perez–Martinez, M. Burgos–Garcia, "Helicopter classification with a high resolution LFM radar," IEEE Trans. Aerosp. Electron. Syst., vol. 45, no. 4, pp. 1373–1384, Jan. 2010.
- [5] T. Misaridis, J. A. Jensen, "Use of modulated excitation signals in medical ultrasound. Part I: basic concepts and expected benefits," IEEE Trans. Ultrason., Ferroelect., Freq. Control, vol. 52, no. 2, pp. 177–191, Feb. 2005.
- [6] M. Martone, "A multicarrier system based on the fractional Fourier transform for time–frequency–selective channels," IEEE Trans. Commun., vol. 49, no. 6, pp. 1011–1020, Jun. 2001.

- [7] P.M. Djuric and S. M. Kay, "Parameter estimation of chirp signals," IEEE Trans. Acoust., Speech, Signal Process., vol. 38, no. 12, pp. 2118–2126, Dec. 1990.
- [8] B. Boashash, "Estimating and interpreting the instantaneous frequency of a signal," Proc. IEEE, vol. 80, no. 4, pp. 519–569, Apr. 1992.
- [9] G.F. Boudreaux-Bartels and T.W. Parks, "Time-varying filtering and signal estimation techniques using Wigner distribution synthesis techniques," IEEE Trans. Acoust., Speech, Signal Process., vol. 34, no. 3, pp. 442–451, Jun. 1986.
- [10] S. Kay and G. F. Boudreaux-Bartels, "On the optimality of the Wigner distribution for detecting a chirp signal," in Proc. IEEE ICASSP, Mar. 1985.
- [11] L. Zheng and D. Shi, "Maximum amplitude method for estimating the compact fractional Fourier domain," IEEE Signal Proc. Lett., vol. 17, no. 3, Mar. 2010.
- [12] C. Capus and K. Brown, "Fractional Fourier transform of the Gaussian and fractional domain signal support," IEE Proc. Vis. Image. Signal Process., vol. 150, no. 2, pp. 99–106, Apr. 2003.
- [13] C. Capus, Y. Rzhannov, and L. Linett, "The analysis of multiple linear chirp signals," Proc. IEE Symposium on Time-Scale and Time-Frequency Analysis and Applications, pp. 4/1–4/7, London, Feb. 2000.
- [14] D.E. Ferguson, "Fibonacci searching," Commun. ACM, vol. 3, no. 12, Dec. 1960.
- [15] L.B. Almeida, "The fractional Fourier transform and time frequency representations," IEEE Trans. Signal Process., vol. 42, no. 11, pp. 3084–3091, Nov. 1994.
- [16] C. Candan, M.A. Kutay, and H.M. Ozaktas, "The discrete fractional Fourier transform," IEEE Trans. Signal Process., vol. 48, no. 5, pp. 1329–1337, May 2000.

BIOGRAPHY



AHMET SERBES received the B.S. degree from Istanbul Technical University, Istanbul, Turkey in 2002, the M.S. and Ph.D. degrees from Yildiz Technical university in 2004 and 2011, respectively all in electronics and communications engineering.

He is currently with the department of Electronics and Communications Eng. Dept., Yildiz Technical University, where he is an Assistant Professor. His research interests include statistical signal processing, estimation and detection theory, communications, linear transformations, time–frequency signal processing, and fractional Fourier transform.

Evaluation of the Turkish Highway Network Analysis with Traffic Data

İ. Türker

Abstract— As a complex geospatial structure, Turkish national highway transportation network is studied by the means of network science. We used the dataset retrieved from the KGM (Karayolları Genel Müdürlüğü) maps with a hand-driven process. The dataset labels the junctions in the map as nodes, and the roads between these junctions as edges. We outlined the statistical properties of the Turkish highway transportation network by the means of eigenvector, betweenness, closeness centrality, modularity and eccentricity measures, while comparative percentile plots between these measures are also performed. We investigated the correlation of these parameters with the traffic volume, and outlined that only eccentricity measure is correlated with the traffic volume. We also investigated the degree correlations of the network and found that the network displays disassortative mixing behavior, meaning that nodes with high degrees tend to connect with lower degree nodes, and vice versa. This property is consistent with the recent studies of transportation networks, as well as various types of real networks like Internet, World-Wide Web, protein interactions, neural network etc.

Index Terms— Transportation networks, Complex networks, Centrality, Data analysis, Scale-free networks.

I. INTRODUCTION

NETWORK science provides a framework to analyze the infrastructures of the networked systems in nature. These systems are in a variety spanning cellular [1, 2], ecological [3, 4], social [5-8], WWW [9], power-grid networks [10, 11] etc. which exist as interconnected systems in nature. The characterization of such complex systems using statistical and computational techniques have attracted considerable attention in the literature in recent years. Complex systems are composed of numerous components, those interact in a manner that collective behavior is not an ordinal function of their individual behaviors [12].

As a complex system, transportation networks also deal with the nature of the movement patterns of people in a geographic region, where the movement is towards roads, railways or airways [13]. The studies in this field are performed in regional, national or global scale.

İ. TÜRKER, Department of Computer Engineering; Karabük University, Karabük, Turkey, (e-mail: iturker@karabuk.edu.tr) 

Manuscript received August 26, 2017; accepted December 28, 2017.
DOI: [10.17694/bajece.369235](https://doi.org/10.17694/bajece.369235)

Guimera et al. analyzed the structure of the worldwide air transportation network, a large-scale structure with a considerable impact on local, national, and international economies. They outlined that the most connected cities of the network are not necessarily the most central, resulting in anomalous values of the centrality [14]. In another study concerning air transportation networks, Bagler evaluated domestic civil aviation infrastructure of India as a complex network. He labeled the structure as a small-world network with scale-free property, as fingerprints of self-organizing phenomenon also reported in other transportation network studies. The mentioned network also displays disassortative mixing property, meaning that high degree nodes tend to connect with low degree nodes in majority [15].

Xu and Harriss stated out that the air transportation network of U.S. is also a small-world and scale-free network. They also outlined the emergence of a rich-club phenomenon which means cities with numerous connections tend to connect to cities with comparable degrees, which in turn sustains high volumes of traffic between these high degree nodes [16]. Also disassortative mixing patterns are observed by Xu and Harris, as reported in the study of Bagler.

Road and railway networks are other forms of transportation networks in which connections between nodes are affected by their spatial structures. In such networks connections between distant nodes can only be sustained via other nodes locating spatially between these distant nodes. This in turn results connections only established between spatially close locations. The studies in this aspect span several public transportation networks of regions like Singapore [17], Shanghai [18], Greece [19], Boston (U.S.) [20] etc. In the study of Soh et al., while two networks studied yield nearly neutral assortativity behaviors, bus network of Singapore is slightly disassortative while the fast railway network is slightly assortative [17].

Several network studies in transportation networks are also performed to investigate the impact of network structure in tourism [21], robustness in highway networks [22], capacity reliability road networks [23], urban street structures [24, 25] etc. The commonality of the mentioned studies are the evidence of universal properties of complex networks like being small-world and scale-free, together with clustering coupled with a disassortative mixing property.

This study mainly focuses on uncovering the centrality and assortativity properties of the Turkish highway transportation network. The specifications of the dataset together with the results are detailed in the coming section, followed by a conclusion section.

II. DATA AND METHODS

We can briefly abstract the basic network properties from that study as follows. The Turkish highway transportation network displays invincibly high node separation (~28.3) together with high diameter (83) values compared to the most real network structures. These high values are correlated with the spatial structure of the constructed network, in which the nodes are assumed as the junction points of the roads and the edges are the roads connecting these nodes. The network is also reported as having very high modularity (0.918) together with low average clustering coefficient (0.034). Further conclusions about the basic network analysis can be accessed via the mentioned study.

The network approach has a long tradition in economic geography and city planning, being used to investigate the territorial relationships among communication flows, population, wealth and land-uses [28]. Centrality is also a fundamental concept in network analysis, described as below:

- i) Closeness centrality, C^C , measures how a node i is close to the all other nodes along the shortest paths. It is defined as:

$$C_i^C = \frac{N-1}{\sum_{j \in G, j \neq i} d_{ij}} \quad (1)$$

where N is the number of nodes and d_{ij} is the shortest path length between nodes i and j in a network [28, 29].

- ii) Betweenness Centrality, C^B assumes a node is central if it is located between many other nodes, regarding the number of occurrences for that node as a hop between the shortest paths connecting the other nodes. The betweenness centrality of node i is defined as:

$$C_i^B = \frac{1}{(N-1)(N-2)} \sum_{j,k \in G, j \neq k \neq i} n_{jk}(i) / n_{jk} \quad (2)$$

where n_{jk} is the number of shortest paths between nodes j and k , and $n_{jk}(i)$ is the number of shortest paths between nodes j and k which contain node i [28, 29].

- iii) Eigenvector Centrality, C^E defines the importance of a node as its connectivity to important nodes. It can also be assumed as a weighted sum of not only direct connections but indirect connections of every length. Thus, it takes into account the entire connectivity pattern in the network. Let A be the adjacency matrix for this graph; $a_{ij} = 1$ if vertices i and j are connected by an edge and 0 if not.

$$Ax = \lambda x, \quad \lambda x_i = \sum_{j=1}^n a_{ij} x_j, \quad i = 1, \dots, n \quad (3)$$

Eq. (3) describes eigenvector centrality x in two equivalent ways, as a matrix equation and as a sum. The centrality of a vertex is proportional to the sum of the centralities of the vertices to which it is connected. λ is the

largest eigenvalue of A and n is the number of vertices. [30].

Eccentricity (E), a measure involving the distances between nodes is the maximum distance of a node to all other nodes in a network. Thus the minimum eccentricity of a network defines its radius whereas the maximum eccentricity defines its diameter [31]. The exact definition and formulation can be accessed via this Ref. This measure deviates from the average path length for a node by always taking into consideration the maximal shortest distances to the other nodes.

Another measure investigated in the network is Modularity (M), quantifying the idea that true community structure in a network corresponds to a statistically surprising arrangement of edges. Modularity is the number of edges falling within groups minus the expected number in an equivalent network with edges placed at random. The precise mathematic formulation can be accessed at Ref. [32].

III. RESULTS

3.1 Centrality, Modularity and Eccentricity

To shed insight into the infrastructure of the network by the means of centrality, we calculated the centrality measures for the nodes by using the Gephi software introduced by Bastian [33]. The results are further analyzed in MATLAB to assign the number of nodes belonging to some pairs of Betweenness Centrality, Closeness Centrality, Eigenvector Centrality and Modularity Class measures, as percentiles of their maximal values. We present 3D percentile plots pairing these measures in Figures 1 to 3.

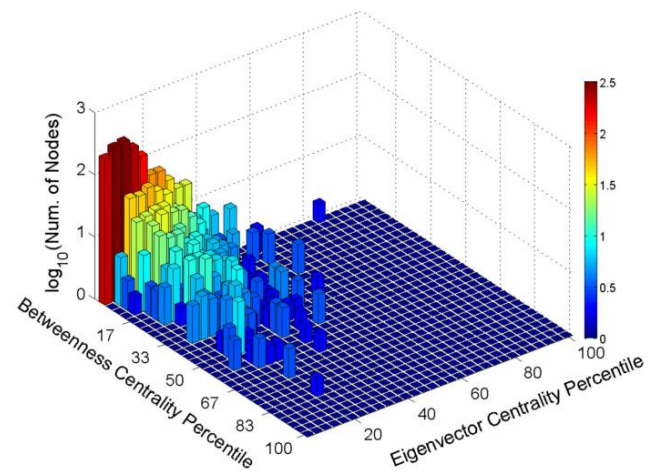


Fig. 1. The number of nodes (logarithmically scaled) corresponding to the intersection of Betweenness Centrality vs. Eigenvector Centrality values. The centrality values are expressed as percentiles to their maximal values.

Fig.1 demonstrates the logarithmically scaled number of nodes corresponding to the C^B and C^E pairs. The nodes seem to have C^E values below 50% while the C^B scale is widely used. This scene outlines that there exists a very small number of nodes having high C^E values, while the C^B values display a more homogenous decaying characteristic. The trend also shows that highest pairing probability emerges as very small C^B

values (<5%) with a range of C^E values between 0 to 30%. The highest C^B values seem to pair with C^E values around 20%. Also the highest C^E values pair with C^B values below 5%.

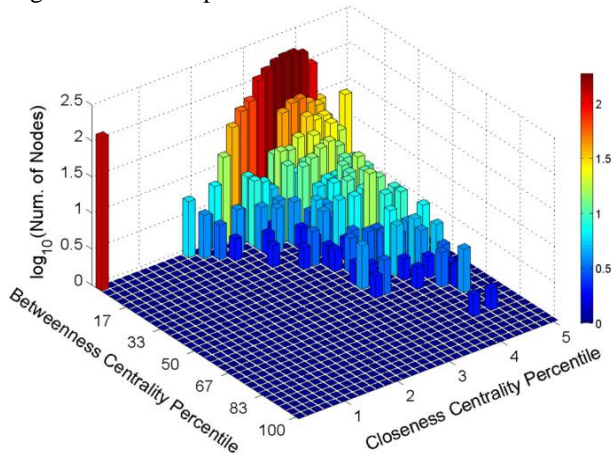


Fig. 2. The number of nodes (logarithmically scaled) corresponding to the intersection of Betweenness Centrality vs. Closeness Centrality values. The centrality values are expressed as percentiles to their maximal values.

Fig.2 shows the logarithmically scaled number of nodes corresponding to the C^B and C^C pairs. Since the upper 95% scale of the C^C values include very sparse node circumstances, we focused on the first 5% of the C^C values in the graph. Therefore, we can conclude that most of the nodes in the network have small C^C values, affected from the spatial dependencies of the network. On the other hand, the nodes display higher C^B values compared to C^C , indicating that the nodes in some way locate in the shortest paths between cities, whether they are not close to the rest of the network. The single distribution of C^C cumulates between 2-5% of the axis, having peak values at ~4%. This is an indicator of the spatial complexity of the network, which leads numerous hops to connect locations in the map, resulting high separation values mentioned in the beginning of the section. As mentioned in Fig.1, C^B scale is widely used. The pairing probability between C^B and C^C values make peak around 4% of C^C and <5% of C^B values, decaying towards lower closeness and higher betweenness centrality values.

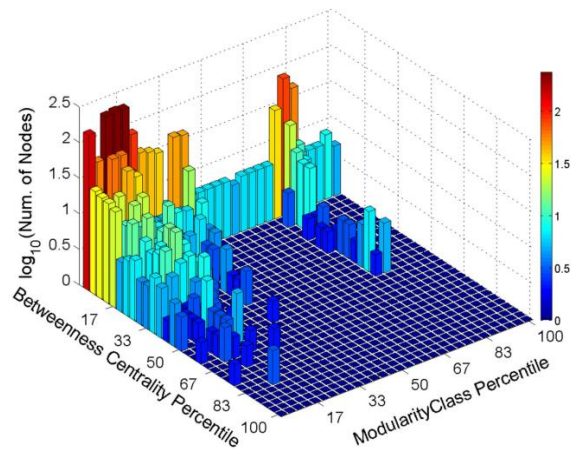


Fig. 3. The number of nodes (logarithmically scaled) corresponding to the intersection of Betweenness Centrality vs. Modularity Class values. The centrality and modularity values are expressed as percentiles to their maximal values.

Fig.3 demonstrates the pairing characteristics between C^B and M . We can infer from the figure that both measures display more homogenous distributions compared to the first two plots. The higher C^B values emerge for either M values less than 43%, or M values close to 80%. This behavior seems to be mostly driven by the bimodal distribution of Modularity. The most probable pairing occasion is for the lower band C^B and M values, while there exist nodes also having low C^B together with high modularity values.

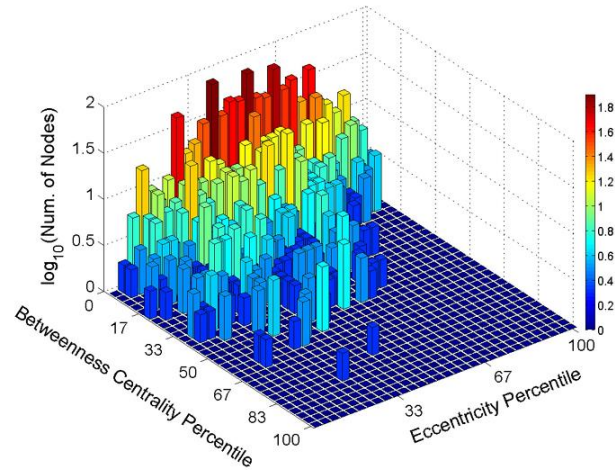


Fig. 4. The number of nodes (logarithmically scaled) corresponding to the intersection of Betweenness Centrality vs. Eccentricity values. The centrality and eccentricity values are expressed as percentiles to their maximal values.

Fig.4 yields the pairing characteristics between C^B and E . We can infer from the figure that the nodes seem to have E values distributed smoothly through the percentile range while the C^B distribution decays with increasing values. The highest pairing probability emerges for small C^B values (<17%) with the mid-range of E values. This property indicates that nodes with high eccentricity values tend to have small betweenness centrality values in the transportation network.

3.2 Traffic Volume

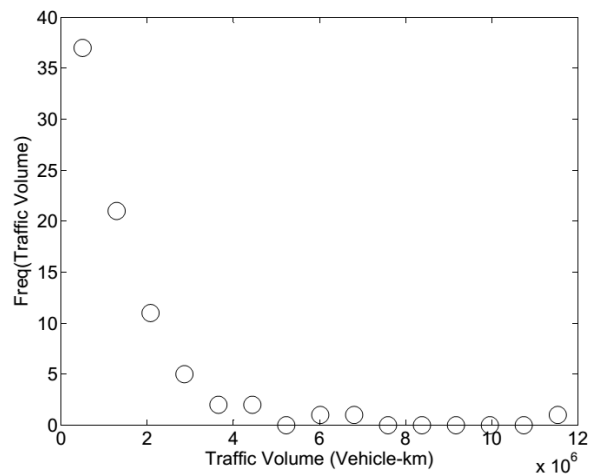


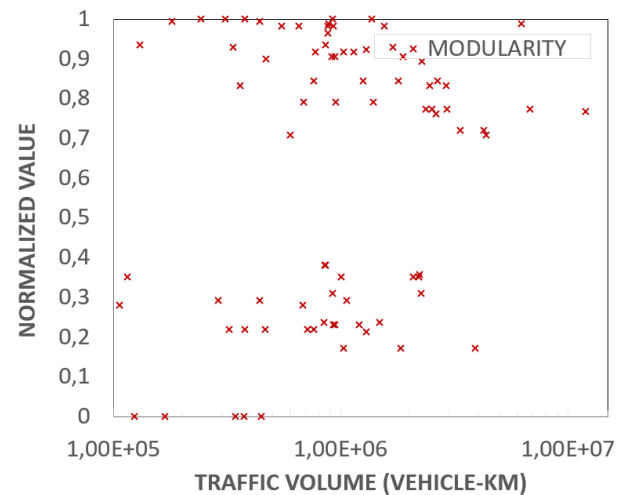
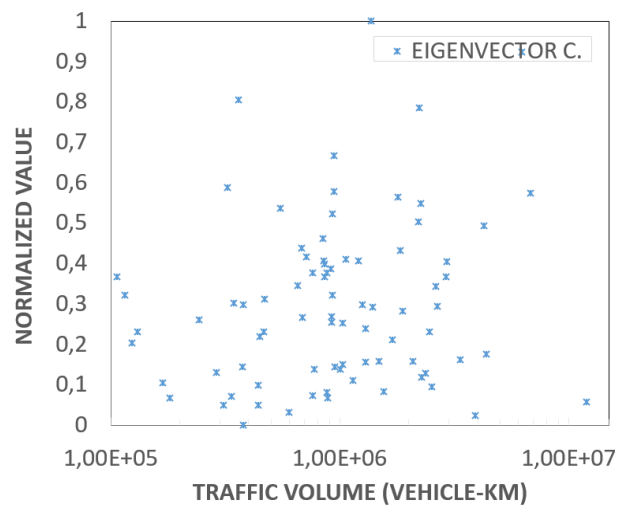
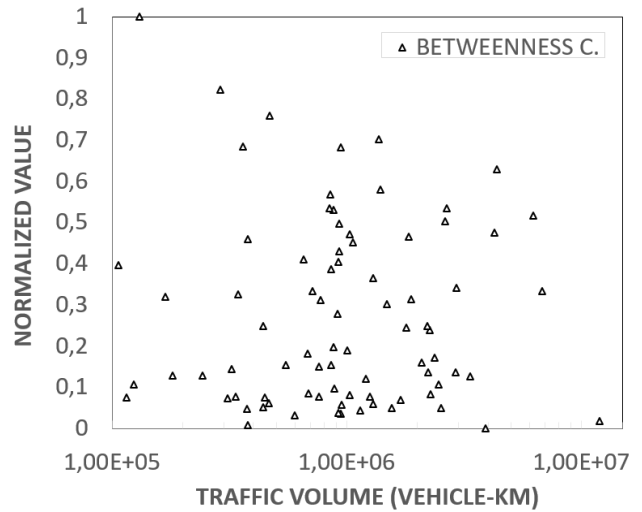
Fig. 5. Histogram for traffic volume in vehicle-km, retrieved from KGM statistics. The volumes are products of vehicle counts with distances covered in kilometers.

We retrieved the traffic volume data for the cities from the statistics section of KGM [34]. This data set includes traffic volume data with a vehicle-km basis, including the product of the vehicles with the distance covered. We first present the histogram of traffic volume in Fig. 5. This figure indicates a small portion of cities have very high traffic volumes, whereas the probability increases towards small volumes.

To investigate the correlation of traffic volume with network parameters, we present the scattered distribution of five network parameters through the traffic volume in Fig. 6. The data used in these graphs include the traffic volume measures for all 81 cities in Turkey, coupled with the nodes that correspond to the city centers in the network representations. Therefore, it represents only 81 nodes of the network for which a traffic volume data can be retrieved from KGM statistics. The relation between the centrality measures and modularity versus traffic volume do not indicate direct correlations as the graphics display. Only the eccentricity measure implies a correlated trend through the traffic volume range. To quantify the correlations between these five measures and traffic volume, we present the correlation coefficients calculated from the same data as in Table 1.

TABLE I
CORRELATION COEFFICIENTS CALCULATED FOR THE FIVE
PARAMETERS VERSUS TRAFFIC VOLUME FOR THE 81 CITY
CENTERS

	CORR. COEFF.
CLOSENESS C.	-0,076
BETWEENNESS C.	-0,036
EIGENVECTOR C.	0,102
MODULARITY	0,153
ECCENTRICITY	0,322



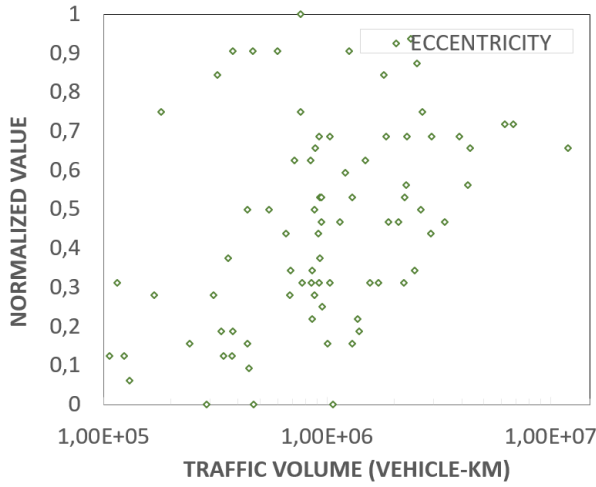


Fig. 6. Scattered distribution of 3 centrality parameters, modularity, and eccentricity through traffic volume in vehicle-km. The parameters in the vertical axis are normalized according to their min-max values. The first panel includes all parameters in one plot, while the other panels display the standalone plots of these parameters vs. traffic volume.

The correlation coefficients presented in Table 1 indicate that the only noteworthy parameter by the means of correlation with the traffic volume is the eccentricity. The main cause for this output may be that higher eccentricity, meaning higher greatest path length with the rest of the cities, results more number of cities which may use the path through that city. In fact, betweenness centrality measure should be expected to imply more correlation with traffic volume, but in this case (a spatially distributed transportation network) shortest paths do not emerge to determine transportation routes. Instead, drivers seem to prefer routes with shortest metric distances or shortest trip durations.

3.3. Degree Correlations and Assortativity

Generally, a network is denoted to have degree correlations if the number of links between the nodes with high and low-degrees is invincibly different from a randomly generated network. In an *assortative network*, hubs favor connecting to each other and avoid connecting nodes with small degrees. Additionally, small-degree nodes favor connecting to other small-degree nodes. Networks displaying such trends are *assortative*. Contrary with this definition, in a *disassortative network*, hubs don't connect to hubs, preferring wiring with small-degree nodes. And the nodes with small degrees tend to connect to hubs, avoiding links to nodes with comparable degrees. If both trends are not observed in a network, i.e. the degree of a node does not affect its neighborhood preferences, such a network is called *neutral* [35].

To measure this behavior in a network, degree correlation function is derived from the edge matrix of the network. We first measure the average degree of the neighbors of each node as in Eq. 4.

$$k_{nn}(k_i) = \frac{1}{k_i} \sum_{j=1}^N A_{ij} k_j \quad (4)$$

Then, the *degree correlation function* is used to calculate the average degree of neighbors for all nodes with degree k as in Eq. 5.

$$k_{nn}(k) = \sum_{k'} k' P(k'|k) \quad (5)$$

Where $P(k'|k)$ stands for the conditional probability that a node of *degree-k* will have a neighbor of *degree-k'*. As a result, $k_{nn}(k)$ denotes the average degree of the neighbors of all nodes with degree k [35]. The k_{nn} vs k plot displays an increasing trend in assortative networks, a decreasing trend in disassortative networks, and a constant trend in neutral networks.

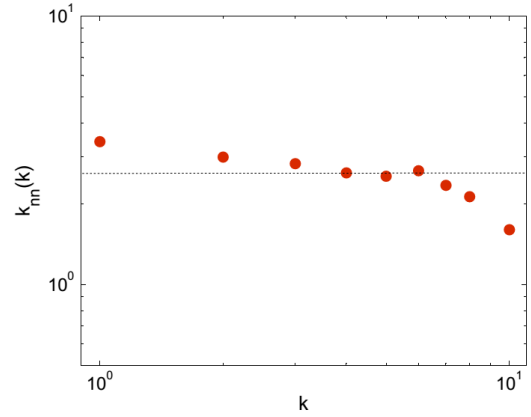


Fig. 7. Degree correlations for the Turkish highway transportation network. The dotted line corresponds to average degree. The decreasing trend of the $k_{nn}(k)$ function indicates that the network is *disassortative*.

Deriving the $k_{nn}(k)$ plot for our network, we present the degree correlation function in Fig. 7. The decreasing trend is obvious, indicating that the network is *disassortative*. This behavior is evident in most transportation networks as mentioned in the introduction section.

Another indicator of degree correlations is the *degree correlation coefficient*, proposed by Newman and calculated with the equation below :

$$r = \frac{1}{\sigma_q^2} \sum_{jk} jk (e_{jk} - q_j q_k) \quad (6)$$

where

$$\sigma_q^2 = \sum_k k^2 q_k - [\sum_k k q_k]^2 \quad (7)$$

For the detailed extraction of Eq. 6, the reader is referred to the study of Newman in Ref. [36].

Correlation function is zero in the absence of assortative mixing, while it is positive for assortative or negative for disassortative mixing properties. The real and modeled network examples reported by Newman are also presented in Table 2 [36].

Calculating the assortativity coefficient r for our network, we found $r = -0.1708$, confirming the above inference of disassortativity. We can therefore conclude that the spatially generated urban transportation network studies in this paper yields disassortative mixing property.

TABLE II
SIZE n AND ASSORTATIVITY COEFFICIENT r FOR A NUMBER OF
DIFFERENT NETWORKS, REPORTED BY NEWMAN [36].

	network	n	r
real-world networks	physics coauthorship ^a	52 909	0.363
	biology coauthorship ^a	1 520 251	0.127
	mathematics coauthorship ^b	253 339	0.120
	film actor collaborations ^c	449 913	0.208
	company directors ^d	7 673	0.276
	Internet ^e	10 697	-0.189
	World-Wide Web ^f	269 504	-0.065
	protein interactions ^g	2 115	-0.156
	neural network ^h	307	-0.163
food web ⁱ	92	-0.276	
models	random graph ^u		0
	Callaway <i>et al.</i> ^v		$\delta/(1+2\delta)$
	Barabási and Albert ^w		0

Depending on Table 2, in which the assortativity coefficients for various networks are reported by Newman, we can figure out that together with the transportation networks mentioned in the introduction section, the disassortative mixing behavior is coherent with some real networks like Internet, World-Wide Web, protein interaction networks, neural networks, food web etc. These types of networks are rather physically connected networks, while the social networks listed as the first group of Table 2 display assortative mixing property.

IV. CONCLUSIONS AND FUTURE WORK

Studying the centrality, modularity and assortativity properties of the Turkish highway transportation network, composed of physical connections (roads) between the junctions of roads as edges, we presented 3D comparative plots of the centrality and modularity measures first. We outlined that the betweenness centrality scale used in all the three 3D percentile plots has a homogenous distribution, meaning that the network includes nodes of various C^B values with a decreasing trend. Nodes have eigenvector centrality measures stuck in the lower 50% band of the C^E scale, while the highest C^B values seem to pair with C^E values around 20%. The nodes with highest C^E values tend to have C^B values below 5%.

Focusing on the closeness centrality measure, we see that almost all the nodes are of 5% closeness to the rest of the network. This is an expected result originating from the spatial dependencies of the network. Having relatively small closeness values, the nodes display higher betweenness centrality values, indicating that the nodes in some way locate in the shortest paths between cities whether they are not close to the rest of the network. The single distribution of C^C ranging between 2-5% of the axis indicates that the network has a spatially complex structure, resulting high separation between nodes. C^B and C^C values mostly pair around 4% of C^C and <5% of C^B scales, decaying towards lower closeness and higher betweenness centrality values.

The modularity measure, conveying information about the tendency of nodes to form modules, is recently reported to have very high values for this network [26], therefore labels the network as highly modular. The single distribution of Modularity displays bimodal character while it pairs with

higher betweenness centrality values around 43% and 80% of the scale. The pairing probability peaks for lower betweenness and modularity.

The eccentricity measure, quantifying the maximal shortest distance of a node to the rest of the nodes is nearly uniformly distributed over betweenness centrality, whereas it is the most correlated measure with the traffic volume of the cities. We conclude that the uncorrelated behavior of traffic volume with the centrality measures is mostly driven by the selection of trip routes by drivers regarding with the main roads/highways that make the travel shorter in metric distance or time. These routes generally may not be the shortest paths of the graph.

The concept of assortativity in a network probes the emergence of degree correlations of the paired nodes. The quantitative way of testing this phenomenon is the assortativity coefficient r proposed by Newman, which we found $r=-0.1708$ for our network. Together with the $k_{nn}(k)$ function which yields negative slope for our network, both indicators label our network as disassortative, coherent with the real networks with "more physical" wiring mechanisms.

As a future work, this study can be extended to include sub-urban roads which are not covered in this study. Also, more detailed transportation networks can be constructed via image processing techniques applied over satellite images.

ACKNOWLEDGMENT

The author thanks Sabah Bashir Salem Rashed for sharing raw data supplied from KGM maps.

REFERENCES

- [1] H. Jeong, S. P. Mason, A.-L. Barabási, and Z. N. Oltvai, "Lethality and centrality in protein networks," arXiv preprint cond-mat/0105306, 2001.
- [2] D. A. Fell and A. Wagner, "The small world of metabolism," *Nature biotechnology*, vol. 18, p. 1121, 2000.
- [3] I. Hartmann-Sonntag, A. Scharnhorst, and W. Ebeling, "Modelling selforganization and innovation processes in networks," arXiv preprint cond-mat/0406425, 2004.
- [4] J. M. Montoya, S. L. Pimm, and R. V. Solé, "Ecological networks and their fragility," *Nature*, vol. 442, p. 259, 2006.
- [5] M. E. J. Newman, "The structure of scientific collaboration networks," *Proceedings of the National Academy of Sciences of the United States of America*, vol. 98, pp. 404-409, Jan 2001.
- [6] A. Cavusoglu and I. Turker, "Scientific collaboration network of Turkey," *Chaos Solitons & Fractals*, vol. 57, pp. 9-18, Dec 2013.
- [7] A. Ferligoj, L. Kronegger, F. Mali, T. A. B. Snijders, and P. Doreian, "Scientific collaboration dynamics in a national scientific system," *Scientometrics*, vol. 104, pp. 985-1012, Sep 2015.
- [8] A. M. Manago, T. Taylor, and P. M. Greenfield, "Me and my 400 friends: the anatomy of college students' Facebook networks, their communication patterns, and well-being," *Developmental psychology*, vol. 48, p. 369, 2012.
- [9] A. L. Barabási, R. Albert, and H. Jeong, "Scale-free characteristics of random networks: the topology of the World-Wide Web," *Physica A*, vol. 281, pp. 69-77, Jun 2000.
- [10] A. E. Motter, S. A. Myers, M. Anghel, and T. Nishikawa, "Spontaneous synchrony in power-grid networks," arXiv preprint arXiv:1302.1914, 2013.
- [11] G. A. Pagani and M. Aiello, "The power grid as a complex network: a survey," *Physica A: Statistical Mechanics and its Applications*, vol. 392, pp. 2688-2700, 2013.
- [12] M. E. Newman, "The structure and function of networks," *Computer Physics Communications*, vol. 147, pp. 40-45, 2002.
- [13] M. G. Bell and Y. Iida, "Transportation network analysis," 1997.
- [14] R. Guimera, S. Mossa, A. Turttschi, and L. N. Amaral, "The worldwide air transportation network: Anomalous centrality, community structure, and

cities' global roles," Proceedings of the National Academy of Sciences, vol. 102, pp. 7794-7799, 2005.

- [15] G. Bagler, "Analysis of the airport network of India as a complex weighted network," *Physica A: Statistical Mechanics and its Applications*, vol. 387, pp. 2972-2980, 2008.
- [16] Z. Xu and R. Harriss, "Exploring the structure of the US intercity passenger air transportation network: a weighted complex network approach," *GeoJournal*, vol. 73, p. 87, 2008.
- [17] H. Soh, S. Lim, T. Y. Zhang, X. J. Fu, G. K. K. Lee, T. G. G. Hung, et al., "Weighted complex network analysis of travel routes on the Singapore public transportation system," *Physica a-Statistical Mechanics and Its Applications*, vol. 389, pp. 5852-5863, Dec 2010.
- [18] Y. Li, W. Zhou, and S.-j. Guo, "An Analysis of Complexity of Public Transportation Network in Shanghai [J]," *Systems Engineering*, vol. 1, p. 006, 2007.
- [19] D. Tsiotas and S. Polyzos, "Introducing a new centrality measure from the transportation network analysis in Greece," *Annals of Operations Research*, vol. 227, pp. 93-117, 2015.
- [20] V. Latora and M. Marchiori, "Is the Boston subway a small-world network?," *Physica A: Statistical Mechanics and its Applications*, vol. 314, pp. 109-113, 2002.
- [21] H.-Y. Shih, "Network characteristics of drive tourism destinations: An application of network analysis in tourism," *Tourism Management*, vol. 27, pp. 1029-1039, 2006.
- [22] D. M. Scott, D. C. Novak, L. Aultman-Hall, and F. Guo, "Network robustness index: A new method for identifying critical links and evaluating the performance of transportation networks," *Journal of Transport Geography*, vol. 14, pp. 215-227, 2006.
- [23] A. Chen, H. Yang, H. K. Lo, and W. H. Tang, "Capacity reliability of a road network: an assessment methodology and numerical results," *Transportation Research Part B: Methodological*, vol. 36, pp. 225-252, 2002.
- [24] S. Porta, P. Crucitti, and V. Latora, "The network analysis of urban streets: a primal approach," *Environment and Planning B: planning and design*, vol. 33, pp. 705-725, 2006.
- [25] S. Porta, P. Crucitti, and V. Latora, "The network analysis of urban streets: a dual approach," *Physica A: Statistical Mechanics and its Applications*, vol. 369, pp. 853-866, 2006.
- [26] İ. Türker, S. O. Tan, and S. B. S. Rashed, "Extracting the connectivity properties of the Turkish highway transportation network," presented at the ICRES, Kuşadası, Aydın, 2017.
- [27] (2017). Karayolları Genel Müdürlüğü Bilgi İşlem Dairesi, "Haritalar". Available: <http://www.kgm.gov.tr/Sayfalar/KGM/SiteTr/Root/Haritalar.aspx>
- [28] P. Crucitti, V. Latora, and S. Porta, "Centrality measures in spatial networks of urban streets," *Physical Review E*, vol. 73, p. 036125, 2006.
- [29] S. Wasserman and K. Faust, *Social network analysis: Methods and applications* vol. 8: Cambridge university press, 1994.
- [30] P. Bonacich, "Some unique properties of eigenvector centrality," *Social networks*, vol. 29, pp. 555-564, 2007.
- [31] P. Dankelmann, W. Goddard, and C. S. Swart, "The average eccentricity of a graph and its subgraphs," *Utilitas Mathematica*, vol. 65, pp. 41-52, 2004.
- [32] M. E. J. Newman, "Modularity and community structure in networks," *Proceedings of the National Academy of Sciences*, vol. 103, pp. 8577-8582, 2006.
- [33] M. Bastian, S. Heymann, and M. Jacomy, "Gephi: an open source software for exploring and manipulating networks," presented at the International AAAI Conference on Weblogs and Social Media, San Jose, California, 2009.
- [34] "Karayolları Genel Müdürlüğü Bilgi İşlem Dairesi, "Trafik ve Ulaşım Bilgileri"," 2017.
- [35] A. L. Barabási, *Network Science*. Cambridge: Cambridge University Press, 2016.
- [36] M. E. Newman, "Assortative mixing in networks," *Physical review letters*, vol. 89, p. 208701, 2002.

BIOGRAPHIES



İlker TÜRKER was born in Karabük, Turkey, in 1980. He received his B.S. Degree from Istanbul Technical University, Dept. of Electronics and Telecommunications, in 2001, M.S. degree from Zonguldak Karaelmas University, Dept. of Electrics and Electronics, in 2006 and Ph.D. degree in computer software, from Karabük University, Dept. of Computer Engineering, in 2013. He has been an Assistant Professor with the Computer Engineering department, Karabük University. He studies on data mining, complex network analysis and modeling, neurocomputing. He is also Assistant Editor-in-Chief in JESTECH, an international ESCI-indexed journal about engineering, science and technology, which is published by Elsevier BV.

FPGA Schematic Implementations and Comparison of FIR Digital Filter Structures

O. Coşkun, and K. Avci

Abstract—In this study, we investigate the FPGA schematic implementations of finite impulse response (FIR) digital filters for three fundamental structures on Altera DE2-115 board without requiring any other software packages such as DSP Builder and Matlab Simulink. First of all, a low pass FIR digital filter is designed by using Matlab filter design and analysis tool (fdatool) program. Then, the designed filter is implemented and simulated on Matlab for a given input signal. After that, for three fundamental structures (namely direct-form, transposed direct-form, and symmetric direct-form) in literature, the designed filter is implemented schematically on Quartus-II software and then each project containing different structure implementation is compiled. Then, the digital filters implemented by each structure are simulated by University Program Vector Wave File (VWF) simulation program on Quartus-II software. Simulation results show that the obtained results are the same as the ones obtained on Matlab, which confirms that the schematic designs are successfully implemented. Moreover, the implemented digital filters are realized and successfully tested on Altera DE2-115 FPGA board. Finally, three fundamental FIR structures for various filter lengths from 11 to 51 are implemented to compare them in terms of total logic elements, total registers, and total memory.

Index Terms—Altera DE2-115, FIR filter, FPGA, Matlab, Quartus-II.

I. INTRODUCTION

DIGITAL filters, which are one of the most important elements in Electronics Engineering applications such as communication, control, and biomedical systems, are used to remove or enhance selected frequency range in a digital signal. Digital filters are classified as finite impulse response (FIR) and infinite impulse response (IIR) according to the duration of impulse response [1]. FIR filters are very popular because they can be designed as always stable and having exact linear phase.

FIR Digital filters can be implemented on the embedded systems such as microcontroller [2], digital signal processor (DSP) [3], and field programmable gate array (FPGA) [4]. An FPGA is an integrated circuit in which hardware structure can be changed after production according to the desired function.

O. COŞKUN, is with Department of Electrical and Electronics Engineering, Abant İzzet Baysal University, Bolu, Turkey, (e-mail: oguzhanoskun1608@gmail.com) 

✉ K. AVCI, is with Department of Electrical and Electronics Engineering, Abant İzzet Baysal University, Bolu, Turkey, (e-mail: avci_k@ibu.edu.tr) 

Manuscript received August 4, 2017; accepted Dec. 18, 2017.

DOI: 10.17694/bajece.369234

FPGA technology is used in a wide spectrum area from consumer electronics to aerospace and defense industries [5]. FPGA implementation of FIR filters can be provided by a hardware description language (VHDL or Verilog) or schematic description. And, there are recently proposed studies in literature on the implementation of FIR filters on FPGA [6-9], but they require some licensed software package.

In this study, we investigate the FPGA schematic implementations of FIR digital filters for three fundamental structures on Altera DE2-115 FPGA board without requiring any other software packages such as DSP Builder and Matlab Simulink. In Section 2, we briefly introduce FIR filters with their fundamental structures and then the software and hardware tools used in this study. We then describe our proposed FPGA schematic implementations in Section 3. The simulation and realization results for the proposed implementations are given in Section 4. Finally, conclusion part is presented in the last section.

II. MATERIALS AND METHODS

In this section, we first briefly describe the theoretical backgrounds of FIR filters and their fundamental structures. And then, the software tools and FPGA board used in this study are introduced.

A. FIR Filters

A causal N-length (or order with N-1) FIR digital filter can be characterized by the transfer function, $H(z)$, which is the z-transform of the impulse response of the digital filter

$$H(z) = \frac{Y(z)}{X(z)} = \sum_{n=0}^{N-1} h(n)z^{-n} = \sum_{n=0}^{N-1} b_{n+1}z^{-n} \quad (1)$$

where $Y(z)$ and $X(z)$ are z-transforms of the input and output signals of the digital filter, respectively. And, $h(n)$ and b coefficients represent the impulse response and filter coefficients of the digital filter, respectively. For an FIR filter, the impulse response values and the filter coefficients are always the same whereas they are different for an IIR filter.

An FIR filter can also be characterized by the difference equation which gives the relationship between the input and output signals of the digital filter in discrete time domain

$$y(n) = b_1x(n) + b_2x(n-1) + \dots + b_Nx(n-N+1) \quad (2)$$

where $x(n)$ and $y(n)$ represent the input and output signals of the digital filter, respectively.

As compared to IIR filters, FIR filters have two main advantages which are about the stability and linear phase characteristics. FIR filters are always stable, because the poles of the transfer function are always on the origin of the z-plane which mean that they are inside the unit circle. And, FIR filters can be easily designed as having exact linear phase by providing that $h(n)$ is symmetric or antisymmetric.

In literature, four general methods, namely optimization, windowing, frequency sampling, and numerical methods are used to design FIR filters to satisfy a prescribed characteristic [1]. By using a software tool such as Matlab ©, FIR filters can be easily designed, i.e. the filter coefficients can be found.

B. Fundamental FIR Filter Structures

FIR digital filters can be implemented by three fundamental structures known as direct-form, transposed direct-form, and symmetric direct-form. Besides these, they can be implemented by some other structures such as cascade, parallel, lattice, etc. [1]. In all digital filter implementation types, three circuit elements are used. These are the multiplier, adder, and delay.

The circuit for direct-form FIR structure for N length is shown in Fig.1. It is called direct-form because it directly realizes the convolution process of an FIR filter. It is seen from the figure that total number of the delay elements is equal to the filter order ($N-1$), therefore this structure is a canonical type structure [1]. In this structure, the input signal is first delayed by z^{-1} and then multiplied by b coefficients.

The circuit for transposed direct-form FIR structure for N length is shown in Fig.2. It is called transposed direct-form because as opposed to the direct-form the input signal is first multiplied by b coefficients and then delayed by z^{-1} . This structure is also a canonical type structure.

The circuit for symmetric direct-form FIR structure for N length is shown in Fig.3. The number of the multipliers in this structure is half of the ones in other two fundamental structures. This structure can be used only if the filter coefficients are symmetric.

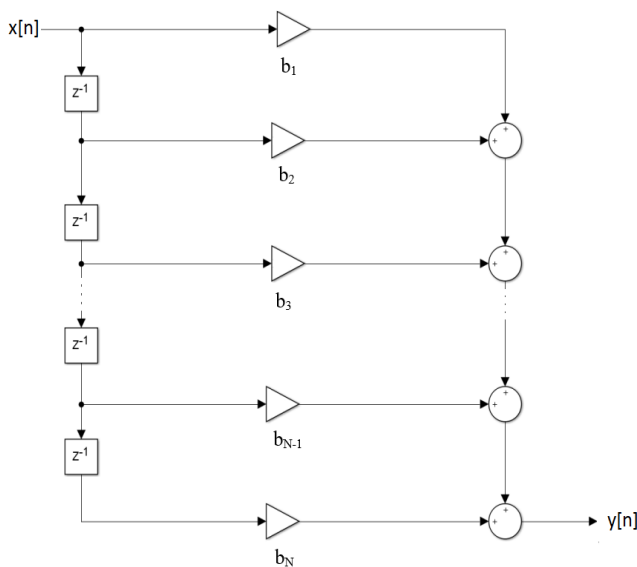


Fig.1. Direct-form FIR structure for N length

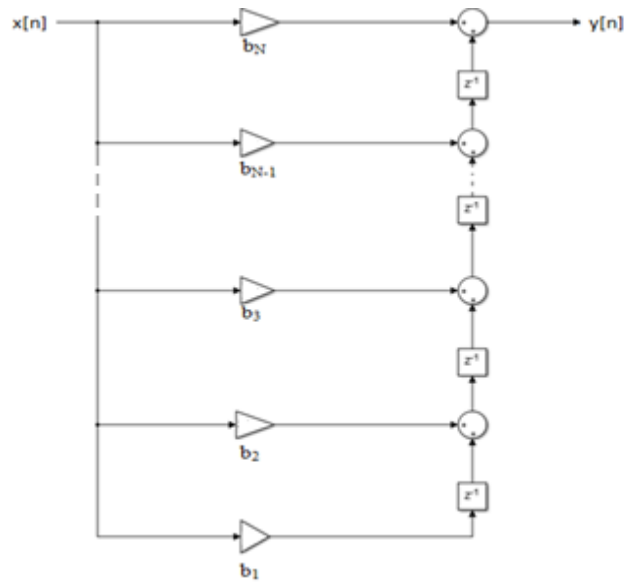


Fig.2. Transposed direct-form FIR structure for N length

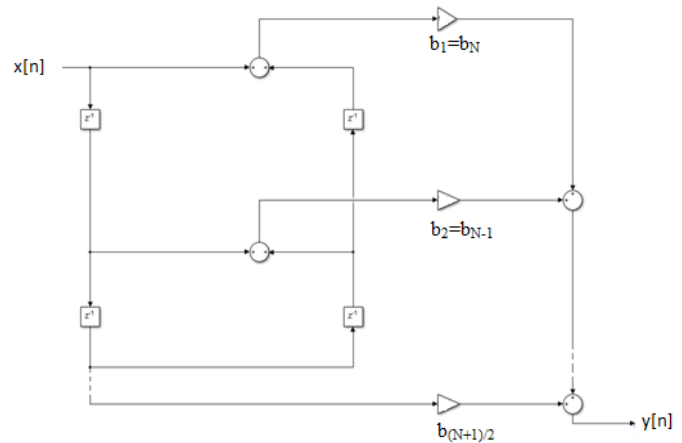


Fig.3. Symmetric direct-form FIR structure for N length

C. Matlab Software

Matlab software produced by the MathWorks Company is one of the most useful software environment for engineers and scientists [10]. In this study, Matlab © 2016a software is used to design and simulate the FIR digital filter to have a reference for the comparison with the FPGA implementation. The digital filters are designed and analyzed in Matlab © software by using a powerful user interface known as fdatool (Filter design and analysis tool).

D. Quartus II Software

The Quartus-II software produced by Altera is a programmable logic device design software, and it enables analysis and synthesis of HDL designs [11]. In this study, Quartus-II is used to implement the digital filters schematically, to compile and simulate the digital filters, and to upload the necessary files to the FPGA board. We use Quartus-II 13.1 64 bit web edition as shown in Fig.4.

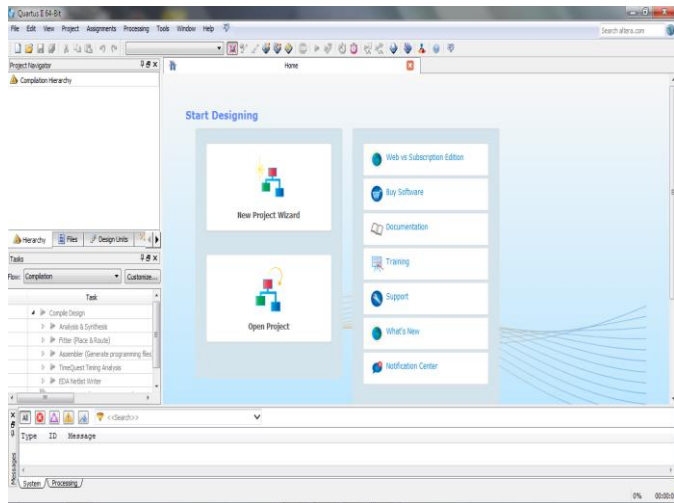


Fig.4. Quartus-II 13.1 web edition

E. Altera DE-2 115 FPGA Board

The DE2-115 board produced by Terasic Company shown in Fig.5 has many features that allow users to implement a wide range of designed circuits, from simple circuits to various multimedia projects [12]. This board is used with Quartus-II software in our study to realize the schematic implemented filter structures.

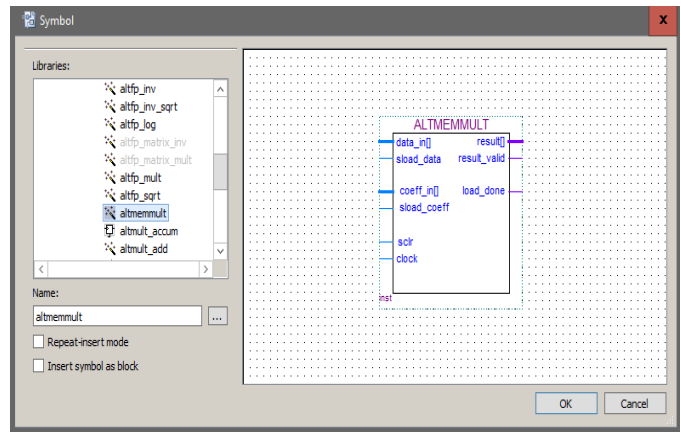


Fig.5. Altera DE2-115 FPGA board

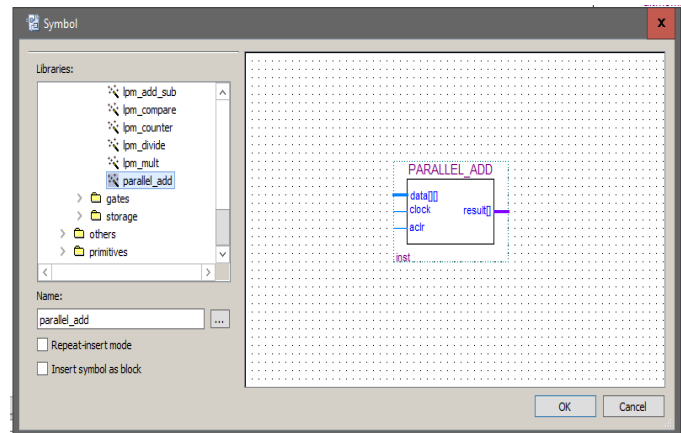
III. SCHEMATIC IMPLEMENTATIONS OF FUNDAMENTAL FIR FILTER STRUCTURES ON QUARTUS II SOFTWARE

In this section, we present the proposed schematic implementations for three fundamental FIR structures.

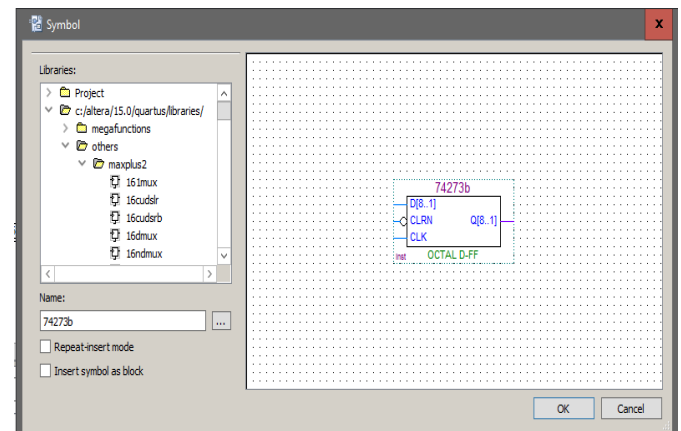
As can be seen from the circuits given by Fig.1, Fig.2, and Fig.3, a digital FIR filter circuit consists of only three digital circuit elements which are multiplier, adder, and delay. Therefore, *altemmult* (Fig.6a), *parallel_add* (Fig.6b), and *74273b D-flip-flop* (Fig.6c) block schemes are chosen from the Quartus II software library for implementing the elements of multiplier, adder, and delay, respectively.



(a)



(b)



(c)

Fig.6. a) *altemmult* for multiplier b) *parallel_add* for adder c) *74273b D-flip-flop* for delay element

Using the block schemes as digital circuit elements shown in Fig.6, an FIR digital filter can be implemented schematically for any filter length. The schematic implementations of three different forms for an FIR filter with the filter length $N=5$ are shown in Fig.7, Fig.8, and Fig.9 for direct, transposed direct, and symmetric direct forms, respectively.

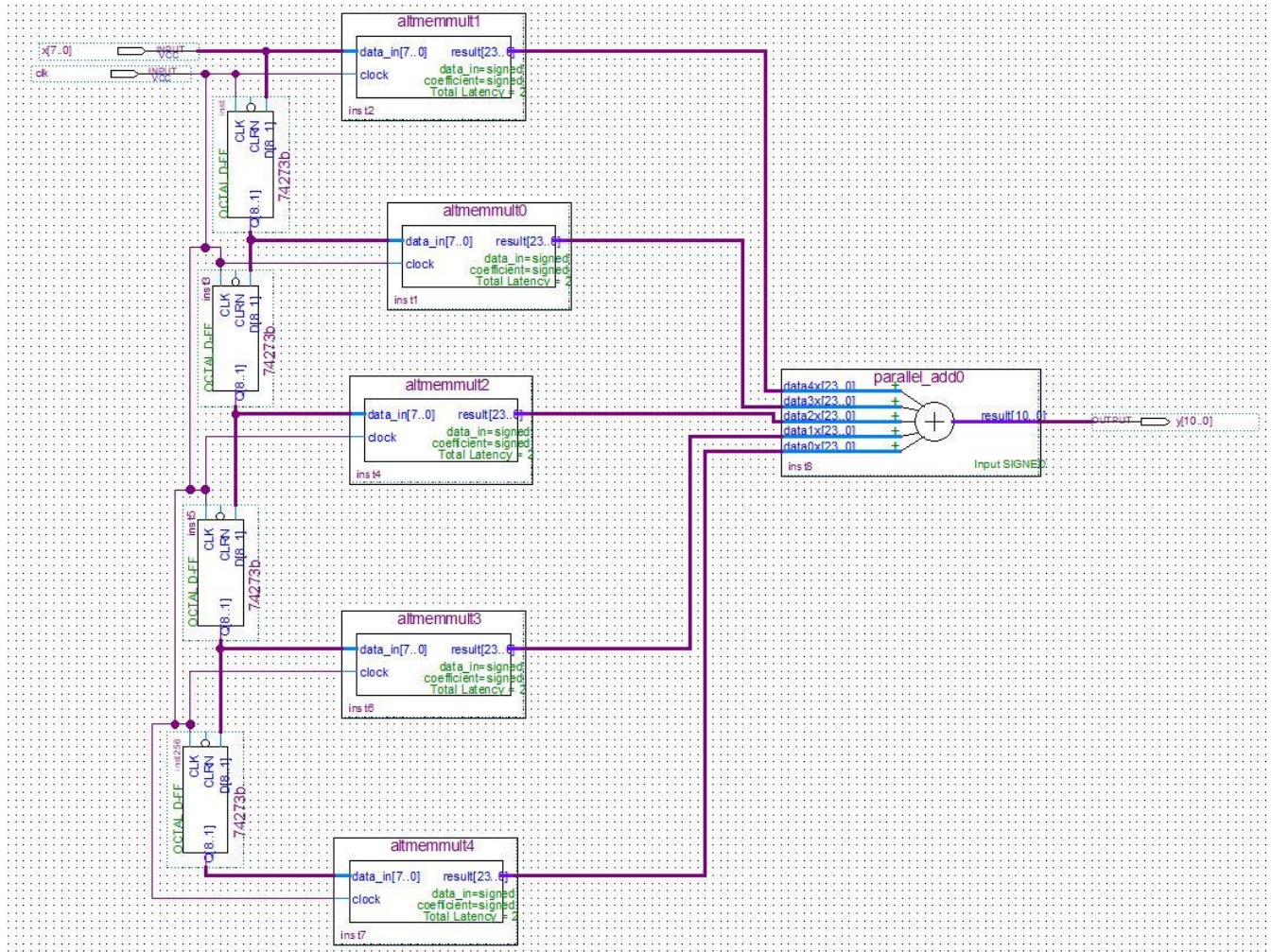


Fig.7. FPGA implementation of direct-form FIR structure for the designed filter with N=5 on Quartus-II

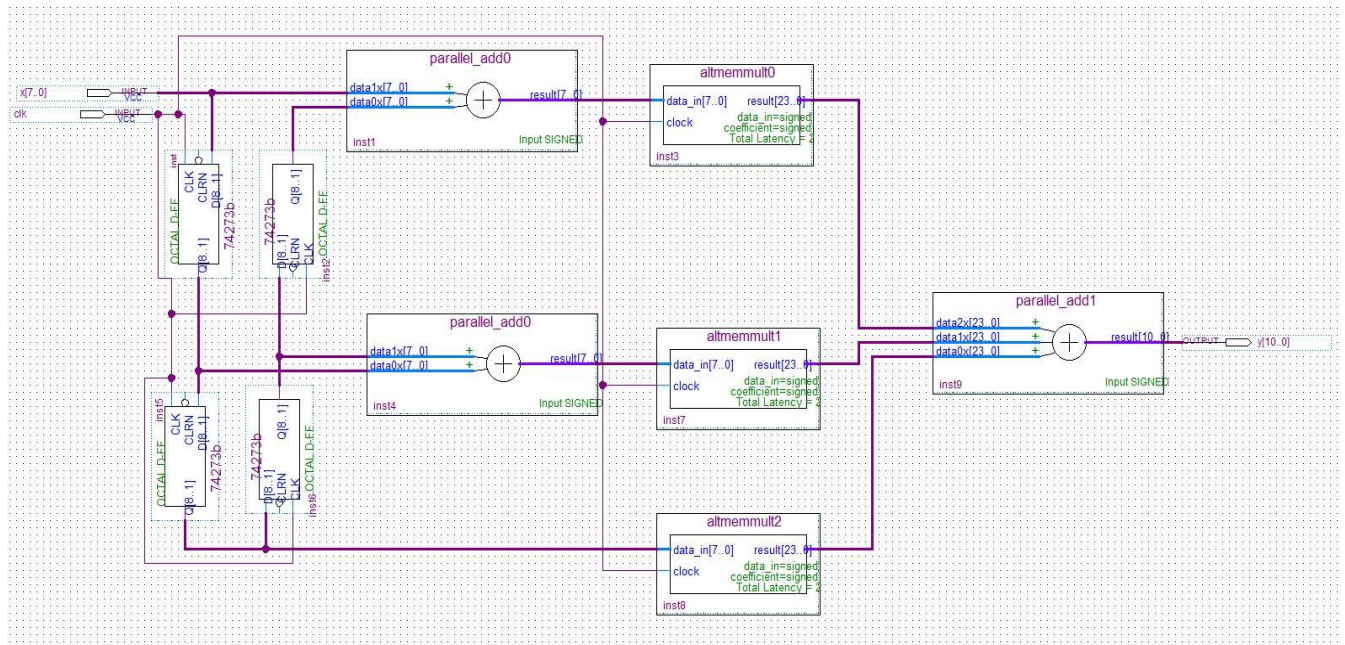


Fig.8. FPGA implementation of transposed direct-form FIR structure for the designed filter with N=5 on Quartus-II

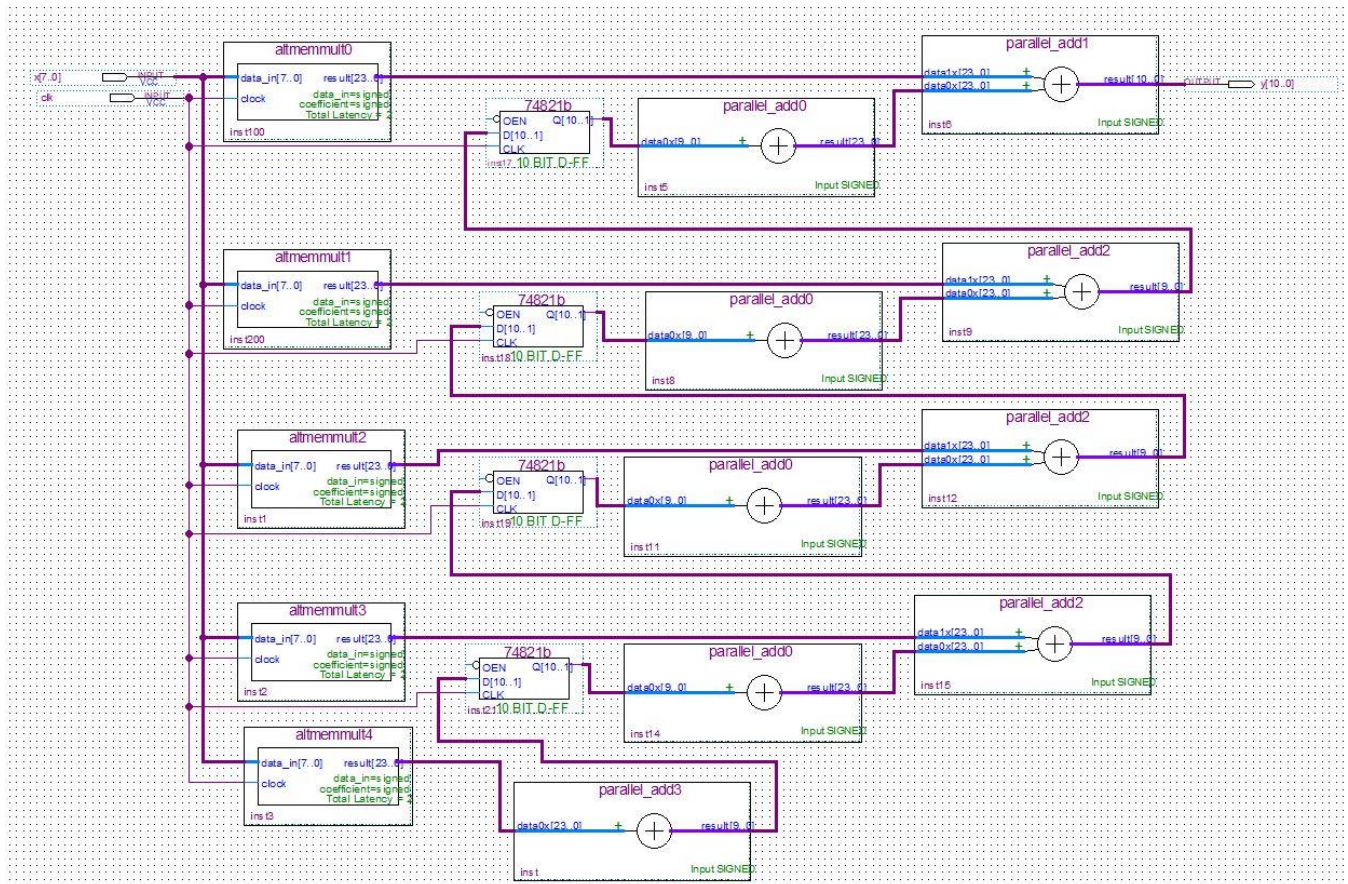


Fig.9. FPGA implementation of symmetric direct-form FIR structure for the designed filter with N=5 on Quartus-II

IV. SIMULATION AND REALIZATION RESULTS

In this section, we present the simulations performed on Matlab and Quartus II environments and then compare with realization performed on the FPGA board.

A. Matlab Simulation Results

To be able to simulate a digital filter and then implement it on an FPGA, we first need to design that filter by using a software program. For this purpose, a lowpass FIR filter based on Kaiser window [13] for $\beta = 1$ is designed by using Matlab fdatool for the filter length $N=5$ (or filter order = 4), sampling frequency $f_s=1000$ Hz, and cut off frequency $f_c=100$ Hz as seen in Fig. 10.

The five non-integer filter coefficients found from the fdatool are given in Fig.11a. These coefficients are then rounded to be integer as in Fig.11b.

The test signal which will be used as an input to the designed filter for the simulation and realization example is shown in Fig.12a. When this input signal is applied to the designed filter which is also defined by its impulse response in Fig.12b, the output signal is obtained as shown in Fig.12c. It is seen that the steady state filtered value is 1000 in decimal which will be used to evaluate the proposed FPGA implementations of the digital filter.

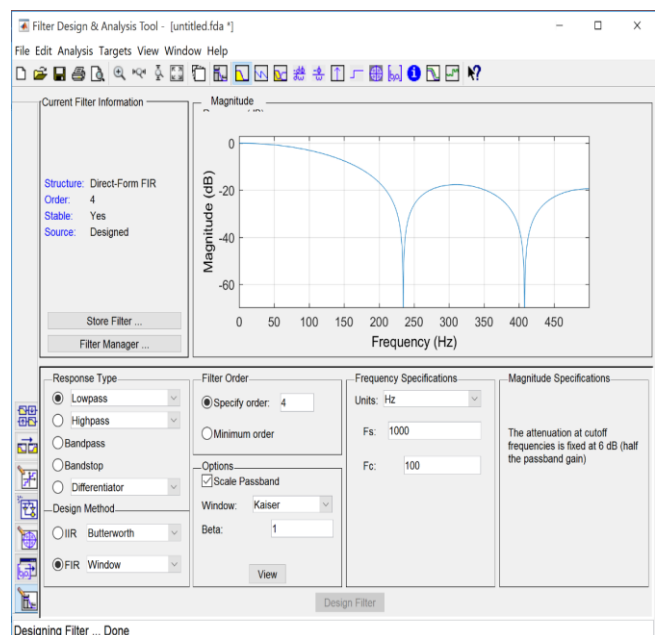


Fig.10. Low pass FIR filter design using Kaiser window [10,11] for window length $N=5$ (or filter order = 4) and cut off frequency $f_c=100$ Hz

```

-Filter Coefficients-
-----
Numerator:
0.15081345405910787
0.22304157717564707
0.25228993753049012
0.22304157717564707
0.15081345405910787
    
```

(a)

```

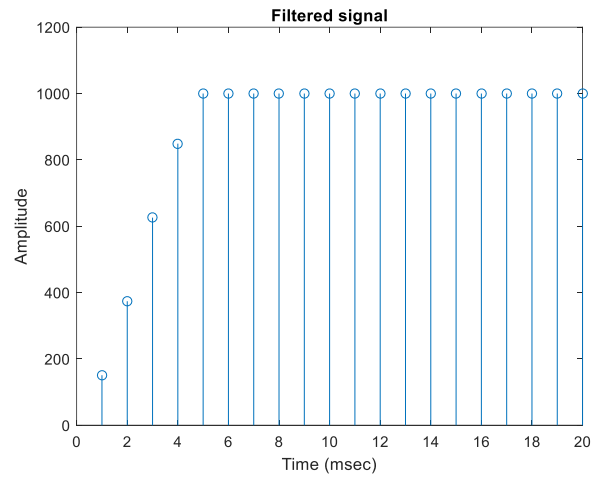
Command Window
New to MATLAB? See resources for Getting Started.
>> b_rounded=round(1000*b)

b_rounded =

    151    223    252    223    151
    
```

(b)

Fig.11. a) Non-integer filter coefficients b) rounded filter coefficients to be integer for the designed filter



(c)

Fig.12. a) input signal, b) impulse response, and c) filtered signal for simulation example of the designed filter for fs=1000 Hz

B. Quartus-II Simulation Results

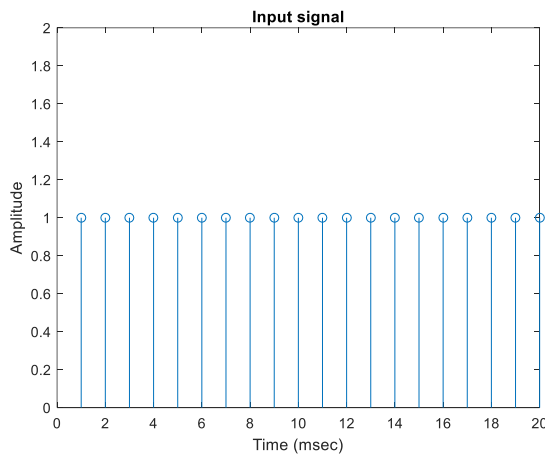
First of all, a Quartus-II project including the schematic implemented direct-form FIR structure given Fig.7 is prepared and then compiled. After that, it is simulated by using *University Program Waveform* in Quartus II. The obtained simulation result is shown in Fig.13.

It is seen from the figure that the output signal has transient values of 0, 151, 374, 626, and 849 and also has a steady state value of 1000. These results are exactly the same as the ones in Matlab simulation given by Fig.12c. Two more Quartus- II projects for the schematic implemented transposed direct and symmetric direct forms of FIR structures given in Fig.8 and Fig.9 are also prepared and then compiled and simulated as in case for the direct-form. It is observed that the simulation results for the transposed direct and symmetric direct forms are also the same as the one given in Fig.13. These simulation results demonstrate that our proposed FPGA schematic implementations for FIR structures given by Fig.7, Fig.8, and Fig.9 are proper implementations.

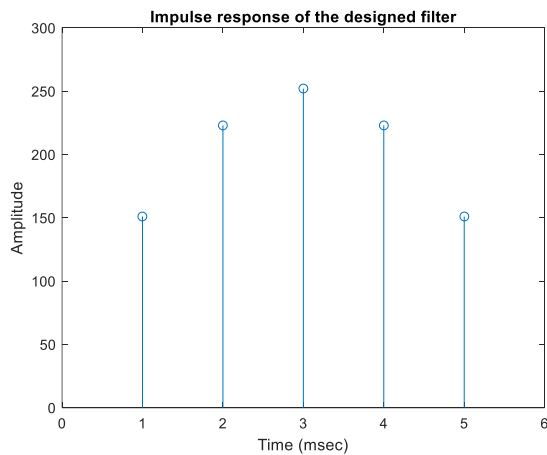
C. Realization on DE-2 115 FPGA Board

To test the schematically implemented FIR structure on FPGA board, first the pins for the input x and output y signals are assigned as shown in Fig.14 by using Assignment Editor in Quartus II. This process results in the switches from SW0 to SW8 on the board to be the input and clock signals, and also in the leds from LEDR0 to LEDR10 to be the output signal.

After making pin assignments, the project for direct-form is compiled again for realization test. Then, by using the programmer interface in Quartus II, the related .sof extended file is loaded to the FPGA board as shown in Fig 15.a. If the loading progress is successful as in Fig 15.b, the realization test can be performed.



(a)



(b)

D. Comparison of Schematic Implementations of FIR Digital Filter Structures for Various Filter Length

In the previous two sections, the simulations and realizations of three different types of the schematic implemented FIR structures for the filter length $N=5$ are successfully carried out. In this section, we perform the same procedures for various filter length ($N=11, 21, 31, 41,$ and 51) to compare the fundamental structures in terms of the total logic, the total registers, and the total memory bits which are obtained from the compiling all the structures on Quartus-II. Since the circuits for implemented structures become more complex and larger in size for the larger filter length, the circuits are not given here. But we observed that all circuits are successfully simulated and realized separately.

Table I shows the total logic elements used for three fundamental FIR structures for various filter lengths. It is seen that the least total logic elements are obtained for transposed direct-form structure. Also, it can be seen that the number of total logic elements used for all three structures increases as the filter length increases.

TABLE I
DATA FOR THE COMPARISON OF THE STRUCTURES IN TERMS OF THE TOTAL LOGIC FOR VARIOUS FILTER LENGTHS

Structures	N=11	N=21	N=31	N=41	N=51
Direct	150	281	360	439	521
Transposed	80	168	248	328	411
Symmetric	124	242	367	492	608

Table II shows the total register elements used for three fundamental FIR structures for various filter lengths. It is seen that the least total register elements are obtained for direct structure. Also, it can be seen that the number of total register elements used for all three structures increases as the filter length increases.

TABLE II
DATA FOR THE COMPARISON OF THE STRUCTURES IN TERMS OF THE TOTAL REGISTERS FOR VARIOUS FILTER LENGTHS

Structures	N=11	N=21	N=31	N=41	N=51
Direct	80	120	120	120	120
Transposed	80	160	240	320	400
Symmetric	80	160	240	320	400

Table III shows the total memory bits used for three fundamental FIR structures for various filter lengths. It is seen that the least total memory bits are obtained for symmetric direct-form structure for lower filter lengths and for direct structure for higher filter lengths. Also, it can be seen that the number of total memory bits used for all three structures increases as the filter length increases.

TABLE III
DATA FOR THE COMPARISON OF THE STRUCTURES IN TERMS OF THE TOTAL MEMORY BITS FOR VARIOUS FILTER LENGTHS

Structures	N=11	N=21	N=31	N=41	N=51
Direct	22528	32848	33008	33168	33328
Transposed	22528	43008	63488	83968	104448
Symmetric	12288	22528	32768	43008	53248

V. CONCLUSION

In this study, FPGA schematic implementations for three different fundamental structures of FIR digital filters are investigated. To have a reference result for the comparisons, we first provide a simulation example on Matlab for the filter length $N=5$ for an input signal. Then, three FIR structures are schematically implemented on Quartus-II for $N=5$.

After that, three FIR structures for $N=5$ are simulated using the universal waveform tool in Quartus-II. It is shown that the simulation results of Quartus-II are the same as those of Matlab, which means our proposed schematic implementations are proper successful implementations.

Then, our schematic implementations are tested on Altera DE2-115 FPGA board. The realization results also demonstrate that our proposed implementations are successful.

Moreover, we implement three fundamental FIR structures for various filter lengths from 11 to 51 to compare them in terms of total logic elements, total registers, and total memory by compiling them on Quartus-II. We conclude that the least total logic elements and registers are obtained for transposed direct-form and direct-form structures, respectively. As for the least total memory bits, the best results are obtained for symmetric direct-form structure for lower filter lengths and for direct structure for higher filter lengths.

ACKNOWLEDGMENT

This study is supported by the Scientific Research Projects Unit of Abant Izzet Baysal University with the project number 2016.09.03.1009.

Also, this study is partly presented in ICENS 2016 and published as an abstract [14].

REFERENCES

- [1] A. Antoniou, *Digital Signal Processing: Signal, Systems, and Filters*. New York: McGraw-hill, 2005.
- [2] B. K. A. Ramu, "Implementing FIR and IIR Digital Filters Using PIC18 Microcontrollers", Microchip Application Notes, pp.1-46, 2002.
- [3] C. L. Hu, "Design and Verification of FIR Filter Based on Matlab and DSP", International Conference on Image Analysis and Signal Processing (IASP), 9-11 Nov., Hangzhou, China, pp. 286-289, 2012.
- [4] I. Thingom, P. Khundrakpam, "FPGA implementation of FIR filter using RADIX-2", International Conference on Wireless Communications, Signal Processing and Networking (WiSPNET), 23-25 March, Chennai, India, pp. 1524-1528, 2016.
- [5] S. Karataş, E. Saritas, *Her yönüyle FPGA ve VHDL*. Palme Yayıncılık, 2003.
- [6] V. H. Deshmukh, A. Mishra, A.S. Bhalchandra, "FIR Filter Design on Chip Using VHDL" IPASJ International Journal of Computer Science. Vol. 2, No. 7, July, pp 12-16, 2014.
- [7] R. M. Narsale, D. Gawali, A. Kulkarni, "FPGA Based Desing & Implementation of Low Power FIR Filter for ECG Signal Processing" IJSETR International Journal of Science, Engineering and Technology Research. Vol.3, No. 6, June, pp 1673-1677, 2014.
- [8] K. Aboutabikh, I. Haidar, A. Garib, "Design and Implementation of a Digital FIR LFP with Variable Pass-Band for ECG Signal using FPGA" International Journal of Advanced Research in Computer and Communication Engineering. Vol.4, No. 9, September, pp 275-281, 2015.
- [9] K. Aboutabikh, N. Aboukerdah, "Design and Implementation of a Multiband Digital Filter Using FPGA to Extract the ECG Signal in the Presence of Different Interference Signals" Computers in Biology and Medicine, Vol. 62, pp.1-13, 2015.
- [10] https://www.mathworks.com/products.html?s_tid=gn_ps
- [11] <https://www.altera.com/downloads/download-center.html>
- [12] www.terasic.com.tw/_sub/de2-115

- [13] J. F. Kaiser, Nonrecursive digital filter design using I_0 -sinh window function. *Proc. IEEE Int. Symp. Circuits and Systems (ISCAS'74)*, San Francisco, Calif, USA, April, 20-23, 1974.
- [14] O. Coşkun, K. Avci, "Schematic Implementations of FIR Digital Filters on Altera FPGA", 2016 Book of Abstracts: 2nd International Conference on Engineering and Natural Sciences (ICENS 2016), 24-28 May, Srajevo, Bosnia and Herzegovina, pp. 664, 2016, (Abstract)

BIOGRAPHIES



OĞUZHAN COŞKUN was born in Bursa, Turkey, in 1995. He received the B.S. degree in electrical and electronics engineering from Abant İzzet Baysal University, Turkey in 2016. Currently, he is a graduate student at the same department since February 2017. His current research interests are digital filters and FPGA implementation.



KEMAL AVCI was born in Adiyaman, Turkey, in 1980. He received the B.S., M.S., and Ph.D. degrees in electrical and electronics engineering from the University of Gaziantep, Turkey in 2002, 2004, and 2008, respectively. Also, from 2003 to 2008, he worked as a research assistant at the same department. Currently, he works as an assistant professor since 2008 in electrical and electronics engineering in Abant İzzet Baysal University, Turkey. His main research interests are design and implementation of digital filters and filter banks, two dimensional digital filters, audio & music signal processing, and switched capacitor networks.

Optimal Tuning of PID Controller Using Grey Wolf Optimizer Algorithm for Quadruped Robot

M. A. Şen, and M. Kalyoncu

Abstract—The research and development of quadruped robots is grown steadily in during the last two decades. Quadruped robots present major advantages when compared with tracked and wheeled robots, because they allow locomotion in terrains inaccessible. However, the design controller is a major problem in quadruped robots because of they have complex structure. This paper presents the optimization of two PID controllers for a quadruped robot to ensure single footstep control in a desired trajectory using a bio-inspired meta-heuristic soft computing method which is name the Grey Wolf Optimizer (GWO) algorithm. The main objective of this paper is the optimization of K_P , K_I and K_D gains with GWO algorithm in order to obtain more effective PID controllers for the quadruped robot leg. The importance to this work is that GWO is used first time as a diversity method for a quadruped robot to tune PID controller. Moreover, to investigate the performance of GWO, it is compared with widespread search algorithms. Firstly, the computer aided design (CAD) of the system are built using SolidWorks and exported to MATLAB/SimMechanics. After that, PID controllers are designed in MATLAB/Simulink and tuned gains using the newly introduced GWO technique. Also, to show the efficacy of GWO algorithm technique, the proposed technique has been compared by Genetic Algorithm (GA) and Particle Swarm Optimization (PSO) algorithm. The system is simulated in MATLAB and the simulation results are presented in graphical forms to investigate the controller's performance.

Index Terms—Quadruped Robot, PID controller, Optimization, Gait definition, Grey Wolf Optimizer, Genetic Algorithm, Particle Swarm Optimization, Trajectory Tracing.

I. INTRODUCTION

TRACEKED and wheeled robots can travel very fast only on fairly flat floors. However, they can move slower than legged robots on rougher terrains. Quadruped robots have the advantages of the strong obstacle capability, less energy consumption, high flexibility, good stability and locomotion on uneven and rough terrain, do little damage to the environment etc. So, quadruped robots are an important place in robotic and their popularity are increasing. Nevertheless, quadruped robots have more complicated structure and it is more difficult to control than tracked and wheeled robots.

M.A. ŞEN, is with Department of Mechanical Engineering University of Selçuk University, Konya, Turkey, (e-mail: marifsen@selcuk.edu.tr) 

M. KALYONCU, is with Department of Mechanical Engineering University of Selçuk University, Konya, Turkey, (e-mail: mkalyoncu@selcuk.edu.tr) 

Manuscript received September 6, 2017; accepted January 11, 2018.
DOI: [10.17694/bajece.401992](https://doi.org/10.17694/bajece.401992)

Therefore, the controller design is more important for quadruped robots. A robust controller is necessary for the stability analysis and trajectory planning of the system for quadruped robots.

There are a lot of current studies about quadruped robots. For example; BigDog [1] is developed by Boston Dynamics, ANYmal [2] is developed by Hutter et al., Jinpong [3] is developed by Cho et al., HyQ2Max [4] is developed by Semini et al.

The PID controller operates the large share of the control system in the world. Tuning of PID gains using a search algorithm is ensure better response more than traditional methods such as trial-error methods and Ziegler-Nichols method. Detail studies about the optimization of PID controllers are available in the literature. Das et.al. [5] designed a PID controller for an adopted second order DC motor system and they used the evolutionary algorithm based on GWO algorithm to optimize the PID controller. Madadi and Motlagh [6], GWO Algorithm is utilized and designed for DC Motor drive to discover the global optimum solution in search space. Kanojiya and Meshram [7], present a method to determine the optimal PI controller gains on DC motor drive system using PSO algorithm.

Moura Oliveira [8], The GWO algorithm is proposed a PID controllers design using two degrees of freedom control configuration. Verma et.al. [9], presents a novel evolutionary technique which is the GWO algorithm to optimize the parameters of fractional order controller. Lal et.al. [10], present a meta-heuristic optimization algorithm has been applied to interconnected Hydro-thermal power system for automatic generation control. The optimal gains of the fuzzy based PID controllers are obtained by employing the proposed GWO algorithm. Tsai et.al. [11], proposed a novel multi-objective method for optimal robot path planning which based on GWO algorithm. Razmjoo et. al. [12] tuned a LQR controller using GWO algorithm for a single-link flexible joint robot manipulator. Hultmann and do Santos [13], developed a multi-objective non-dominated sorting GA for the tuning of a PID controller applied to a robotic manipulator. Krohling and Rey [14] present a PID controller based on GA for solving the constrained optimization problem in a servo motor system.

This paper examines evaluates the performance of an optimized two PID controllers using GWO algorithm, PSO algorithm and GA for single footstep controlling the quadruped robot in a desired trajectory. The quadruped robot is built SolidWorks and exported to MATLAB/SimMechanics environment. The control system is modelled MATLAB/Simulink environment and PID controllers are tuned with proposed algorithms. The main aim is to use a search algorithm include GWO algorithm,

PSO algorithm and GA to design a suitable PID controllers for the quadruped robot system. Also, a comparison between the tuning techniques presents to show the best method.

Followed by introduction the paper is created as follows: the model of the quadruped robot is explained in Section 2. Section 3, describes GWO algorithm, PSO algorithm and GA. In section 4, designing the PID controllers optimally for the quadruped robot is shown; applying of the described algorithms is also presented in this section. Simulation results and comparisons are presented in section 5. Finally, in section 6, the paper is concluded.

II. MODELLING OF QUADRUPED ROBOT

This chapter presents the specifications of the quadruped robot. The computer aided design (CAD) model of the quadruped robot system built in SolidWorks software. The model which mainly based on the inspiration by nature and other robots shows in Figure 1. The robot has four legs with three DOF of each leg. This structure is simple and allows the robot to perform a wide range of tasks. The physical parameters of the system are given in Table 1. Physical specifications describe the robot's size and weight.

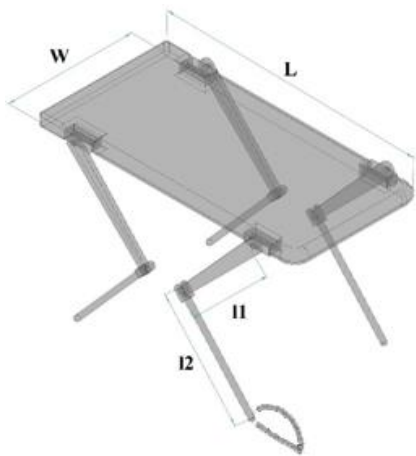


Figure 1: The CAD model of system

TABLE I
THE PHYSICAL PARAMETERS OF SYSTEM

Parameter	Value
Material	Alloy 1060
Weight	28.7 kg
W	500 mm
L	1000 mm
I1	400 mm
I2	410 mm

III. DESCRIBED PROPOSED ALGORITHMS

In this section, GWO algorithm, PSO algorithm and GA summarized. In this paper, the proposed algorithms are used to tune of PID controller gains to provide a single footstep control in a desired trajectory for the quadruped robot.

A. Grey Wolf Optimizer (GWO) Algorithm

GWO algorithm [15 - 19] is a new meta-heuristic algorithm which is introduced in 2014 by Mirjalili et al. The GWO algorithm mimics the leadership hierarchy and hunting mechanism of the grey wolves in the wild. The method simulates the social hierarchy and hunting behaviour in the society of grey wolves. Four types of simulations are applied in grey wolf hierarchy: *Alpha* (α), *Beta* (β), *Delta* (δ) and *Omega* (ω) as shown in Figure 2. The *Alpha* (α) wolf which leaders of whole group is mostly responsible for making decisions about hunting, sleeping place, time to wake etc. *Beta* (β) wolf which subordinate of *Alpha* (α) wolves is found in the second rank in the hierarchy. *Beta* (β) wolf is known as an *Alfa* (α) assistant in decision to hunting and other activities. The lowest ranking grey wolf is *Omega* (ω) wolf which follow *Alphas* (α), and *Betas* (β), but dominate *Omegas* (ω). If a wolf is not an *Alpha* (α), *Beta* (β), or *Omega* (ω), it is called *Delta* (δ) wolf. The search in GWO starts with wolves' population (solutions) which are generated randomly. These wolves estimate the location of prey (optimum) through an iterative procedure in during the hunting (optimization) process. *Alpha* (α) is the fittest solution followed by *Beta* (β) and *Delta* (δ) as the second and third best solutions. The rest of the solutions are least important and considered as *Omega* (ω) [15].

The hunting behavior is mainly divided into three steps [15]:

- Tracking, chasing and approaching the prey.
- Encircling and harassing the prey until it stops moving.
- Attacking the prey.

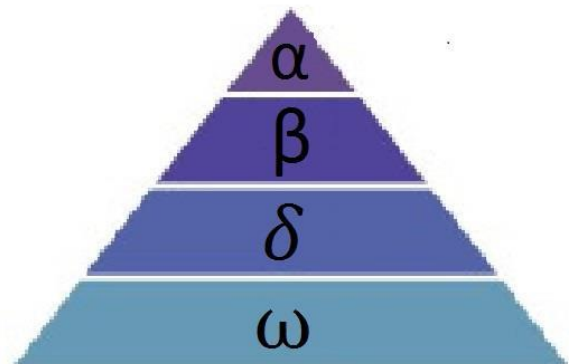


Figure 2: The grey wolf hierarchy [15]

The following equations are proposed in order to mathematically model the encircling behaviour:

$$\vec{D} = |\vec{C}\vec{X}_p(t) - \vec{X}(t)| \quad (1)$$

$$\vec{X}(t+1) = \vec{X}_p(t) - \vec{A}\vec{D} \quad (2)$$

where t is the current iteration, \vec{A} and \vec{C} are coefficient vectors, $\vec{X}_p(t)$ represents the position vector of the victim. \vec{X} indicates the position vector of a grey wolf. The vectors \vec{A} and \vec{C} calculated as follows:

$$\vec{A} = 2\vec{a}\vec{r}_1 - \vec{a} \quad (3)$$

$$\vec{C} = 2\vec{r}_2 \quad (4)$$

where \vec{a} include are linearly decreased from 2 to 0 over the course of iterations and \vec{r}_1 and \vec{r}_2 are random vectors in the range [0, 1].

In GWO, the first three obtained best solutions are saved so far and compel the other search agents (including the omegas) to update their positions due to the position of the best search agents. For this regard, the following formulas are proposed.

$$\vec{D}_\alpha = |\vec{C}_1\vec{X}_\alpha - \vec{X}|, \vec{D}_\beta = |\vec{C}_2\vec{X}_\beta - \vec{X}|, \vec{D}_\delta = |\vec{C}_3\vec{X}_\delta - \vec{X}| \quad (5)$$

$$\vec{X}_1 = \vec{X}_\alpha - \vec{A}_1(\vec{D}_\alpha), \vec{X}_2 = \vec{X}_\beta - \vec{A}_2(\vec{D}_\beta), \vec{X}_3 = \vec{X}_\delta - \vec{A}_3(\vec{D}_\delta) \quad (6)$$

$$\vec{X}(t+1) = \frac{\vec{X}_1 + \vec{X}_2 + \vec{X}_3}{3} \quad (7)$$

Pseudo code of the GWO is shown the Figure 3. In GWO algorithm, the mathematical models of the social hierarchy consist of; tracking, encircling, and attacking prey are description in Mirjalili et al. study [15]. The parameters of GWO algorithm are given in Table 2.

```

Initialize the grey wolf population  $X_i (i = 1, 2, \dots, n)$ 
Initialize  $a$ ,  $A$ , and  $C$ 
Calculate the fitness of each search agent
 $X_\alpha$ =the best search agent
 $X_\beta$ =the second best search agent
 $X_\delta$ =the third best search agent
While ( $t < \text{Max number of iterations}$ )
    for each search agent
        Update the position of the current search agent by equation (7)
    end for
    Update  $a$ ,  $A$ , and  $C$ 
    Calculate the fitness of all search agents
    Update  $X_\alpha$ ,  $X_\beta$  and  $X_\delta$ 
     $t = t + 1$ 
end while
return  $X_\alpha$ 
    
```

Figure 3: Pseudo code of the GWO algorithm [15]

TABLE II
GREY WOLF OPTIMIZER PARAMETERS

Maximum Iteration	100
Number of Search Agent	30

B. Particle Swarm Optimization (PSO)

PSO algorithm [20] which is inspired by social behaviour of bird flocking or fish schooling is one of the most popular optimization algorithms which have been developed in 1995 by Kennedy and Eberhart. In this approach optimal solution to a mathematical optimization problem is restricted of birds behave in the moment the food pursue, the escape from hunters and the search for mates. In the last years, PSO algorithm has been employed in wide variety of applications ranging from classical mathematical programming problems to scientific optimization problems and highly proprietary engineering [21, 22].

Traditional PSO algorithm starts with an initial population (swarm) of candidate solution (particles). The particles look for throughout the search space because of defined formulations. In the wake of seeking, the particles move to their own best known position in the search space and the swarm's best known position. The particles will the guide the other particles movements after finding the best position. Until the satisfactory solution will finally be detected, the searching about the search space is repeated. In each iteration, the swarm is tuned in order to the following equations:

$$v_i^{t+1} = \omega v_i^t + c_1 r_1 (p_i^t - x_i^t) + c_2 r_2 (g_i^t - x_i^t) \quad (8)$$

$$x_i^{t+1} = x_i^t + v_i^{t+1} \quad i=1,2,\dots,n \quad (9)$$

Where, t is the iteration number, n is the number of particles, C_1 and C_2 are the positive constants, w is the weighted inertia, r_1 and r_2 are two random numbers distributed within the range [0,1], p_i is the best position of the i th particle and g_i is the best particle among the group members. The parameters of PSO algorithm are given in Table 3.

TABLE III
PARTICLE SWARM OPTIMIZATION PARAMETERS

Number of Particle (NoP)	30	
Maximum Iteration	100	
Velocity Clamping Parameter (V_{max})	6	
Inertia Weight	w_{init}	0.2
	w_{final}	0.9
The Importance of Personal Best Value (c_1)	2	
The Importance of Neighbourhood Best Value (c_2)	2	

C. Genetic Algorithm (GA)

The Genetic Algorithm [23] is an extensively used optimization method based on the process that mimics natural selection and genetics.

In this study, GA Global Optimization Toolbox which is a one of the built-in method in MATLAB Global Optimization Toolbox [24] is used. MATLAB Global Optimization Toolbox is a powerful tool to solve optimization problems. The parameters of GA are given in Table 4.

TABLE IV
GENETIC ALGORITHM PARAMETERS

Population Size	30
Elite Count	5
Generations	100
Crossover Fraction	0.8

IV. DESIGNING AND OPTIMIZATION OF THE PID CONTROLLERS

In this section, the description of the designing of the PID controllers of the quadruped robot system using GWO algorithm, PSO algorithm and GA is given. Initially, the computer aided design (CAD) of the system are built using SolidWorks and exported to MATLAB/SimMechanics software. The MATLAB/ SimMechanics model of the system is given in Figure 4. The PID controllers are designed in MATLAB/Simulink. Inverse kinematic solutions are used to obtain upper (hip) and lower (knee) leg angular positions from trajectory coordinates. The PID controller model of the quadruped robot is given in Figure 5.

The aim is to search for the optimal values of the gains of PID controllers with respect to a determined objective function which consist of trajectory coordinates. The objective function (J) is:

$$J = norm\sqrt{|X_{ref} - X|^2 + |Y_{ref} - Y|^2} \tag{10}$$

where X_{ref} and Y_{ref} are the reference coordinate of the trajectory, X and Y are the realized trajectory in simulations. GWO algorithm, PSO algorithm and GA are employed for optimizing the proposed fitness function. The optimisation ranges of gains are set as shown in Table 5.

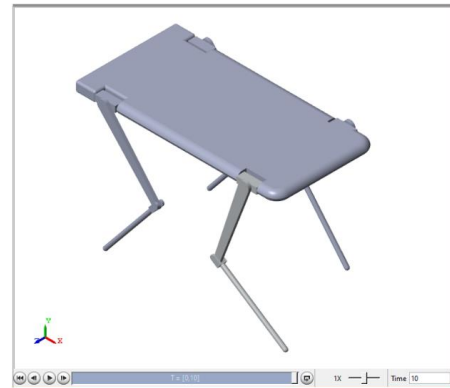


Figure 4: The MATLAB/SimMechanics model of system

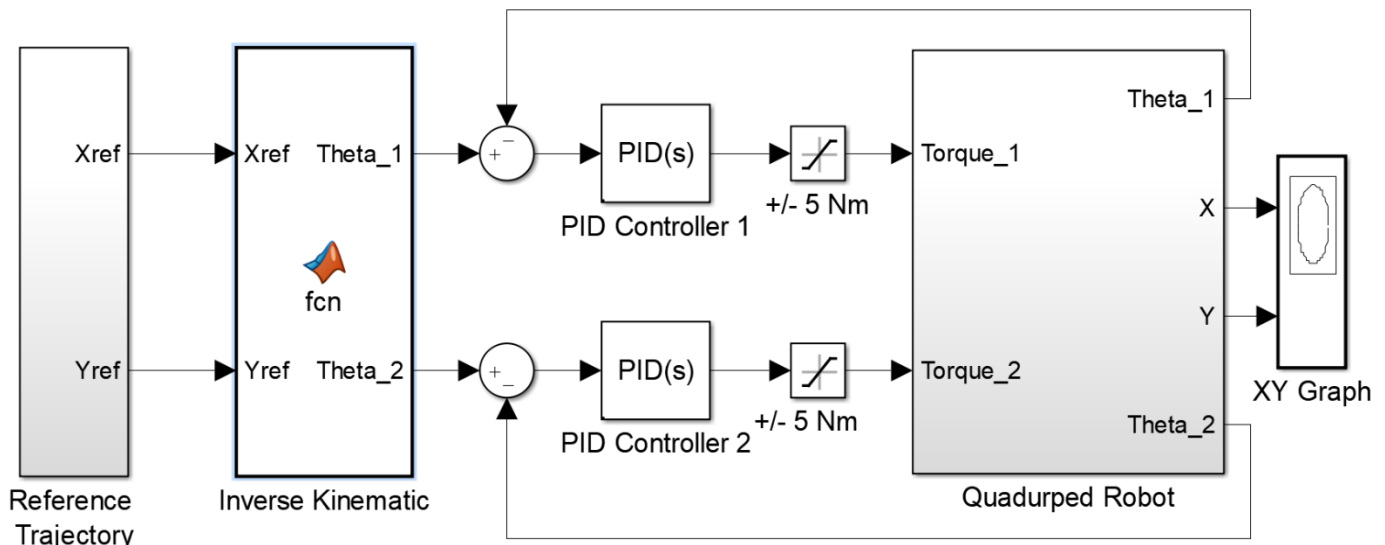


Figure 5: The PID controller model of system

TABLE V
THE RANGE OF PID CONTROLLER'S GAINS

	PID 1			PID 2		
	Kp	Ki	Kd	Kp	Ki	Kd
Min.	0	0	0	0	0	0
Max.	1000	1000	1000	1000	1000	1000

V. SIMULATION RESULTS

GWO algorithm and PSO algorithm are programmed in MATLAB environment and GA which is a tool in MATLAB Global Optimization Toolbox run on an Intel(R) Core(TM) i7-4700HQ CPU 2.40 GHz PC with 16.0 GB memory separately. The proposed algorithms run offline for 100 iterations to find the minimum value of the cost function that defined as the objective function (J). After optimization, the best set of the

PID controller's gains values corresponding to the minimum objective function value provided by the optimal GWO algorithm, PSO algorithm and GA are given in Table 6. Also, the minimum objective function value (Best Value) and elapsed time in optimizations are shown in Table 6. The system simulated with tuned gains of the PID controls and the snapshots from MATLAB/SimMechanics simulations are demonstrated in Figure 6. In simulations, upper (hip) and lower (knee) leg angular positions (Theta 1 and Theta 2) are given in Figure 7 and Figure 8. It is clear from the graphics, the proposed algorithms realized in a similar way.

Tracing trajectory performances of the proposed algorithms simulated in MATLAB/Simulink environment. As seen in Figure 9, PID controllers which tuned with GWO algorithm, PSO algorithm and GA ensure settling on the path very successfully. The performances of the proposed algorithms are

similar. However, as seen in Figure 10, the GWO algorithm traced trajectory with less errors than the others. Objective function convergence performances of the GWO algorithm, PSO algorithm and GA are graphically illustrated in Figure 11. As seen obviously, GWO algorithm is converged better at the

end. Moreover, PSO algorithm and GA are converged slower than GWO algorithm. In other terms, GWO algorithm is given better solutions at finding global search and local search according to PSO algorithm and GA.

TABLE VI
THE TUNED GAINS OF PID CONTROLLERS

	PID 1			PID 2			Best Value(J)	Elapsed time (s)
	Kp	Ki	Kd	Kp	Ki	Kd		
GWO	493.3	0.0556	8.05	93.73	21.92	3.91	63.94	1854,59
PSO	932.50	615.00	34.85	117.40	271.36	173.95	67.93	2025.94
GA	81.65	2.54	465.37	47.78	595.40	247.91	74.14	2342.48

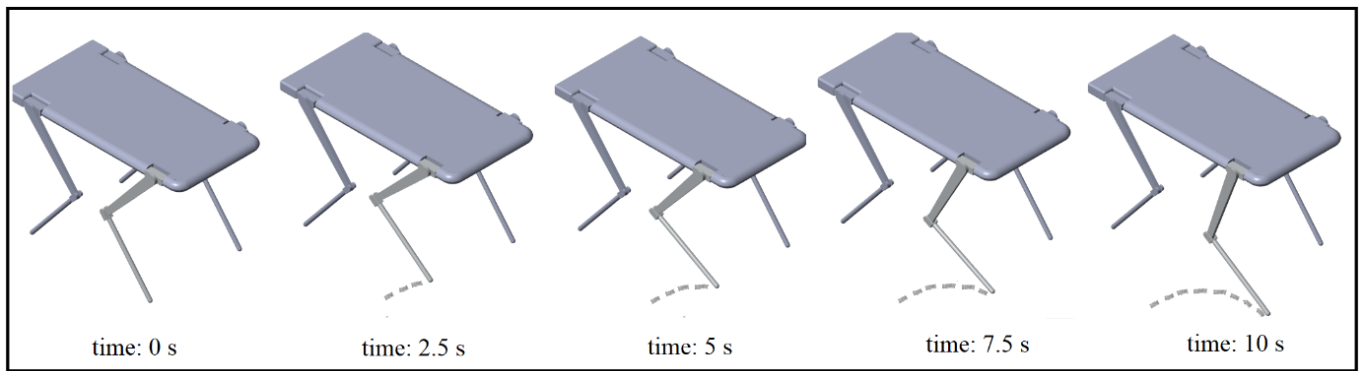


Figure 6: Snapshots from the simulations

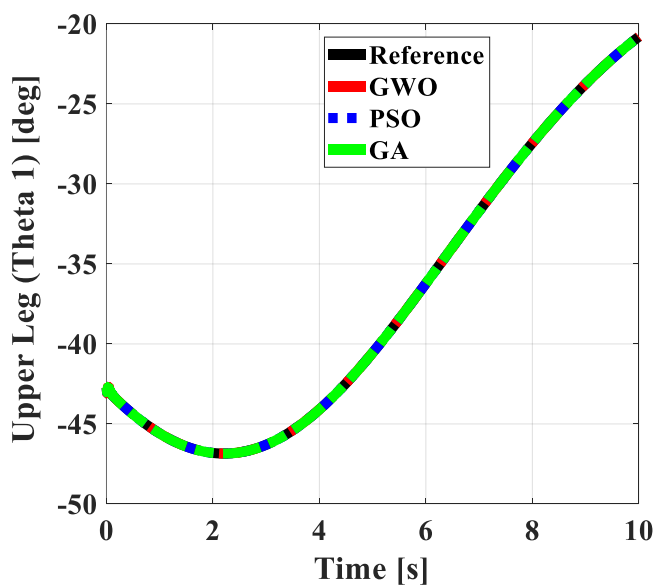


Figure 7: Upper leg angular position of quadruped robot

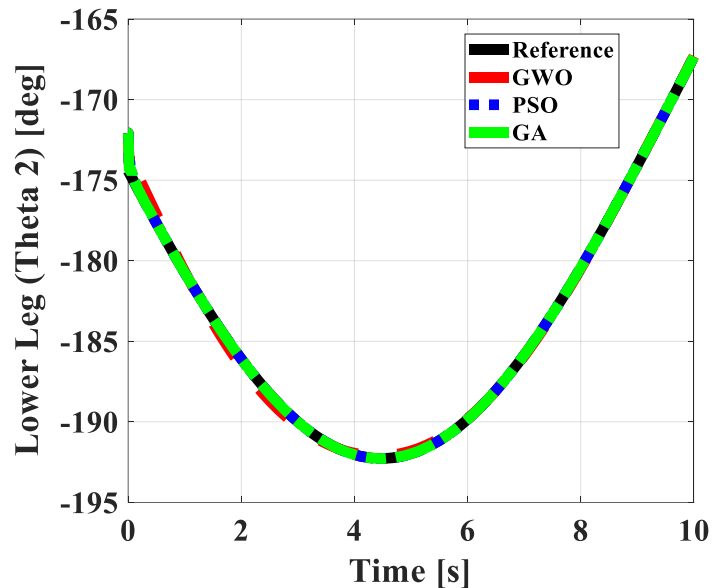


Figure 8: Lower leg angular position of quadruped robot

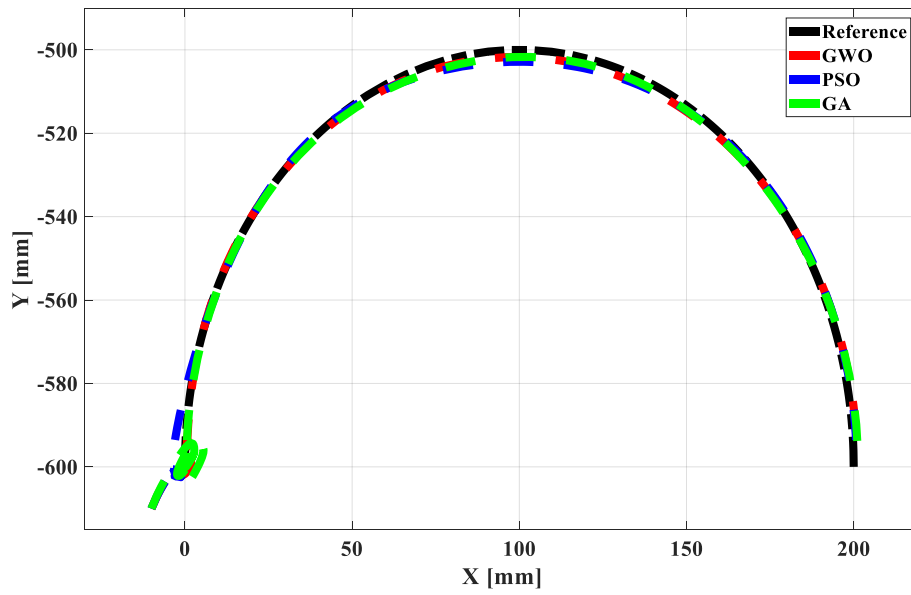


Figure 9: The control performance of the proposed algorithms in trajectory

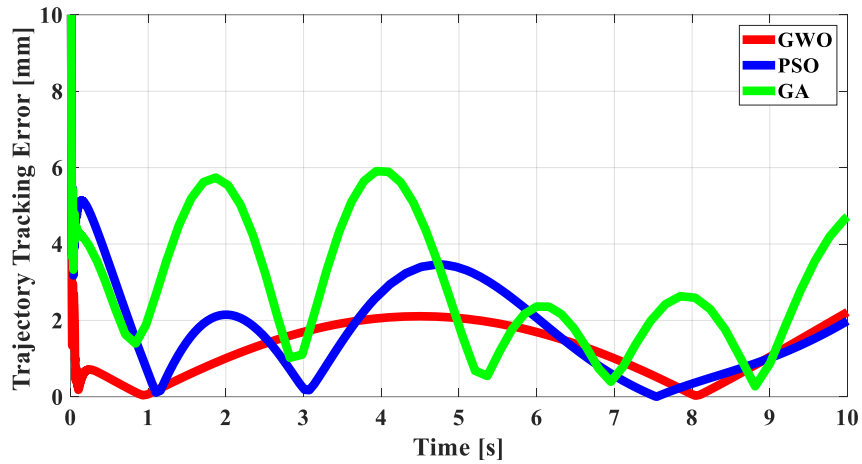


Figure 10: The trajectory tracking error of proposed algorithms

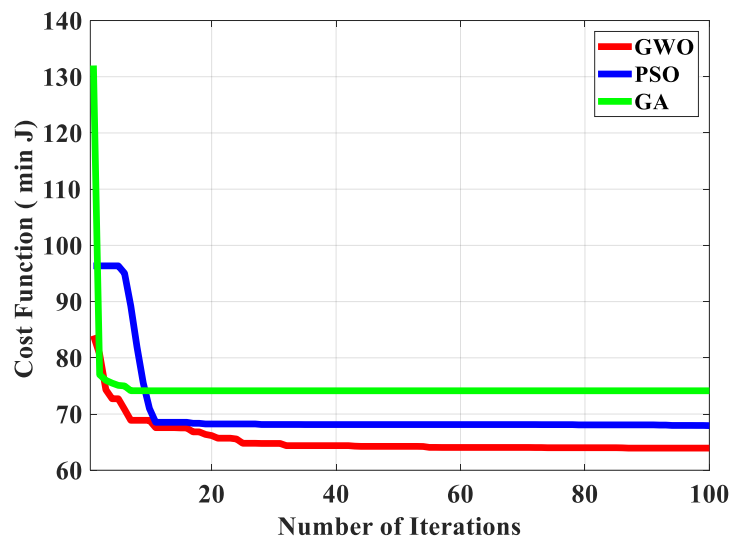


Figure 11: The performance analysis of proposed algorithms

VI. CONCLUSIONS

In this paper, the optimization of the PID controllers for the quadruped robot to ensure a single footstep control in a desired trajectory using GWO algorithm, PSO algorithm and GA are investigated by simulations. The importance of this work is that GWO is used first time as a diversity method for a quadruped robot to tune PID controllers. Moreover, to investigate the performance of GWO, it is compared with widespread search algorithms. The GWO algorithm has been successfully applied to design of the PID controllers. In order to demonstrate the performances of GWO algorithm, it is compared with commonly used search algorithms; PSO algorithm and GA. The proposed algorithms are used to find the optimal PID controller gains for the optimum controller performance over the quadruped robot. The simulation results show that GWO algorithm is faster and more efficiency than PSO algorithm and GA in global and local search in optimization. In this study, the GWO algorithm is the best which illustrated satisfactory performances toward PSO algorithm and GA. However, the tuned PID controllers with all the proposed algorithms performed trajectory control of the system successfully and their performances realized similar. It is anticipated that this study will contribute to the quadruped robot works about walking and control.

REFERENCES

- [1] M. Raibert et al., Bigdog, "the rough-terrain quadruped robot", Proceedings of the 17th World Congress The International Federation of Automatic Control, pp. 10822-10825, Seoul, Korea, 2008.
- [2] M. Hutter et al., "Anymal-a highly mobile and dynamic quadrupedal robot", Intelligent Robots and Systems (IROS), 2016 IEEE/RSJ International Conference on. IEEE, 2016.
- [3] J. Cho et al., "Simple Walking Strategies for Hydraulically Driven Quadruped Robot over Uneven Terrain", Journal of Electrical Engineering & Technology, vol. 11, no. 5, pp. 1921-718, 2016.
- [4] C. Semini et al., "Design of the Hydraulically-Actuated Torque-Controlled Quadruped Robot HyQ2Max", IEEE/ASME Transactions on Mechatronics, vol. 22, no. 2, pp. 635-646, 2017.
- [5] K. R. Das, D. Das, and Das J., "Optimal tuning of PID controller using GWO algorithm for speed control in DC motor", Soft Computing Techniques and Implementations (ICSCIT), 2015 International Conference on. IEEE, 2015.
- [6] A. Madadi and M. M. Motlagh, "Optimal control of DC motor using grey wolf optimizer algorithm", TJEAS Journal-2014-4-04/373-379, vol. 4, no. 4, pp.373-79, 2014.
- [7] R. G. Kanojiya and P. M. Meshram, "Optimal tuning of PI controller for speed control of DC motor drive using particle swarm optimization", Advances in Power Conversion and Energy Technologies (APCET), 2012 International Conference on. IEEE, 2012.
- [8] P.B. de Moura Oliveira, H. Freire, and E.J. Solteiro Pires, "Grey wolf optimization for PID controller design with prescribed robustness margins", Soft Computing, vol.20, pp.4243-4255, 2016.
- [9] S.K. Verma, S. Yadav, and S.K. Nagar, "Optimization of Fractional Order PID Controller Using Grey Wolf Optimizer", Journal of Control Automation and Electrical Systems, vol. 28, pp. 314-322, 2017. <https://doi.org/10.1007/s40313-017-0305-3>
- [10] D. K. Lal, A. K. Barisal, and M. Tripathy, "Grey wolf optimizer algorithm based fuzzy PID controller for AGC of multi-area power system with TCPS", Procedia Computer Science, vol. 92, pp. 99-105, 2016.
- [11] P. W. Tsai, T. T. Nguyen, T. K. Dao, "Robot Path Planning Optimization Based on Multiobjective Grey Wolf Optimizer", In: Pan JS., Lin JW., Wang CH., Jiang X. (eds) Genetic and Evolutionary Computing. ICGEC

2016. Advances in Intelligent Systems and Computing, Springer, Cham, vol 536, pp.166-173, 2017.
- [12] N. Razmjoo, M. Ramezani, and A. Namadchian, "A New LQR Optimal Control for a Single-Link Flexible Joint Robot Manipulator Based on Grey Wolf Optimizer", Majlesi Journal of Electrical Engineering vol.10, no. 3, pp.53-60, 2016.
- [13] A. H. V. Hultmann, C. L. do Santos, "Tuning of PID Controller Based on a Multiobjective Genetic Algorithm Applied to a Robotic Manipulator", Expert Systems with Applications, vol. 39, pp. 8968-8974, 2012.
- [14] R. A. Krohling and J. P. Rey, "Design of optimal disturbance rejection PID controllers using genetic algorithms", IEEE Transactions on Evolutionary Computation, vol. 5, no. 1, pp. 78-82, 2001.
- [15] S. Mirjalili, S. M. Mirjalili, and A. Lewis, "Grey wolf optimizer", Advances in Engineering Software, vol. 69, pp. 46-6, 2014.
- [16] S. Mirjalili et al., "Multi-objective grey wolf optimizer: a novel algorithm for multi-criterion optimization", Expert Systems with Applications vol. 47, pp.106-119, 2016.
- [17] Mirjalili S., "How effective is the Grey Wolf optimizer in training multi-layer perceptrons, Applied Intelligence", vol. 43, no. 1, pp. 150-161, 2015.
- [18] S. Shahrzad, S. Z. Mirjalili, and S. M. Mirjalili, "Evolutionary population dynamics and grey wolf optimizer", Neural Computing and Applications vol. 26, no. 5, pp. 1257-1263, 2015.
- [19] X. Song, et al., "Grey Wolf Optimizer for parameter estimation in surface waves", Soil Dynamics and Earthquake Engineering vol. 75, pp. 147-157, 2015.
- [20] J. Kennedy, "Particle swarm optimization, Encyclopedia of machine learning", Springer US, pp.760-766, 2011.
- [21] M. Zarringhalami, S. M. Hakimi and M. Javadi, "Optimal Regulation of STATCOM Controllers and PSS Parameters Using Hybrid Particle Swarm Optimization", IEEE conference, 2010.
- [22] S. Panda, and N. Padhy, "Comparison of particle swarm optimization and Genetic Algorithm for FACTS-based controller design", International Journal of Applied Soft Computing, pp. 1418-1427, 2008.
- [23] S. S. Rao, "Engineering Optimization Theory and Practice", 4th Edition, John Wiley & Sons Inc. 2009.
- [24] MATLAB Global Optimization Toolbox User's Guide (Release 2015b), <http://www.mathworks.com/help/gads/index.html>

BIOGRAPHIES



MUHAMMED ARIF ŞEN was born in 1987, Konya, Turkey. He received the B.S. and M.S. degrees in Mechanical Engineering from Selçuk University, Konya, Turkey, in 2010, and 2014, respectively. He currently continues Ph.D. education at Selçuk University Faculty of Engineering, as a research assistant. His research interests include, Control Theory, System Dynamics, Mechatronics Systems, Mobile Robotics, Modelling and Simulation, MATLAB Simulation, Controller Design, The Bees Algorithm and Optimization.



METE KALYONCU received the M.S. and Ph.D. degrees in Mechanical Engineering from Selçuk University, Konya, Turkey, in 1993 and 1998, respectively. He is currently a full Professor in the Mechanical Engineering Department, Selçuk University. His research interests include, System Dynamics and Control, Mechatronics, Mechanical Vibration, Robotic, Industrial Design, Fuzzy Logic Control, Modelling of Systems and Simulation, Controller Design, The Bees Algorithm and Optimization.

Performance of MAP Channel Estimator in Power Line Communication with OFDM under Impulsive Noise

S. Muratoğlu Çürük

Abstract— Power Line Communication (PLC), which is a competitive technique especially for in-home applications, faces impulsive noise together with unstable channel characteristics. These two unpredictable factors make the communication on power lines difficult, which may reduce the efficiency of Orthogonal Frequency Division Multiplexing (OFDM), the selected modulation standard for PLC. There exists various channel estimators for PLC in the literature. The former techniques assume the channel noise is white Gaussian as in the wireless multipath, while the newer ones model the corrupted noise as impulsive which results with more complex receivers. In this study, the performance of the Maximum A-Posteriori (MAP) estimator proposed for additive white Gaussian noise channels is evaluated for PLC systems with OFDM under the constraint of impulsive noise. For the simulations multipath channel data is taken from the literature and Middleton Class A impulsive noise model is used. The results show that the MAP estimator which is designed with the assumption of white Gaussian noise has a satisfactory performance even under heavy impulsive noise.

Index Terms— Channel estimation, impulsive noise, Orthogonal Frequency Division Multiplexing, Power Line Communication.

I. INTRODUCTION

In recent years, studies related to the performance of the popular technique, Power Line Communication (PLC) is increasing rapidly. The main superiority of PLC is that it does not request any specific wiring for communication because it uses the already existing power line network. For communication, though they are wired, power line channels have multipath characteristics like the wireless channels and the parameters of the multipath channels vary with different network topologies and loads. Moreover, PLC may be damaged by disturbances, such as narrowband interference and additive, white/colored and/or impulsive noise. Unfortunately, all these factors result with unstable varying channel characteristics, which is the primary restricting factor for the data rate of PLC modems that has to struggle with alternatives.

S. M. ÇÜRÜK, is with Department of Electrical and Electronics Engineering University of Iskenderun Technical University, Hatay, Turkey, (e-mail: selva.curuk@iste.edu.tr) 

Manuscript received September 18, 2017; accepted January 9, 2018.
DOI: [10.17694/bajece.401998](https://doi.org/10.17694/bajece.401998)

For a success power line networks should be considered carefully and this increases the complexity of PLC systems. The multicarrier modulation technique named Orthogonal Frequency Division Multiplexing (OFDM) overcomes multipath fading effects by dividing the wide band into many narrower subbands where it uses orthogonal carriers for bandwidth efficiency. OFDM has been popular for wireless communication systems and has also been selected by Home Plug Powerline Alliance as power line modulation standard [1]. The performance of an OFDM system is highly dependent on the quality of the channel estimation. Typically, in OFDM systems subchannel coefficients are highly correlated. Thus the Maximum A-Posteriori (MAP) based estimation techniques are expected to perform better than the Maximum Likelihood (ML) based ones: The ML estimates will have a higher Mean Square Error (MSE) especially for low Signal to Noise Ratios (SNR).

Although the number is limited, channel estimators for OFDM systems in PLCs have been proposed in the literature. The former techniques assume the channel noise is white Gaussian as in the wireless multipath, while the newer ones are more realistic and model the corrupted noise as impulsive which results with more complex receiver structures. Further, adaptive estimator structures proposed, which estimate the channel and noise dynamically, are declared to have better performance but even more complicated receivers. For example in [2], to reduce impulsive noise, an algorithm for channel estimation is given basing on a robust cost function. In [3], a discrete-time parametric representation of a linear periodically time-varying system is adopted to model indoor power line channels. Following, the parameters of the proposed representation are estimated. In [4], the robust relevance vector machine based channel estimation is used. The authors in [5] present an adaptive iterative receiver used to decrease the impact of impulsive noise on OFDM based power line communications. In [6], power line channel impulse response estimation is done by applying a relevance vector machine to the received data. The authors of [7] cancel the impulsive noise in PLC systems with OFDM by steps settled on turbo coding and frequency domain equalization. The adaptive algorithm in [8] for impulsive noise suppression seen over the PLC channel applies an iterative estimation. In [9], regardless of the statistics of the noise, the authors give the equivalence of Minimum SNR estimator and Minimum MSE estimator. In [10], authors have used the Generalized Eigenvalues Utilizing Signal Subspace

Eigenvectors algorithm for multipath parameter estimation of PLC channel. The authors of [11] provide an iterative impulsive noise reduction technique based on MMSE/MAP estimation for OFDM communications.

Before dealing with complicated receivers, the question that should be answered is that, do we really need such complex receivers in practice? What is the degradation in performance if we use simple estimation techniques? Therefore, in this study, we investigate the degradation in performance if we use the MAP estimator proposed for additive white Gaussian noise channels for PLC systems with OFDM under the constraint of impulsive noise.

II. POWER LINE CHANNELS

PLC channels have frequency selective and time varying multipath behavior, depending on the network topology and wire type. The studies have shown that a PLC channel may be modeled as a multipath channel, and its frequency response is dedicated by [12]

$$H(f, t) = \sum_{i=1}^{L_p} g_{i,t} \cdot e^{-(a_0+a_1 f^k) d_i} \cdot e^{-j2\pi f(d_i/v_p)}, \quad (1)$$

where $g_{i,t}$ is the time dependent weighting factor of i -th path. $e^{-(a_0+a_1 f^k) d_i}$ is the attenuation part (a_0 and a_1 are attenuation parameters, k is the exponent of the attenuation factor, d_i is the length of i -th path) and $e^{-j2\pi f(d_i/v_p)}$ is the delay portion (v_p is the propagation velocity).

In this study, three different PLC multipath channel model taken from the literature are used: CH1, is a 4-path multipath channel which is suitable for PLC channels with 1-4 branch network topology and short distance in the range of 100 - 200 m [12]. The attenuation parameters are $a_0 = 0$, $a_1 = 7.8 \cdot 10^{-10}$, $k = 1$, and the propagation velocity $v_p = 1.5 \cdot 10^8$. CH2 is again for short distance channels with an 8-path multipath, but with different attenuation parameters: $a_0 = 0$, $a_1 = 1 \cdot 10^{-7}$, $k = 0.6$ [13]. CH3 has 15 path, and is a model for longer distance, longer than 300 m, with a more complicated network topology [14]. The parameters are $a_0 = 0$, $a_1 = 7.8 \cdot 10^{-10}$, $k = 1$, and $v_p = 1.5 \cdot 10^8$. The path weighting factor $g_{i,t}$ and path length d_i , for CH1, CH2 and CH3 are inscribed in Table 1, Table 2 and Table 3, respectively.

TABLE I
CHANNEL I (CH1) PARAMETERS

Path no	1	2	3	4
$g_{i,t}$	0.64	0.38	- 0.15	0.05
d_i (m)	200	222.4	244.8	267.5

TABLE II
CHANNEL II (CH2) PARAMETERS

Path no	1	2	3	4
$g_{i,t}$	0.6	0.11	- 0.12	0.11
d_i (m)	15	22	28	35
Path no	5	6	7	8
$g_{i,t}$	0.07	- 0.07	0.06	- 0.01
d_i (m)	41	48	53	59

TABLE III
CHANNEL III (CH3) PARAMETERS

Path no	1	2	3	4	5
$g_{i,t}$	0.029	0.043	0.103	-0.058	-0.045
d_i (m)	75	85	94.2	119.2	123.3
Path no	6	7	8	9	10
$g_{i,t}$	-0.040	0.038	-0.038	0.071	-0.035
d_i (m)	166.7	216.7	268.3	342.5	408.3
Path no	11	12	13	14	15
$g_{i,t}$	0.065	-0.055	0.042	-0.059	0.049
d_i (m)	472.5	616.7	800	941.7	1041.7

The noise sources observed in PLC channels may be grouped according to their durations. The first group is stationary over a long period compared to symbol duration and is called background noise. It is a combination of colored background noise, narrowband noise and periodic impulsive noise asynchronous to the mains frequency. The second group is time variant with short durations of microseconds to milliseconds. This group is a combination of asynchronous impulsive noise and periodic impulsive noise synchronous to the mains frequency. Time domain impulsive noise in PLC is modelled frequently with Middleton's Class A noise model. The probability density function (pdf) of a Middleton Class A noise sample n_k is given by [15]:

$$p(n_k) = \sum_{m=0}^{\infty} P_m \cdot \mathcal{N}(n_k; 0, \sigma_m^2), \quad (2)$$

where the mixing probability P_m is given by

$$P_m = \frac{A^m \cdot e^{-A}}{m!}. \quad (3)$$

The "impulsive index" A gives the density of impulses in an observation period. It should be specified that $A \in [10^{-2}, 1]$ for PLC channels. $\mathcal{N}(n_k; \mu, \sigma_m^2)$ is the Gaussian pdf with mean μ and variance σ_m^2 . The variance in Middleton Class A model is defined as

$$\sigma_m^2 = \sigma_I^2 \cdot \frac{m}{A} + \sigma_g^2 \quad (4)$$

or equivalently,

$$\sigma_m^2 = \sigma_g^2 \left(\frac{m}{A\Gamma} + 1 \right). \quad (5)$$

Here σ_l^2 and σ_g^2 are the variances of the impulse noise and the background Gaussian noise, respectively. The Gaussian factor $\Gamma = \sigma_g^2 / \sigma_l^2$ is the ratio of Gaussian to impulse noise power. The Gaussian factor is generally in the range $[10^{-6}, 1]$.

III. CHANNEL ESTIMATORS

The PLC channel is assumed to be stationary inside the observation interval. Further, the channel band is frequency selective, but flat for subbands of OFDM. Then, after removing the modulation effects, the received vector for an OFDM system with N subcarriers is:

$$\mathbf{r} = \mathbf{h} + \mathbf{n}, \quad (6)$$

where the additive noise \mathbf{n} is impulsive and the channel coefficients \mathbf{h} are samples of zero mean jointly Gaussian complex random process with covariance matrix \mathbf{C}_h . The MAP estimation of the channel coefficient vector [16] is found by:

$$\hat{\mathbf{h}}_{\text{MAP}} = \arg \max_{\mathbf{z}} p(\mathbf{h}/\mathbf{r}) \quad (7)$$

If the impulsive noise is modeled as zero mean white Gaussian with covariance matrix \mathbf{C}_n , then

$$p(\mathbf{r}/\mathbf{h}) = \frac{1}{\pi^N |\mathbf{C}_n|} \exp \left[-(\mathbf{r} - \mathbf{h})^H \mathbf{C}_n^{-1} (\mathbf{r} - \mathbf{h}) \right] \quad (8)$$

$$p(\mathbf{h}) = \frac{1}{\pi^N |\mathbf{C}_h|} \exp \left[-\mathbf{h}^H \mathbf{C}_h^{-1} \mathbf{h} \right] \quad (9)$$

Following necessary steps it can be shown that the MAP estimates are given by:

$$\hat{\mathbf{h}}_{\text{MAP}} = (\mathbf{C}_n^{-1} + \mathbf{C}_h^{-1})^{-1} \mathbf{C}_n^{-1} \mathbf{r} \quad (10)$$

and simplifying (10), MAP estimation expression is found to be

$$\hat{\mathbf{h}}_{\text{MAP}} = \mathbf{B} \cdot \mathbf{r} \quad \text{where} \quad \mathbf{B} = \mathbf{C}_h \cdot (\mathbf{C}_n + \mathbf{C}_h)^{-1} \quad (11)$$

The MSE matrix for the MAP estimates is given by [16]:

$$\mathbf{MSE}_{\text{MAP}} = \mathbf{B} \cdot \mathbf{C}_n \cdot \mathbf{B}^H + (\mathbf{B} - \mathbf{I}_N) \cdot \mathbf{C}_h \cdot (\mathbf{B} - \mathbf{I}_N)^H \quad (12)$$

where \mathbf{I}_N is the $N \times N$ identity matrix and $(\cdot)^H$ means Hermitian of the matrix. Equivalently, it can be written as

$$\mathbf{MSE}_{\text{MAP}} = \mathbf{C}_h - \mathbf{C}_h \cdot (\mathbf{C}_n + \mathbf{C}_h)^{-1} \cdot \mathbf{C}_h \quad (13)$$

Note that, under the constraint of white noise, the noise samples are mutually independent, i.e., $\mathbf{C}_n = \sigma_n^2 \mathbf{I}_N$, where σ_n^2 is white noise variance, then (13) simplifies to

$$\mathbf{MSE}_{\text{MAP}} = \sigma_n^2 \cdot \mathbf{B} \quad (14)$$

For ML estimation (without a priori knowledge of the channel), \mathbf{B} will be the identity matrix. Then the ML estimate [16] is $\hat{\mathbf{h}}_{\text{ML}} = \mathbf{r}$, and its MSE is $\mathbf{MSE}_{\text{ML}} = \mathbf{C}_n$.

IV. SIMULATION RESULTS

For the simulations, we have taken the HomePlug AV standard [1] as reference. The standard states that OFDM with 1155 subcarrier is used as modulation scheme in the band 1.8 to 30 MHz. Therefore in the simulations 0-30 MHz band is considered (elementary period T is $1/30 \mu\text{s}$) and the subcarrier number, N , is selected to be 1200 (25 kHz subbands).

Fig. 1, Fig. 2 and Fig. 3 depict multipath characteristics of PLC channels that will be estimated, whose parameters are given in Section II. The amplitudes are determined from the samples taken from the amplitude spectra of the channels where n is the subchannel indices. As seen from the figures the frequency selectivity is lowest for CH2. The amplitude attenuation that exists in CH1 rapidly increases with frequency. And for CH3, there are sudden changes in the multipath characteristics in 0-200 subbands (0-5 MHz band), which is more serious in 0-100 subbands (0-2.5 MHz band).

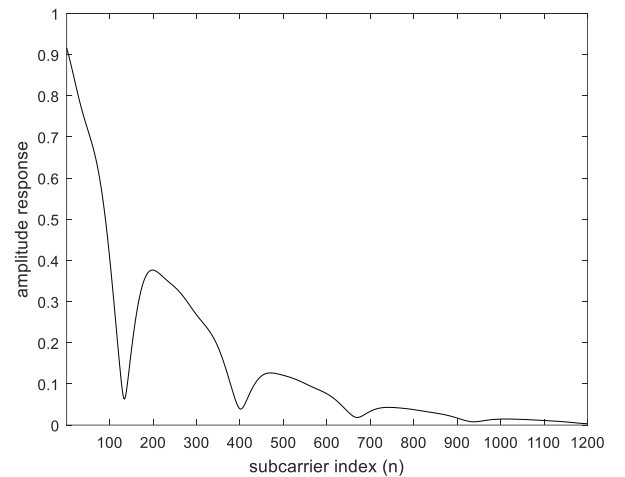


Fig. 1. Amplitude response of CH1 versus subcarrier index.

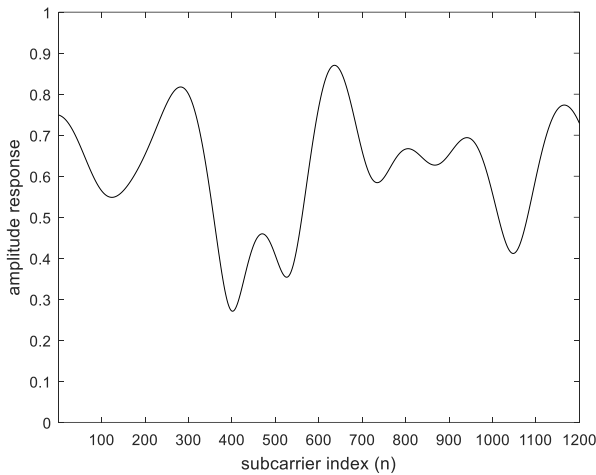


Fig. 2. Amplitude response of CH2 versus subcarrier index

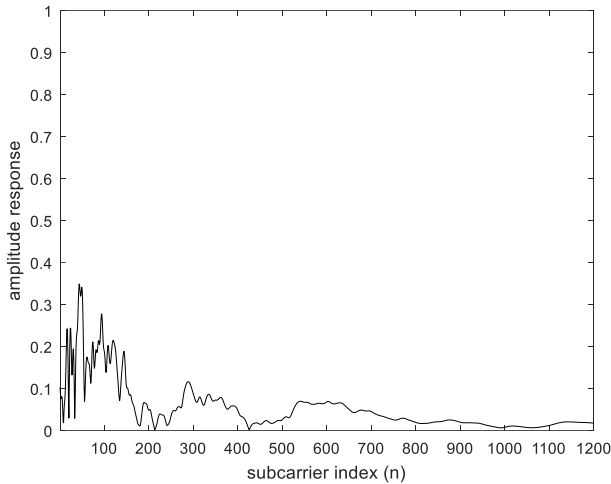


Fig. 3. Amplitude response of CH3 versus subcarrier index.

Simulation results of MAP channel estimator rms errors with Gaussian noise versus subchannel number for CH1, CH2 and CH3 are given in Fig. 4, Fig. 5, and Fig. 6, respectively. Simulation parameters are selected to be SNR = 10 dB, $N = 1200$. The performance of the MAP estimator with Gaussian noise assumption is also analyzed under the Middleton Class A model impulsive noise with parameter values are selected to be $A = 1$, $\Gamma = 10^{-6}$ (highly impulsive case) with same SNR and subcarrier number as in the previous simulations. Simulation results for CH1, CH2 and CH3 are again given in Fig. 4, Fig. 5, and Fig. 6, respectively. As seen, the performance of the MAP estimator designed for Gaussian noise is good under the constraint of impulsive noise for all channels, as in white noise case. The average MSEs under Gaussian noise are 0.0022, 0.0024 and 0.0003 for CH1, CH2 and CH3, respectively. Under the impulsive noise, the averages are 0.0024, 0.0028 and 0.0003 for CH1, CH2 and CH3, respectively. MAP estimator designed with the assumption of Gaussian noise performs well in all channels even in the worst case of impulsive noise when SNR is 10 dB.

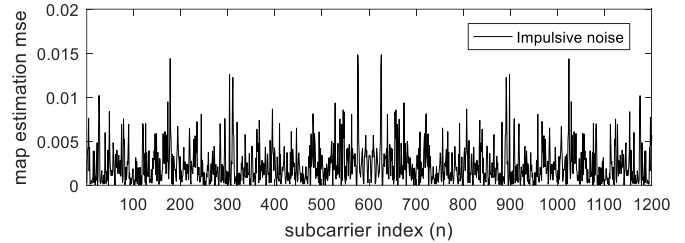
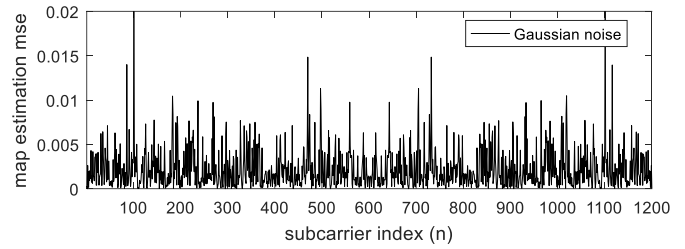


Fig. 4. MAP channel estimator rms error, SNR = 10 dB, CH1, Gaussian and Impulsive noise.

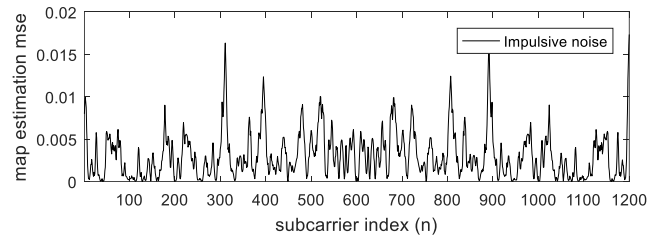
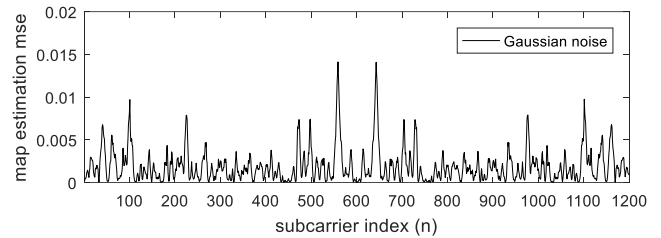


Fig. 5. MAP channel estimator rms error, SNR = 10 dB, CH2, Gaussian and Impulsive noise.

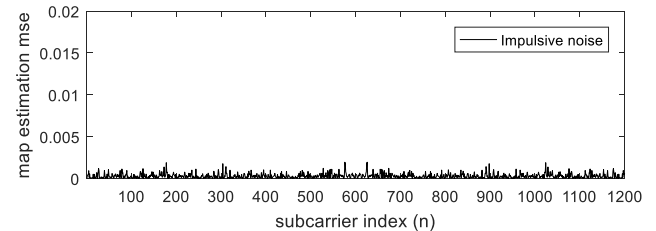
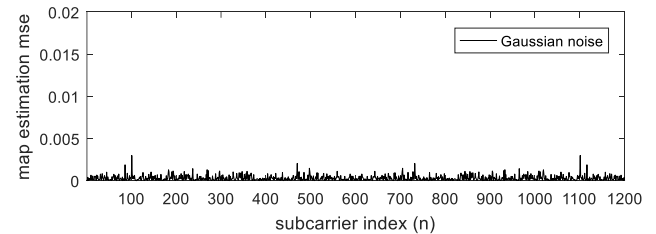


Fig. 6. MAP channel estimator rms error, SNR = 10 dB, CH3, Gaussian and Impulsive noise.

The simulations are repeated for $\text{SNR} = 0$ dB to investigate the performance for low SNR case. The results are given below in Fig. 7, Fig. 8 and Fig. 9. The average MSEs of estimator under Gaussian noise are found to be 0.0059, 0.0092 and 0.0012 for CH1, CH2 and CH3, respectively. The average MSEs of estimator under impulsive noise are 0.0064, 0.0106 and 0.0014 for CH1, CH2 and CH3, respectively. Again we concluded that although there is a slight degradation in performance, the MAP estimator designed with the assumption of Gaussian noise performs well in all channels.

The simulation results showed that all performances are very close to the case of channel with Gaussian noise even in the worst case of impulsive noise and low SNR. This is because of the FFT operation in OFDM receiver. OFDM systems randomized the power line impulsive noise via its FFT operation, resulting in Gaussian distributed noise, especially if the number of OFDM subcarriers is sufficiently large.

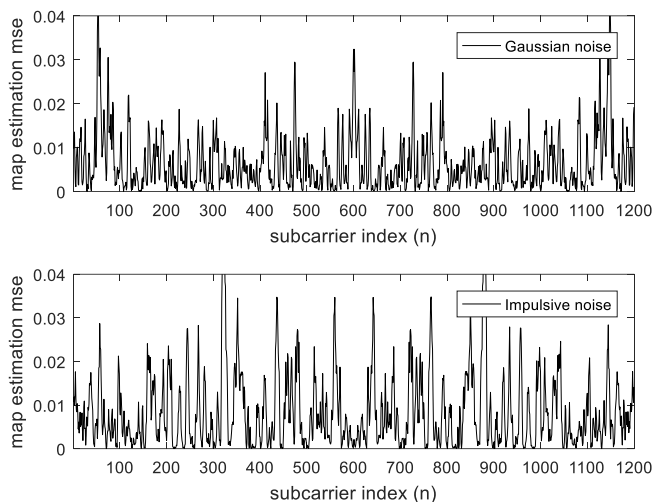


Fig. 7. MAP channel estimator rms error, $\text{SNR} = 0$ dB, CH1, Gaussian and Impulsive noise.

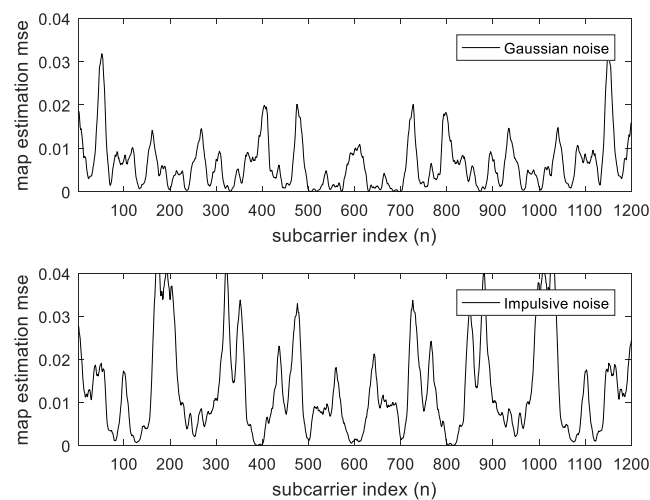


Fig. 8. MAP channel estimator rms error, $\text{SNR} = 0$ dB, CH2, Gaussian and Impulsive noise.

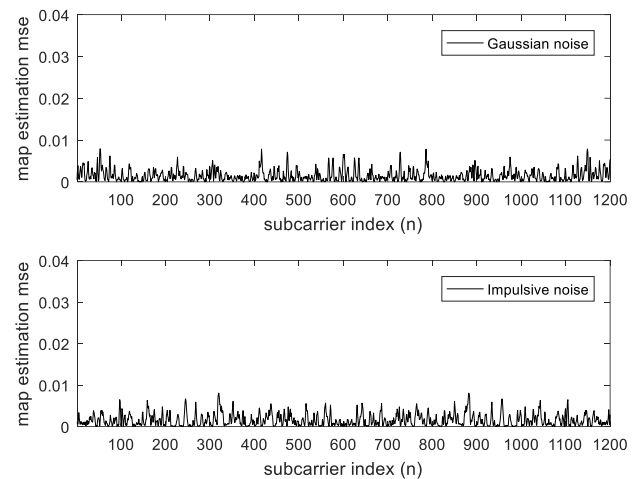


Fig. 9. MAP channel estimator rms error, $\text{SNR} = 0$ dB, CH3, Gaussian and Impulsive noise.

V. CONCLUSION

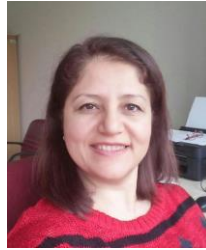
In this study, we aimed to analyze the degradation in the performance of MAP channel estimator if we ignore the noise is impulsive and assume it Gaussian. Thus, the performance of MAP channel estimator proposed for additive white Gaussian noise channels is evaluated for PLC systems with OFDM under the constraint of impulsive noise. The simulations are done using three different channel data taken from the literature and Middleton Class A impulsive noise model. The MSE of estimations under heavy impulsive noise circumstance is investigated. The results show that the degradation in performance is insignificant, only distinctive for low SNR, for all channels. The MAP estimator which is designed for white Gaussian noise has a quite satisfactory performance even under heavy impulsive noise and can be safely used. The reason is that in an OFDM system, the impulsive noise is randomized via the FFT operation, thus noise is spread over all carrier frequencies and behaves like Gaussian even if it is impulsive in time domain. We conclude that we can safely assume the noise to be Gaussian in frequency domain

REFERENCES

- [1] HomePlug Powerline Alliance Inc. (2005). "HomePlug AV White Paper", Available: http://www.homeplug.org/media/filer_public/b8/68/b86828d9-7e8a-486f-aa82-179e6e95cab5/hpav-white-paper_050818.pdf, date on 17.05.2017.
- [2] J. Huang, P. Wang, Q. Wan, "Robust approach for channel estimation in power line communication", *Journal of Communications and Networks*, Vol.14, No.3, 2012, pp.237–242.
- [3] F. Gianaroli, F. Pancaldi, G.M. Vitetta, "On the use of Zadeh's series expansion for modeling and estimation of indoor powerline channels", *IEEE Transactions on Communications*, Vol.62, No.7, 2014, pp.2558–2568.
- [4] M. Asadpour, F.A. Ajhiri, B.M. Tazehkand, et al., "Jointly RVM based channel estimation and PAPR reduction using Modified Tabu Search Algorithm in Power Line Communication systems", *Wireless Personal Communications*, Vol.84, No.4, 2015, pp.2757–2775.
- [5] Y.R. Chien, "Iterative channel estimation and impulsive noise mitigation algorithm for OFDM-based receivers with application to Power-line communications", *IEEE Transactions on Power Delivery*, Vol.30, No.6, 2015, pp.2435–2442.

- [6] M. Asadpour, B.M. Tazehkand, H. Seyedarabi, "A robust Bayesian inference-based channel estimation in power line communication systems contaminated by impulsive noise", *Turkish Journal of Electrical Engineering and Computer Sciences*, Vol.24, No.4, 2016, pp.2865-2880.
- [7] Y. Himeur, A. Boukabou, A. Senouci, "Performance of turbo-coded chaotic interleaving and frequency-domain equalization scheme for high speed OFDM-based PLC systems", *Journal of the Franklin Institute*, Vol.353, No.15, 2016, pp.3799-3817.
- [8] Y. Himeur, A. Boukabou, "OFDM-based power-line communication enhancement using a turbo coded adaptive impulsive noise compensator", *Telecommunication Systems*, Vol.62, No.3, 2016, pp.481-494.
- [9] L. Rugini, P. Banelli, "On the equivalence of Maximum SNR and MMSE estimation: Applications to additive non-gaussian channels and quantized observations", *IEEE Transactions on Signal Processing*, Vol.64, No.23, 2016, pp. 6190-6199.
- [10] Y.H. Kim, "Multipath parameter estimation for PLC channels using the GEESE algorithm", *IEEE Transactions on Power Delivery*, Vol.25, No.4, 2010, pp. 2339-2345.
- [11] P.A.C. Lopes, J.A.B. Gerald, "Iterative MMSE/MAP impulsive noise reduction for OFDM", *Digital Signal Processing*, Vol.69, 2017, pp.252-258.
- [12] M. Zimmermann, K. Dostert, "A multipath model for the powerline channel", *IEEE Transactions on Communication*, Vol.50, No.4, 2002, pp.553-559.
- [13] X. Ding, J. Meng, B.R. Petersen, "Blind channel estimation for HomePlug power-line communications: A feasibility?", *IEEE Transactions on Power Delivery*, Vol.26, No.2, 2011, pp. 754-763.
- [14] A.A.M. Picorone, L.R. Amado, M.V. Ribeiro, "Linear and periodically time-varying PLC channels estimation in the presence of impulsive noise", *IEEE International Symposium on Power Line Communications and Its Applications*, 2010, pp.255-260.
- [15] T. Shongwe, A.J.H. Vinck, H.C. Ferreira, "A study on impulse noise and its models", *SAIEE Africa Research Journal*, Vol.106, No.3, 2015, pp.119-131.
- [16] S.M. Curuk, Y. Tanik, "A simplified MAP channel estimator for OFDM systems under Rayleigh fading", *European Transactions on Telecommunications*, Vol.21, No.4, 2010, pp.396-405.

BIOGRAPHIES



SELVA MURATOĞLU ÇÜRÜK received the B.S. degree from the Electrical and Electronics Engineering Department, Middle East Technical University (METU), Ankara, Turkey, in 1996, and the M.S. and Ph.D. degrees from the same university, in 1999 and 2008, respectively. She is currently an Assistant Professor at the Iskenderun Technical University.

Her research interests are wireless communication systems, digital communication theory, digital signal processing, multicarrier modulation and channel modeling.

Researches on Anti-reflection Coating (ARC) Methods Used in PV Systems

N. Ekren

Abstract—With the development of PV systems' technology over the years and the reduction of production costs, PV systems are now being used for electricity generation. PV systems are listed among the renewable energy sources as the only requirement is solar energy and electricity generation is carried out without any fuel and waste. Solar cells used in PV systems are adversely affected by extremes of temperature, shading, reflection, and pollution. It is known that before sunrays reach the cell's surface, some of them disappears from the protective glass surface and are reflected back from the cell through the glass surface. Anti-reflection coatings (ARC) are used to reduce the energy loss and increase solar cell efficiency and output power. SiO_2 and MgF_2 are the most commonly used solutions among these coatings. It has been seen that the most efficient applications, with anti-reflection coatings as single, double, triple and more layers, are in triple layers applications. It has been observed that applications to the protective glass surface have self-cleaning properties, and TiO_2 and ZrO_2 are frequently used for this. The reflectance index of the protective glass, which is normally 1.51, can be reduced to 1.20 in silicone cells and 1.28 in thin film surfaces with the AR coatings.

Index Terms—PV systems, Anti-reflection, Anti-reflective Coating, Reflection index.

I. INTRODUCTION

IN RECENT YEARS, the share of fossil-fuelled energy sources in electricity generation has been reduced, so renewable energy sources now have more share. When fossil-fuelled resources are used for electricity generation, they release hazardous wastes to the environment. Recently, some studies have been carried out on the environmental pollution caused by these wastes, whose effects lead directly or indirectly to major problems [1]. The use of renewable energy does not generate any waste, so this is a key advantage for nature and human health. Including solar, wind, hydro and biofuel as sources, the use of renewable energy sources as an alternative to fossil fuel usage has gained momentum worldwide. One of the most important renewable energy sources is solar energy. The most common method is the production of electricity by photovoltaic panels, although methods such as solar chimney, condensed solar energy used in electricity generation from solar energy are used. Until 2030, the electricity demand in the world is predicted to increase by 76%.

N. EKREN, is with Department of Electrical and Electronics Eng., Marmara University, Istanbul, Turkey, (e-mail: nazmiyekren@marmara.edu.tr) 

Manuscript received September 18, 2017; accepted January 9, 2018.
DOI: [10.17694/bajece.402004](https://doi.org/10.17694/bajece.402004)

The energy of 5100J per hour that reaches the earth from the sun is the amount of energy consumed by all people in a year. It is known that in photovoltaic systems, 30% of the solar energy is reflected back from the panel surface, and about 70% of the solar energy reaches the solar cell [2]. In this context, solar energy is benefited by the conversion of the energy it contains with the photovoltaic systems to electricity.

Looking at the types of solar panels used in photovoltaic systems, monocrystalline (SC-Si) and polycrystalline (MC-Si) panels appear to be at the forefront. In 2014, 92% of total production was achieved with monocrystalline and polycrystalline panels [3]. The percentage of thin film surfaces (CdTe , CuSe_2 (CIGS)) is less than that of silicon-based surfaces [4]. On the other hand, the production cost of thin films is lower than that of Silicon cells, and thus the production of thin films has accelerated in recent years [5]. The production cost in the silicon panels was 8.5 USD / w in 1995 and 1.1 USD / w in 2015 [6]. Despite the decrease in production costs, the photovoltaic systems which are more expensive and have newer technologies than other electricity generation methods have a share of 1.5% in world electricity generation in 2016. The share of fossil-fuelled resources is 75.5%, which indicates that PV systems are very backward in the same year [7].

II. PV TECHNOLOGY

The applications to utilize solar energy, both in heating and in electricity generation, have been date back to 1960s. The structure of a solar panel consists of a solar cell and protective outer glass. Solar cells vary in their physical and chemical form with the yield, based on the nature of the material, such as silicon (Si) or gallium-arsenide (GaAs). An air gap is the necessity of the distance between the solar cell and the protective glass to zero. The sun's rays entering the air gap will scatter and break, as well as they will cause oxidations in the connections of the cells. For these reasons, there should be no air gap. The protective exterior glass structure is made to be straight and as thin as possible, but it is manufactured resistant to physical factors. In addition to making the protective glass straight, there are also solar panels manufactured by the Fresnel eye method [8].

The efficiency of solar panels is decreased by the effect of temperature increase or overheating, due to solar radiation scattered or reflected by the dirt on the surface, and atmospheric phenomena such as low solar radiation and cloudiness [9]. The real danger for solar panels is reduced efficiency due to overheating. Therefore, cooling technologies are being developed. Up to 20% efficiency increase was observed in the oil cooling operation [10].

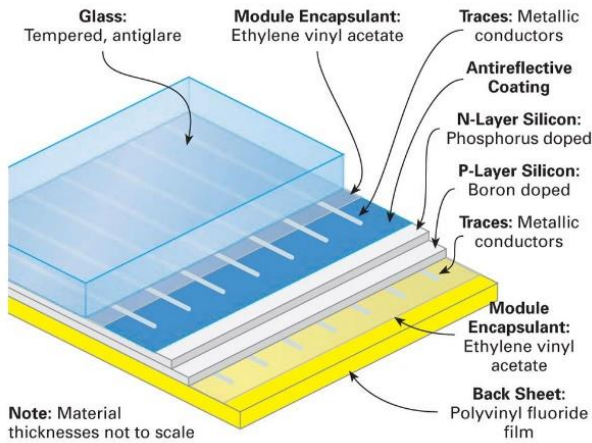


Fig.1. Layers of Solar Cell

Recent studies to increase the efficiency of solar panels have concentrated on Anti-reflective Coating (ARC). The purpose of this study is to analyse the studies in this area and to examine these coating studies according to different cell types and application methods.

To investigate anti-reflection coatings, it is first necessary to classify solar panels according to cell types. Solar cells are made of Silicon Crystal based or Thin Film technology.

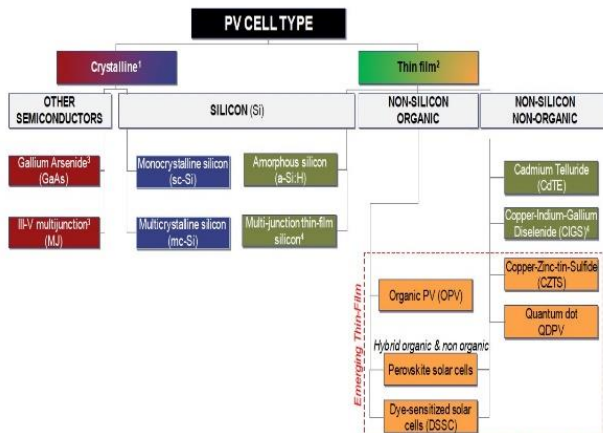


Fig.2. Classifying of PV Cells [11]

III. RESEARCH AND METHOD

Considering the studies of increasing the efficiency of solar panels, coating methods are applied according to cell types. Anti-reflection (AR) is defined as preventing reflection or refraction of sunlight coming to the cell surface. Anti-reflection applications technics are;

- Physical vapour deposition
- Chemical vapour deposition
- Thermal spraying
- Electro deposition
- Electro-less deposition
- Diffusion coating
- Laser based [12].

When the general properties used in these methods are examined, it is seen that the permeability of the coatings is less than 2.5 μm. In seasonal conditions, such as rain or snow, the

physical properties of the coatings are expected to remain unchanged and must be resistant to corrosion and oxidation [2]. Another common feature of anti-reflective coatings is that they can remain stable over long periods of temperature changes and various seasonal weather conditions. Another expectation with this seasonal change is that the surface is well adhered. The resistance against seasonal conditions is on the foreground in the coatings made on the glass surface.

The protective glass reflectance index used for solar panels is 1.51, the silicon cells are 4.71 and the air is 1.0 [13]. Anti-reflection coatings are expected to bring the reflectance index on the glass surface to zero. Because of the mechanical properties of the thin film surfaces, the solar panels used for the silicon cells achieved more efficient results [14]. In studies to reduce the reflectance index, it has been found that SiO₂ is coated with a lower index as a substrate and a different mixture. Implementing double layer coating (DLARC) on the coatings on the cell gave better mechanical and electrical results than single layer coating (SLARC). However, multi-layered coatings (MLARC) made from thinner layers than single- and double-layer coatings also showed favourable results from single- and double-layer coatings.

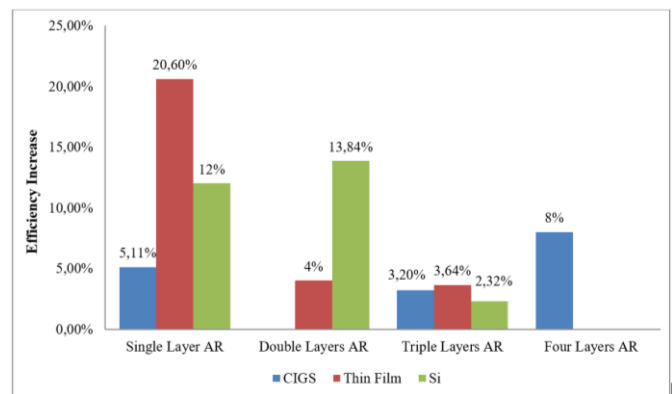


Fig.3. Effect of Anti-reflection Coating to Efficiency

When the literature studies are investigated, the anti-reflection coating works are concentrated on single, double and triple layer coatings. In case of working with four or more floors, the light transmittance decreased due to the increase of coating thickness, which led to decrease in efficiency and open circuit voltage. Silicon cells used as working surfaces have been studied with other thin film cell types, especially CIGS Thin film solar cells.

In the column of single-layer studies, an efficiency increase of 5.11% was obtained in CIGS cells. GIGS cell efficiency which is normally %16.7 increased to 17.6% with a single layer coating. MgF₂ was used at a thickness of about 120 nm [15]. In the case of investigating other thin film types, the efficiency was increased from 1.31% to 1.65% after coating and a total increase of 20.60% was obtained. ZnO cell coating of 80 nm thickness was performed [16]. A single layer of Ag + SiO₂ coating was applied to the silicon cells and a 12% efficiency gain was achieved by supporting this coating with a lens for light condensation [17].

In the two-layer anti-reflection applications; SiO₂ and nano TiO₂ applied to the silicon cell surface and was obtained 400 nm thickness coating. With these coatings, a maximum

efficiency increase of 16% was achieved while an average increase of 13.84% was achieved [18]. In another study on thin-film cells, the SiO₂ mixture was applied and the efficiency of the thin-film surface, which is 9.83%, was increased to 10.24%. The thickness of this two-layer application was around 90 nm [19].

Si-HC is coated on CIGS thin-film cell as a triple-layers antireflective coating. A thickness of 120 nm was obtained and an efficiency increase of 3.2% was obtained [20]. With SiO₂ coating on ZnO thin film, the thickness was 300 nm, and the triple layers coating efficiency increased by 3.64% [21]. In the triple-layers coating applied on the silicon cell surface, the protective glass was removed and TiAl₂ mixture solvent was used. This solvent was applied to the cell surface in triple layers and after each layer was dried the next layers were applied. With this mixture, 2.32% efficiency increase was obtained in silicon cells. The open circuit voltage was increased from 9.49 volts to 10.31 after coating [2].

The CIGS surface was used in four-layer coatings. This is why MgF₂ used does not decrease the required reflectivity when a single-layer coating is applied and does not increase the efficiency. For this reason, HfO₂, TiO₂ and ZrO₂ were used in the bottom and 2nd and 3rd layers respectively, and 2μm MgF₂ was used as the anti-reflection layer in the outermost layer. Optical losses decreased from 9% to 4%, while CIGS cell efficiency increased by 8% [22].

In addition to these coatings, a mold was placed on the protective glass surface to serve as a lens, after which SiO₂ was applied on the mold, and an efficiency increase of 7.88% was achieved with this combination [23].

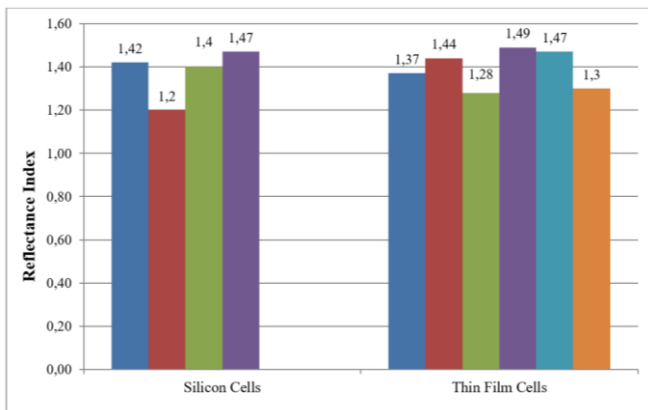


Fig.4. Effect of Anti-reflection Coating to Reflectance Index

It is aimed to pass the sunrays from the surface to the solar cell without any loss by the anti-reflection coatings. These studies are applied on the cell surface, protective glass surface and both cell surface and protective glass. In anti-reflection workings, it is usually seen to be applied to the protective glass surface and between the cell and the glass surface.

Coatings applied on silicone cells were investigated; a triple-layer SiO₂ coating was applied on a polycrystalline solar cell with an index gain of 5.9% and reduced to 1.42. In a study on a monocrystalline surface, a reflectance index of 1.19-1.21 was obtained [24]. In the study on radiation-hardened high-efficiency silicon cells (RHES), single-layer tested with the SiO₂ mixture resulted in 1.46, and 1.4 reflectance index when

triple-layers were applied [25]. In another study, the application of nano-ZnO on the protective glass of silicon cells was modelled. The thickness of the nano-ZnO coating modelled by the finite element method is considered to be 400 nm. The loss of 4% within this coating between the air and glass was estimated to be reduced to 1.5% and the reflection index to be 1.47 [26].

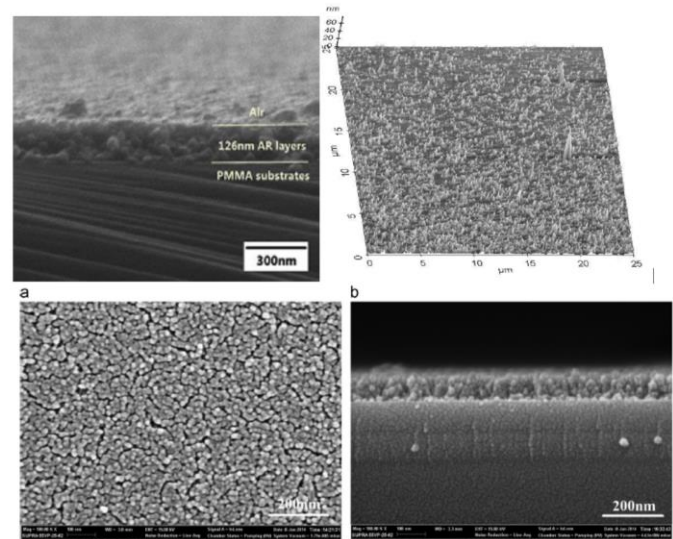


Figure 5. Electron microscopy images of anti-reflection coating studies [12, 19 27]

When working on the thin film; a self-cleaning feature was applied to the protective glass. TiO₂ and SiO₂ are used for the self-cleaning. The TiO₂ solution prepared was mixed with SiO₂ and coated with the spin coating method. With only TiO₂ applying, the reflection index of 2.71 was reduced to 1.37 by using 15% SiO₂ mixed [28]. In a study on the protective outer layer of the CdTe thin film solar cell, a multi-layer coating method was preferred. To reduce the loss due to the 4.2% reflection on the thin film glass, ZrO₂ with high reflectance index was first applied and SiO₂ with low reflectance index was applied above this ZrO₂ layer. A four-layer coating was obtained. The deposition was carried out by evaporation after the layers were made. Reflection losses were reduced to 1.36% and an index of 1.44 was obtained. However, in this application, the flexibility of the properties of the thin films led to the deterioration of this coating. When the thin films were flexed, it was observed that the coating deteriorated [29]. In another study where the SiO₂ coating was applied on BZO (Boron-doped Zinc Oxide) thin film surface, the light transmittance of about 92% was increased to 95%. Using the sol-gel dip coating method, a thickness of 90 nm could be obtained and this coating which is a reflectance index of 1.28 was found to be resistant to adverse weather conditions [19].

In another application, firstly, ZrO₂ was applied to the glass on the thin film surface and then secondly SiO₂, thirdly ZrO₂ again, and SiO₂ as the last layer. In this work, ZrO₂ has high index and low index SiO₂. In this way, a total thickness of 277 nm was obtained and the reflectance index decreased by 1.22% to 1.49. In the same study, 335 nm thicknesses were obtained with six-layer (3 ZrO₂ + 3 SiO₂) AR coating obtained using the same method and the reflectance decreased by 1.49%. The reflectance index of the six-layer application was 1.47 [30]. In

the study on the CIGS (CuInGaSe₂) thin film, the SiO₂ and WO₃ photocatalyst which has the self-cleaning Anti-reflective coating was applied. Due to the use of tungsten, the color of the surface coating is blackened and the reflectance index is measured as 1.3 [20].

IV. CONCLUSION

Because of the refraction and reflections from the surface when the sunrays meet the surface of the solar cell, there is a loss of efficiency even if the cell is positioned at the right angle. The solar cells meet with more solar rays and it is desired to increase the open circuit voltages and the energy intensities to obtain more power output. It is desired that to increase the open circuit voltages and the energy intensities to obtain more power output by meeting the solar cells with more solar rays.

Many methods and materials have been observed when investigating anti-reflection (AR) studies. In these studies, it was observed that the anti-reflective coatings (ARC) could be applied to the protective glass surface, to behind the glass and directly applied to the cell surface. The coating on the protective glass is very useful because they can be applied to existing PV energy systems and PV power plants without any change. It has also been shown that all of the work used in this method has been supplemented with self-cleaning materials and anti-reflection materials. With this combination, PV power plants will be able to achieve huge efficiency gains.

It has been observed that triple-layers of coatings are more durable and stable than the other multi-layers and also give results that are suitable for each type of solar cell. SiO₂, MgF₂ and TiO₂ were used in the coatings. While SiO₂ can be used as an anti-reflection coating alone, higher efficiency is obtained when it is supported by high reflection index materials such as ZrO₂. ZrO₂ was used as an alternative to TiO₂. As an alternative to TiO₂, ZrO₂, HfO₂, Ta₂O₅ and Nb₂O₅ are proposed.

It was observed with the difficulty of 4 or more layers of coatings and the adverse effect of increased thickness and the coatings were pulled away from the thin film surface during the test phase.

If an anti-reflective coating with self-cleaning properties is not used, anti-reflective coatings with a low reflectance index between the protective glass and the cell surface will provide solar cells with longer duration of use and efficiency.

V. REFERENCES

- [1] C.D. Evans, D.T. Monteith, D.M Cooper, "Long-term increases in surface water dissolved organic carbon: observations, possible causes and environmental impacts", *Environmental Pollution*, vol. 137, pp. 55-71, 2005.
- [2] B. Kumaragurubaran, S. Anandhi, "Reduction of reflection losses in solar cell using anti reflective coating", 2014 International conference on computation of power, energy, information and communication ICCPEIC, 2014.
- [3] Fraunhofer Institute of Solar Energy Systems, 2015.
- [4] Dimmler and Wachter, 2007.
- [5] White paper for CIGS thin film solar cell technology, 2016.
- [6] K. Branker, MJM Pathak, JM Pearce, "A review of solar photovoltaic levelized cost of electricity", *Renew. Sustain. Energy*, vol. 15, pp. 4470-4482, rev 2011.
- [7] M. Eckhart, M. El-Ashry, D. Hales, K. Hamilton, P. Rae, "Renewables 2017 Global Status Report", p. 33, 2017.
- [8] D. Huh, J. Shin, M. Byun, S. Son, P. Jung, H. Choi, Y. Kim, H. Lee, "Analysis of long-term monitoring data of PV module with SiO_x-based anti-reflective patterned protective glass", *Solar energy materials and solar cells*, vol. 170, pp. 33-38, 2017.
- [9] K.A Moharram, M.S, Abd-Elhady, Ha Kandil, H. el-Sherif, "Influence of cleaning using water and surfactants on the performance of photovoltaic panels", *Energy Convers Manage*, vol. 68, pp. 266-272, 2013.
- [10] M.S. Abd- Elhady, M.M. Fouad, T. Khalil, Improving the efficiency of photovoltaic (PV) panels by oil coating, *Energy conversion and management*, vol. 115, pp. 1-7, 2016.
- [11] A.T. Kearney Energy Transition Institute, IPCC 2011, Special Report on Renewable Energy, MIT 2015, The Future of Solar Energy
- [12] L.A. Dobrzanski, M. Szindler, Sol gel TiO₂ antireflection coating for silicon solar cells, *Journal of achievements in materials and manufacturing engineering (JAMME)*, Vol. 52-1, 2012
- [13] S. Yoon, G. Turner, V. Garboushian, Thin, lightweight, %18 efficient space silicon solar cell and array, 25th PVSC, May 1996, Washington USA.
- [14] X. Zhang, S. Cai, D. You, L. Yan, H. Lv, X. Yuan, B. Jiang, Template-free sol-gel preparation of superhydrophobic ORMOSIL films for double-Wavelength broadband antireflective coating, *Adv. Funct. Mater.*, vol. 23, no. 25, pp. 4361-4365, 2013.
- [15] G. Rajan, K. Aryal, T. Ashrafee, S. Karki, S. Babcock, V. Ranjan, Real-time Optimization of Anti-reflective Coating for CIGS Solar Cells, *Photovoltaic Specialists Conference (PVSC)*, 2016 IEEE 43rd, 2250-2253
- [16] M.Z. Pakhuruddin, Y.Yusof, K.Ibrahim, A.A. Aziz, Fabrication and characterization of zinc oxide anti-reflective coating on flexible thin film microcrystalline silicon solar cell, *Optik*, vol. 124, pp. 5397-5400, 2013.
- [17] F.Crisostomo, N.Hjerrild, S. Mesgari, Q. Li, R.A.Taylor, A hybrid PV/T collector using spectrally selective absorbing nanofluids, *Applied Energy*, vol. 193, pp. 1-14, 2017.
- [18] U.G. Yasa, M.N. Erim, N. Erim, M.O. Girgin, H. Kurt, "Design of anti-reflective graded height nanogratings for photovoltaic applications", *NUSOD* 2017.
- [19] N. Wang, J. Fang, X. Zhang, G. Wang, L. Wang, C. Liu, H. Zhao, Z. Chen, X.L. Chen, J. Sun, Y. Zhao, "Combined SiO₂ antireflective coating with MOCVD-ZnO:B to improve light absorption in thin-film solar cells", *Solar Energy Materials & Solar Cells*, vol. 130, pp. 420-425, 2014.
- [20] Y. Ota, N. Ahmad, K. Nishioka, "A 3.2% output increase in an existing photovoltaic system using an anti-reflection and anti-soiling silica-based coat", *Solar Energy*, vol.136, pp. 547-552, 2016.
- [21] Y. Lu, X. Zhang, J. Huang, J. Li, T. Wei, P. Lan, Y. Yang, H. Xu, W. Song, "Investigation on antireflection coating for Al:ZnO in silicon thin-film solar cells", *Optik*, vol. 124, pp. 3392-3395, 2013.
- [22] G. Rajan, T.Begou, K.Aryal, T.Ashrafee, S.Karki, V.Ranjan, A.A. Rockett, N.J. Podraza, R.W. Collins, S. Marsillac, "Optimization of multi-layered anti-reflective coating for ultra-thin Cu(In,Ga)Se₂ Solar Cells", *Photovoltaic Specialists Conference (PVSC)*, IEEE 43rd, pp. 1506-1510, 2016.
- [23] D. Huh, J.H. Shin, M. Byun, S. Son, P.H. Jung, H.J. Choi, Y.D. Kim, H. Lee, "Analysis of long-term monitoring data of PV module with SiO_x-based anti-reflective patterned protective glass", *Solar Energy Materials and Solar Cells*, vol.170, pp. 33-38, 2017.
- [24] Y.Yuan, X.Lu, G.Yan, R.Hong, Sol-gel preparation of antireflective coating with abrasion resistance by base/acid double catalysis and surface treatment, *Solar Energy*, 155, 2017, 1366-1372
- [25] S. Yoon, G. Turner, V. Garboushian, Thin, lightweight, 18% efficient space silicon solar cell and array, 25th IEEE PV Conference, 1996, Washington DC USA, pp. 259-262.
- [26] W. Abeygunasekara, V. Karunaratne, P. Hiralal, "Numerical Modelling of Zinc Oxide Nanowire Anti Reflective Coating", 10th IEEE International Conference on Industrial and Information Systems ICIIS, 2015, Sri Lanka, pp. 244-249.
- [27] X. Huang, Y. Yuan, S. Liu, W. Wang, R. Hong, "One-step sol-gel preparation of hydrophobic antireflective SiO₂ coating on poly(methyl methacrylate) substrate", *Materials Letter*, vol. 208, pp. 62-64, 2017.
- [28] D.Adak, S.Ghosh, P.Chakrabarty, A.Mondal, H.Saha, R.Mukherjee, R.Bhattacharyya, Self-cleaning V-TiO₂:SiO₂ thin-film coating with enhanced transmission for solar glass cover and related applications, *Solar Energy*, vol. 155, pp. 410-418, 2017.
- [29] G.Womack, P.M.Kaminski, J.M.Walls, "High Temperature Stability of Broadband Anti-reflection Coating on Soda Lime Glass for Solar Modules", *Photovoltaic Specialist Conference (PVSC)*, 2015 IEEE 42nd, LA USA.

- [30] P.M. Kaminski, G. Womack, J.M. Walls, "Broadband Anti-reflection coating for thin film photovoltaics", Photovoltaic Specialist Conference (PVSC), 2014 IEEE 40th, Denver USA.

BIOGRAPHIES



NAZMİ EKREN received the B.S. degree from the Electrical Engineering Department, Yildiz Technical University (YTU), Istanbul, Turkey, in 1987, and the M.S. degrees from the Marmara University in 1989 and PhD degrees from the Istanbul University in 1996. He is currently an Assistant Professor at the Marmara University. His research interests PV systems, Nano technology and lighting.

Design of Unified Power Quality Conditioner for Power Quality Improvement in Distribution Network

S. Biricik

Abstract—Unified Power Quality Conditioner (UPQC) is one of the most advanced Custom-Power-Devices in use today to improve the quality of Power (PQ) in the distribution network. UPQC compensates both voltage and current related PQ disturbances. Its control in unbalanced and distorted weak grid condition is of research interest. Also the performance of UPQC in the presence of unbalanced and non-linear harmonic loads is critical to maintain desirable PQ. In this work, a Self-Tuning Filter (STF) is implemented on the controller part to improve the performance of UPQC in the weak grid voltage along with current unbalance and distortion. The studied control structure gives an adequate voltage and current compensation for voltage sag with distorted voltage conditions, and also for unbalanced current conditions. A three-phase system is modelled in MATLAB/Simulink. The results of simulation study are presented to verify the effectiveness of the proposed control technique.

Index Terms—UPQC, Voltage Sag, Unbalanced Voltages, Voltage Harmonics, Current Harmonics, STF.

I. INTRODUCTION

VOLTAGE distortions and fluctuations are frequently encountered in the weak grid network systems. The distorted load currents cause non-sinusoidal voltage drops and as a result the network voltages become distorted. On the other hand, voltage sag and swell problems are usually caused by short-circuit current flowing into a fault. Voltage sag and swell are defined as a sudden reduction or rise of grid voltages from its nominal value. Unified Power Quality Conditioner (UPQC) is one of the most advanced custom power devices to solve such power quality problems [1, 2]. UPQC is a combination of series active filter and shunt active power filters, connected back-to-back on a common DC link capacitor. The series part of the UPQC is liable for managing of the network side voltage disturbances: voltage unbalance, sags/swells, voltage flicker, and harmonics. It inserts voltages so as to maintain the load voltages at a desired level; balanced and distortion free. The shunt part is responsible for managing the current quality problems caused by the consumer: poor power factor, load harmonic currents, load unbalance etc. A 12-kVA DSP controlled laboratory prototype UPQC has been designed and installed at the DIT Lab to test all of the above mentioned quality [3].

S. BİRİCİK, is with Department of Electrical & Electronics Engineering, European University of Lefke, Northern Cyprus TR 10 Mersin, Turkey, (e-mail: sbiricik@eul.edu.tr) 

Manuscript received July 9, 2017; accepted November 16, 2017.
DOI: [10.17694/bajece.402009](https://doi.org/10.17694/bajece.402009)

As the UPQC can compensate most of the existing PQ problems in the distribution grid, integration of a UPQC in the DG integrated network can be multipurpose. Different integration techniques with their pros and cons are discussed in [4]. Recently published article shows that UPQC can improve the power quality in microgrid system with their intelligent islanding and seamless reconnection techniques [5, 6].

The performance of the UPQC depends on the appropriate design of the components, generation of reference signals and selection of control strategy. As the UPQC is a back-to-back combination of series and shunt active power filter (SAPF) and is directly connected to a dc link capacitor, both the design and controlling mechanism of the APF in terms of the series and parallel connection are very important. Design parameters for both shunt and series part of APF are calculated from [7, 8].

Generation of appropriate switching patterns or gating signals with reference to command the compensating signals determines the control strategy of any compensating devices. It becomes challenging when the unbalance and distorted grid voltage/current are exist in the grid. Recent studies show that self-tuning filter (STF) is introduced in the control part for most of the compensating devices. It helps to filter out the harmonics from the signal and also calculate the balanced condition to create the precise reference waveform. Some of the examples of implementing STF can be found in [9-16]. STF is mostly used as a filter to extract current harmonics in the controller of SAPF [9-14] and hybrid active power filter [15]. It is also proposed in the control of dynamic voltage restorer (DVR) with dc linked storage to improve its performance in case of weak grid condition [16]. Its performance in DVR and shunt APF encourages to exploit its opportunity to improve the performance of UPQC and specially in the un-balanced and distorted grid condition. Therefore, STF is introduced in this study to improve the performance of the UPQC. The stimulating part of this study is to observe the performance of STF to generate the reference current precisely in the case of combination of shunt and series APF and connected back-to-back with a common dc-link capacitor. It is worth to mention that compare to DVR with separate energy storage, self-stored series APF in UPQC requires high fluctuation of source current in the event of voltage sag. The performance of UPQC is studied in the case of both non-ideal grid voltages and unbalanced voltage sag with current harmonics. Fig 1 gives the studied UPQC topology.

This paper has been organized as follows. The improved control method with STF for the control of UPQC is described

in Section II. Based on the control method and design parameters, simulation results of a UPQC placed in a weak grid distribution network are discussed in Section III which is followed by concluding remarks in Section IV.

II. CONTROL OF THE UPQC

First aim of the UPQC is to suppress the voltage harmonics, \tilde{u}_s , then regulation of the voltage amplitudes at the system frequency, \tilde{v}_s to obtain the pure sinusoidal voltage waveforms on the load terminal as

$$v_s(t) = \sqrt{2} \cdot 230 \sin(\omega t + \theta) \tag{1}$$

the STF is used in the studied control system . In this case, the sensed utility voltages (v_{sa}, v_{sb}, v_{sc}) are transformed first into two phase coordinate system using the Clarke (or α - β) transformation:

$$\begin{bmatrix} v_{s\alpha}(t) \\ v_{s\beta}(t) \end{bmatrix} = \sqrt{\frac{2}{3}} \begin{bmatrix} 1 & -\frac{1}{2} & -\frac{1}{2} \\ 0 & \frac{\sqrt{3}}{2} & -\frac{\sqrt{3}}{2} \end{bmatrix} \begin{bmatrix} v_{sa}(t) \\ v_{sb}(t) \\ v_{sc}(t) \end{bmatrix} \tag{2}$$

The obtained voltage waveforms by (2) are processed with (4) as described in [11].

$$\begin{aligned} \bar{v}_{s\alpha}(s) &= \frac{K_1}{s} [v_{s\alpha}(s) - \bar{v}_{s\alpha}(s)] - \frac{\omega}{s} \bar{v}_{s\beta}(s) \\ \bar{v}_{s\beta}(s) &= \frac{K_1}{s} [v_{s\beta}(s) - \bar{v}_{s\beta}(s)] + \frac{\omega}{s} \bar{v}_{s\alpha}(s) \end{aligned} \tag{3}$$

Then, the waveforms obtained in (3) is converted to the three phase system by using following Clarke transformation :

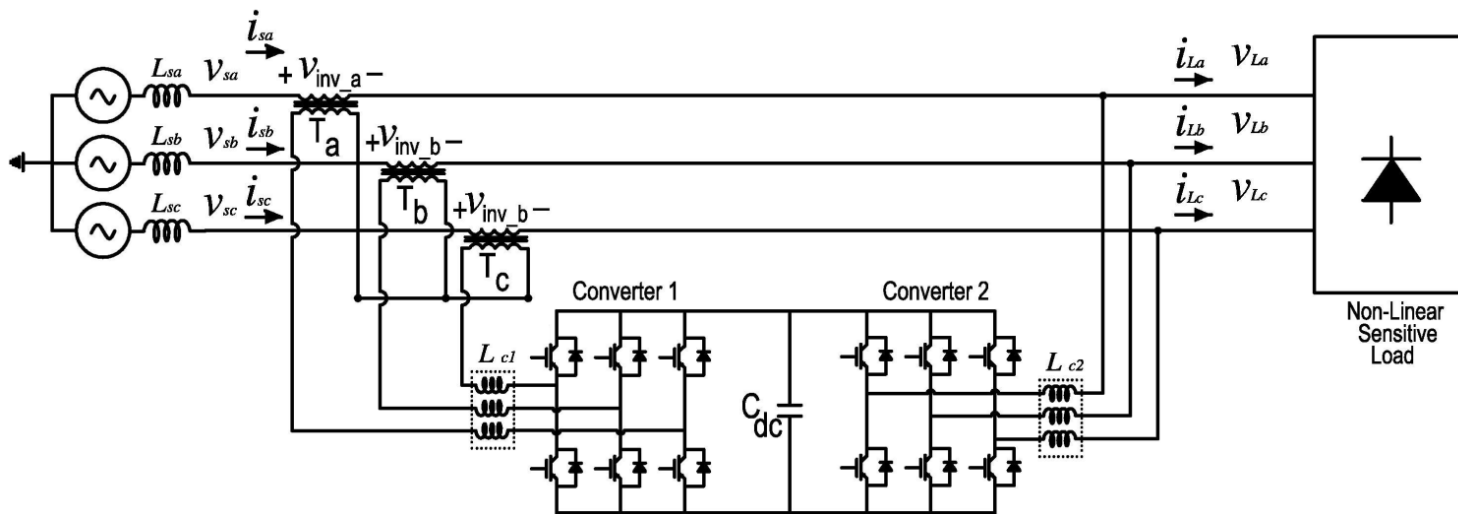
$$\begin{bmatrix} \bar{u}_{s\alpha}(t) \\ \bar{u}_{s\beta}(t) \\ \bar{u}_{sc}(t) \end{bmatrix} = \sqrt{\frac{2}{3}} \begin{bmatrix} 0 & 1 \\ \frac{\sqrt{3}}{2} & -\frac{1}{2} \\ -\frac{\sqrt{3}}{2} & -\frac{1}{2} \end{bmatrix} \begin{bmatrix} \bar{u}_{s\alpha}(t) \\ \bar{u}_{s\beta}(t) \end{bmatrix} \tag{4}$$

The result of (4) are voltage waveforms at the 50 Hz. However, the obtained waveforms may have voltage sag or swell due to the network fluctuations. Therefore, these waveforms cannot be used as reference source signals. To obtain reference signals for each phase, first the amplitude of the determined voltages ($V_{sa}', V_{sb}', V_{sc}'$) from (4) are calculated, and then divided with the obtained waveforms for each phase from (5) as,

$$\sin(\omega t + \theta) = \frac{\bar{v}_s(t)}{V_s'} \tag{5}$$

Eq. (5) can be used to obtain unity sine functions for each phase which will be vary between $\pm 1V$. Lastly, the reference source voltage waveforms can be determined by multiplying standard utility voltage peak (amplitude) level, U_s^* , which is $\sqrt{2} \cdot 230$. The reference source voltage, $u_s^*(t)$, is given by,

$$u_s^*(t) = \sqrt{2} \cdot 230 \sin(\omega t + \theta) \tag{6}$$



A. Fig.1. Topology of the Studied Unified Power Quality Conditioner

Then the expected reference voltages for compensation, $u_c^*(t)$, which are required to induce over the secondary side of the transformer, can be determined by subtracting it from the measured utility voltages, v_s , that is,

$$v_c^*(t) = v_s(t) - v_s^*(t) \tag{7}$$

Results of (7), under ideal condition mean that the source voltages are as described in (1) will be zero. Therefore, the

Converter 1 will turn off. However, results of (7) during voltage sag and harmonic pollution on the source will be as

$$v_c^*(t) = v_{inv}(t) + \tilde{v}_s(t) \tag{8}$$

Therefore, the generated reference voltages are subtracted from the sensed induced voltages on the secondary sides of the coupling transformers (Converter 1 output) for each phases.

$$e(t) = v_c^*(t) - v_{sec}(t) \tag{9}$$

where $e(t)$ is the error signal. Finally, the obtained errors for the phases by (9) are used to drive Converter 1 by generating PWM pulses. In order to determine load current harmonics, the currents on the load terminal are converted to dq frame as

$$\begin{bmatrix} i_d \\ i_q \\ i_0 \end{bmatrix} \sqrt{\frac{2}{3}} \begin{bmatrix} \cos\theta & \cos\left(\theta - \frac{2\pi}{3}\right) & \cos\left(\theta + \frac{2\pi}{3}\right) \\ -\sin\theta & -\sin\left(\theta - \frac{2\pi}{3}\right) & -\sin\left(\theta + \frac{2\pi}{3}\right) \\ \frac{1}{\sqrt{2}} & \frac{1}{\sqrt{2}} & \frac{1}{\sqrt{2}} \end{bmatrix} \begin{bmatrix} i_{La} \\ i_{Lb} \\ i_{Lc} \end{bmatrix} \tag{10}$$

As well known that, the un-equal line currents are one of the most important power quality problem. This problem also may reduce compensation performance of APF controllers. Accordingly, the determined i_d and i_q current waveforms by (10) are also processed using second STF in the studied control structure in order to determine balanced current waveforms at the fundamental frequency.

$$\begin{aligned} \bar{i}_d(s) &= \frac{K_2}{s} (i_d(s) - \bar{i}_d(s)) - \frac{\omega}{s} \cdot \bar{i}_q(s) \\ \bar{i}_q(s) &= \frac{K_2}{s} (i_q(s) - \bar{i}_q(s)) + \frac{\omega}{s} \cdot \bar{i}_d(s) \end{aligned} \tag{11}$$

Then the instantaneous currents can be separated to fundamental harmonic current, reactive current and harmonic current harmonics by using (12),

$$\begin{aligned} \tilde{i}_d &= i_d - \bar{i}_d \\ \tilde{i}_q &= i_q \end{aligned} \tag{12}$$

In the most of the control techniques, high pass filters or low pass filters are used to extract harmonic currents from fundamental harmonic. However, there is no need for an additional filter in the studied control structure. Finally, the determined harmonic current waveform, from (12), are then re-converted to three phase reference currents using the inverse synchronous transform as given by,

$$\begin{bmatrix} i_{ca}^* \\ i_{cb}^* \\ i_{cc}^* \end{bmatrix} = \sqrt{\frac{2}{3}} \begin{bmatrix} \cos\theta & -\sin\theta \\ \cos\left(\theta - \frac{2\pi}{3}\right) & -\sin\left(\theta - \frac{2\pi}{3}\right) \\ \cos\left(\theta + \frac{2\pi}{3}\right) & -\sin\left(\theta + \frac{2\pi}{3}\right) \end{bmatrix} \begin{bmatrix} \tilde{i}_d \\ \tilde{i}_q \end{bmatrix} \tag{13}$$

The schematic representation of the proposed method is shown in Fig. 2.

III. SIMULATION RESULTS

In order to test performance of the studied system, a power system model has been implemented in MATLAB/Simulink. The system performance is verified under voltage sag (50%) condition. Moreover, linear and a non-linear load combinations were also used. Detailed of the system parameters for the study are given in Table1.

The first Load ($Load_1$) is used to consume only active current with reactive current. However, the second load ($Load_2$) consume both active and reactive current and injects harmonic current to the network. The simulation blocks of the power and control systems are presented in Figs 2 and 3.

The proposed system is tested for the following cases and conditions;

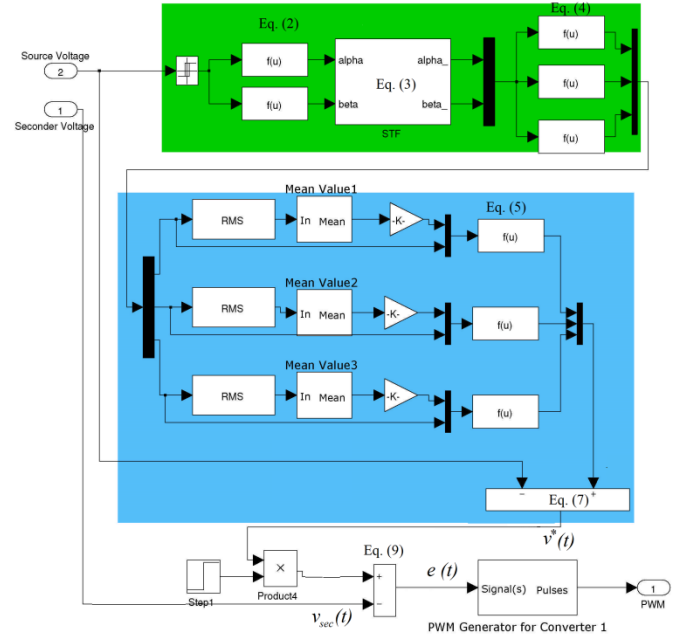


Fig.2. Simulink block diagram of the Converter 1 control

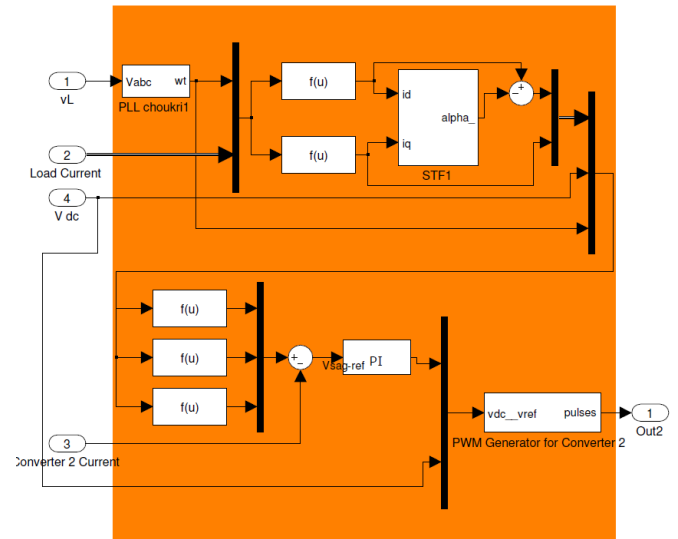


Fig.3. Simulink block diagram of the Converter 2 control

TABLE I
PARAMETERS OF THE STUDIED SYSTEM

Symbol	Quantity	Value
v_s	Ideal Grid L-N rms Voltage	230 V
f	Grid Frequency	50 Hz
$Load_1$	Linear Load Res. and Ind.	4 Ω , 10 mH
$Load_2$	Non-Linear Load Res. and Ind.	24 Ω , 20 mH
$Lc1$	Filter Inductor for Converter 1	0.3 mH
$Lc2$	Filter Inductor for Converter 1	2.5 mH
f_{s1}	Switching Freq. for Converter 1	10 kHz
f_{s2}	Switching Freq. for Converter 1	14 kHz
U_{dc}	DC-Link Source Voltage	750 V
C_{dc}	DC-Link Capacitor Size	2 mF
Kp	Proportional gain for DC link Cont.	0.89
Ki	Integral gain for DC link Cont.	78.96

A. Unbalanced voltages and voltage harmonics on the grid side

The overall system is verified with the adverse grid voltage condition as shown in Fig 4(a). The harmonic distortion in each phases are measured as 9.06 % (229.4V rms) , 9.65 % (229.4V rms) and 7.39 % (231.9V rms), respectively. The system was simulated for 0.3 second and UPQC is activated after 0.05 sec. In order to test the system performance, the voltages are reduced 50 % (voltage sag) between 0.1 to 0.15 sec and voltages are reduced to 117 V at phase-a, 117 V at phase-b and 110.4 V at phase-c. The performance of the system is presented in Fig 4(b) where Converter 1 was immediately injected the required voltages to restore the voltage at the load terminal.

Fig. 4(b) shows the obtained pure sinusoidal voltage waveforms at the load side. With the proposed system, the load voltage harmonics are reduced from 10 % around to 2.10 %, 2.22 %, and 2.01% in each phase. RMS voltage levels are restored from 117 V to 225 V during voltage sag condition on the grid. Fig 4(c) shows the zoomed in load voltages between 0.1 to 0.15 sec during voltage sag on the grid voltages which confirms the balanced and linear voltages are obtained on the load terminal. Thus it shows that STF performs its task perfectly by precisely generating the reference signals and therefore, UPQC provides undistorted and balanced voltage at the load terminal.

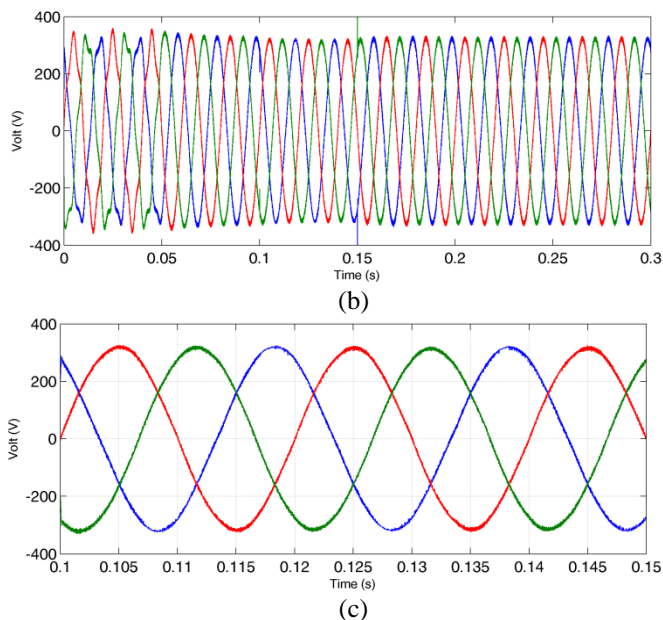
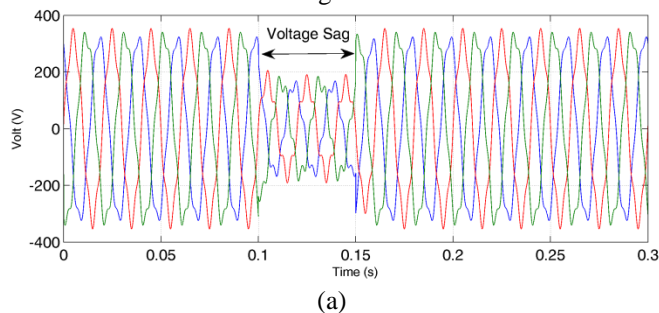


Fig 4. (a) Distorted and unbalanced grid voltages, (b) un-distorted and balanced voltages at the load terminal. (c) voltages at the load terminal during voltage sag (between 0.1 to 0.15 s)

B. Current harmonics on the load terminal

The load currents THD are found 8.99 %, 8.87 % and 9.02 % while the rms currents are 59.43 A, 59.51 A, 59.37 A., as shown in Fig 5(a). The shunt part of UPQC controls the injection of load harmonics to the grid and reactive power compensate by the UPQC. Thus the grid side only supply the fundamental active current required by the load and series APF of UPQC, as shown in Fig 5(b). This figure also confirms the performance of STF by generating the balanced reference current for the supply side during the voltage sag condition. Therefore, UPQC smoothly compensate the voltage sag, reactive and harmonic current at the same time as shown in Fig 4(b) and 5(b) during the period of 0.1 to 0.15 sec. Fig 5(c) shows the performance of the DC link capacitor by maintaining link voltage near to the reference.

C. Power flow analysis

The precisely generated reference signal and the overall control of the UPQC also impact on the power flow within the converters of the UPQC. Fig 6(a) shows the power supply by the grid. During the performance of UPQC, grid only supplies the active power. Therefore, reactive power supplied by the grid is zero. Fig 6(b) shows the power flow within the UPQC. Shunt part of UPQC compensate the reactive and harmonics and therefore Q becomes constant during the operating time. Series APF consumes the active power from the grid to compensate the voltage sag and distortion and this also reflected in Fig 6(a, b). Therefore, load does not sense any disturbance by the grid and thus maintaining constant active and reactive power consumption as shown in Fig 6(c). Moreover, power factor of the system improved with the effective compensation of reactive power.

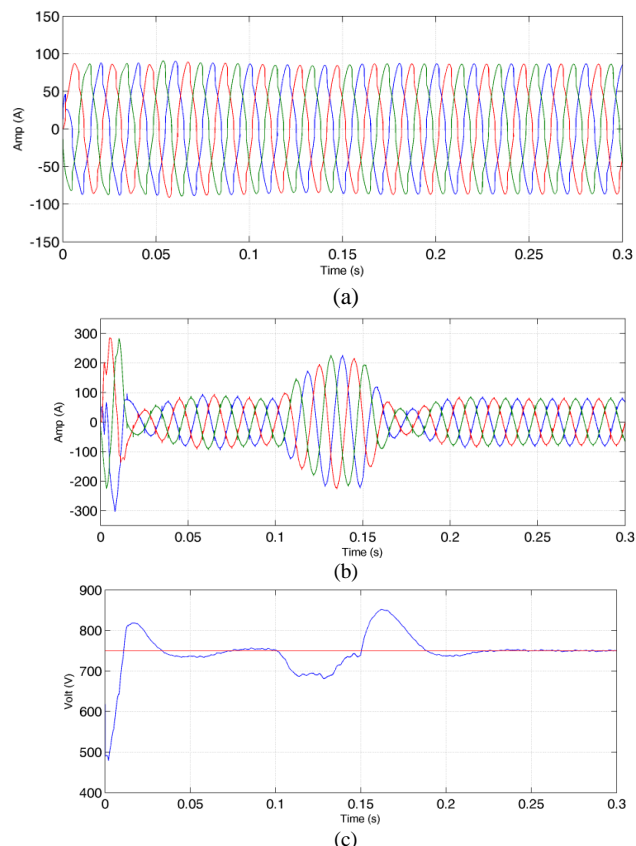


Fig 5. a) Three phase non-linear load currents, b) Grid currents after filtering; c) DC-link voltage profile

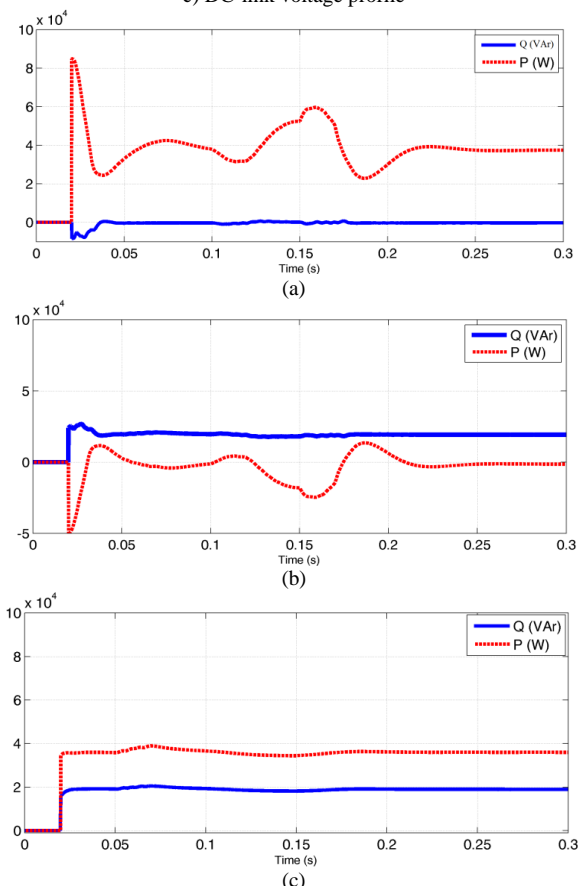


Fig 6. a) supplied powers by the grid; b) by the UPQC and c) consumed powers by the load.

IV. CONCLUSION

Unbalance and distorted voltage conditions are more common now-a-days in the distributed generation integrated network. Harmonic injection by the non-linear and energy efficient load is also increasing. Therefore, precise generation of reference signal for improved control of UPQC is a must. Simulation performance of the UPQC confirms that the inclusion of STF in the controller will add a degree of advantages for better performance of UPQC in distorted and unbalanced grid voltage condition.

REFERENCES

- [1] H Akagi, E H Watanabe and M Aredes, Instantaneous Power Theory and Applications to Power Conditioning, Piscataway, NJ: IEEE Press, 2007
- [2] I Axente, M Basu, M F Conlon, A Control Approach for UPQC Connected to Weak Supply Point, UPEC 2007, p. 619-623.
- [3] I Axente, J N Ganesh, M Basu, M F Conlon, K Gaughan, A 12-kVA DSP-Controlled Laboratory Prototype UPQC Capable of Mitigating Unbalance in Source Voltage and Load Current , IEEE Trans Power Electronics, Vol. 25(6), 2010, pp. 1471 - 1479
- [4] S K. Khadem, M Basu, and M F Conlon, UPQC for power quality improvement in DG integrated smart grid network—A review, Int. J. Emerg. Electr. Power Syst., 2012, vol. 13(1), article 3.
- [5] S K Khadem, M Basu, M F Conlon, Intelligent Islanding and Seamless Reconnection Technique for Microgrid With UPQC," Emerging and Selected Topics in Power Electronics, IEEE Journal of , 2015, vol.3(2), pp.483-492
- [6] S K Khadem, M Basu, and M F Conlon, A new placement and integration method of UPQC to improve the power quality in DG network, UPEC 2013, vol. 1. pp. 1–6.
- [7] S K Khadem, M Basu and M F Conlon, Harmonic power compensation capacity of shunt active power filter and its relationship with design parameters, IET Power Electron., 2013, vol. 7(2), pp. 418–430
- [8] S.K. Khadem, "Power quality improvement of distributed generation integrated network with unified power quality conditioner", Ph.D. dissertation, Dept. Elect. Electron. Eng., Dublin Inst. Technol., Ireland, Europe, Jan. 2013.
- [9] M. Abusalam, P. Poure, S. Karimia, S. Saadate, New Digital Reference Current Generation for Shunt Active Power Filter under Distorted Voltage Conditions, Electric Power Systems Research, 2009, vol. 79, pp 759-76
- [10] A. Ghamri , M. T. Benchouia, A. Golea Sliding-Mode Control Based Three-Phase Shunt Active Power Filter, Simulation and Experimentation, Electric Power Components and Systems, 2012, vol. 40, no. 4, pp. 383-398.
- [11] S. Biricik, S. Redif, O.C.Ozerdem, M Basu, Control of the Shunt Active Power Filter under Non-Ideal Grid Voltage and Unbalanced Load Conditions, UPEC 2013, Dublin, Ireland.
- [12] S S Patnaik, A K Panda, Real-Time Performance Analysis and Comparison of Various Control Schemes for Particle Swarm Optimization-Based Shunt Active Power Filters, Electrical Power and Energy Systems 52 (2013), pp. 185–197.
- [13] S. Biricik, S. Redif, O.C.Ozerdem, S. K. Khadem, M Basu, Real-Time Control of Shunt Active Power Filter under Distorted Grid Voltage and Unbalanced Load Condition using Self Tuning Filter, IET Power Electronics (2014)
- [14] S. Biricik, O.C.Ozerdem, S. Redif and M.O.I. Kmail, Performance Improvement of Active Power Filter under Distorted and Unbalanced Grid Voltage Conditions, Journal of Electronics and Electrical Engineering, 2013, Vol. 19, No.1, pp 35-39
- [15] S.Biricik, O.C.Ozerdem, S.Redif and M.O.I.Kmail, Novel Hybrid Active Power Filter Structure To Compensate Harmonic Currents and Reactive Power, MELECON 2012, 25-28 Mart 2012, Tunisia.
- [16] S. Biricik, S. K. Khadem, S. Redif, M Basu, Control of the Dynamic Voltage Restorer to Improve Voltage Quality, PEDG 2014, Galway, Ireland.

BIOGRAPHIES



SAMET BİRİCİK received his B.Sc. and Ph.D. in electrical and electronic engineering in 2006 and 2013, respectively, from the Near East University, Nicosia, North Cyprus. He won the Best Paper Award from the IEEE 9th International Conference on Environment and Electrical Engineering in the Czech Republic. He was a founding member of the Energy Professionals Association (EPA) and a member of the Cyprus Turkish Chamber of Electrical

Engineers. Between 2006 and 2017, he has worked in various industrial and commercial project engineers. He is currently a research fellow in the School of Electrical and Electronic Engineering of Dublin Institute of Technology in Ireland and a lecturer in the European University of Lefke. His research interests are the application of power electronics, power quality, electrical machines, and high-voltage engineering.

Quaternion-Based Robust Satellite Attitude Tracking Control

J. Dasdemir

Abstract— In this paper, a nonlinear robust quaternion-based controller is developed to address the three-axis attitude tracking control problem of rigid spacecraft in presence of parametric uncertainties, unknown external disturbances and sensor noise. As a first step, a robust controller is designed that compensates parametric uncertainty and disturbance effects. The robust controller then reformulated to deal also with sensor noise. Singularity free unit quaternions are used to represent the attitude of the satellite in three-dimensional space. The Lyapunov-based stability analysis is applied to prove that a uniformly ultimately bounded tracking result is achieved. Simulation results are presented to illustrate the feasibility of the proposed control strategy.

Index Terms— Attitude tracking, unit quaternion, robust control, sensor noise.

I. INTRODUCTION

THE attitude tracking control problem of rigid bodies received much attention for decades due to its application areas ranging from robot manipulators to satellites and still continuous to be an active research area [1-3]. Especially, in applications such as satellite surveillance and communication, a considerable amount of effort has been devoted to solve both stabilization and tracking problems. The challenging nature of the attitude tracking control problem arises not only from the nonlinearity of the dynamics but also the representation of the attitude kinematics. There are several kinematic parameterizations for orientation angles [4]: Three-parameter representations such as Euler angles, Rodriguez parameters and modified Rodrigues parameters, limited because of kinematic singularities and non-singular, four-parameter representation by unit quaternions with a constraint equation. The control problem can be further complicated in presence of parametric uncertainties, unknown disturbances and sensor noise simultaneously.

The attitude control problem of a spacecraft in the presence of disturbance and/or uncertainties has been extensively studied. Many different control strategies including, adaptive control [5-6], sliding mode control [7-8] and robust control methods [9-10] were proposed in the literature and all these methods have their own advantages as well as disadvantages. Sliding mode control is a widely preferred control method due to its simple and inherently robust structure.

However, sliding mode control might excite the high frequency unmodeled dynamics in practical applications [11]. Thus, it can lead to control performance deterioration. A typical adaptive control mechanism is the combination of on-line estimation and control and it has limitations that if uncertain parameters enter the system model in complicated ways, it might be problematic to obtain continuously parameterized control structures and they are also not robust against external disturbances [12-13]. Robust controllers exhibit satisfactory performance against different types of disturbances but they might have large torque demands. Exponential convergence rate with infinite settling time is also a drawback of conventional robust and sliding mode control techniques [14]. In order to eliminate these shortcomings, there are several works on designing finite time control structures mostly based on terminal sliding mode control. However, most of the proposed methods present either slow convergence speed, if state is away from equilibrium, or posses chattering phenomena due to discontinuities [15-16].

All the aforementioned control methods have strength against model uncertainties and/or disturbances. However, none of these papers have considered sensor noise effects. Attitude tracking control of a rigid spacecraft in presence of parametric uncertainties, unknown disturbances and sensor noise is an important problem and should be considered together in control development, in particular for real-time implementations. Performance of a control algorithm also depends on the quality of the available measurements and on-line computation of the algorithm. For applications with demanding sampling times or limited computational resources, this on-line computation requirement can be problematic [17]. If the control law is also contaminated by sensor noise, performance degradation is inevitable. Moreover, low cost, small satellites considered in this study require less energy consumption and do not have sufficient onboard resources to implement complex algorithms [18]. The onboard hardware is usually very limited. Hence, complicated control structures may not perform well particularly in presence of sensor noise. In this work, to overcome this implementation issues, the significant part of the control algorithm formulated without dependence on measurement values. Instead, the predefined desired values have been utilized. Hence, computation burden, sensor contaminations and control energy requirement are relatively reduced.

In this paper, a new robust attitude tracking control method that takes into account the simultaneous effects of parametric uncertainties, external disturbances and measurement noise has been proposed. Firstly, a transformation, introduced in [19] is used for the open-loop tracking error dynamics. As a first step, a typical robust controller is designed to compensate the

J. DASDEMIR is with Department of Control and Automation Eng., Yildiz Technical University, Istanbul, Turkey, (e-mail: janset@yildiz.edu.tr) 

Manuscript received September 19, 2017; accepted January 11, 2018.
DOI: [10.17694/bajece.402013](https://doi.org/10.17694/bajece.402013)

adverse effects of uncertainties in inertia matrix and external disturbances. Then, ultimate boundedness result is obtained through Lyapunov-type stability analysis. Subsequently, to obtain a better performance in the presence of sensor noise, the former control algorithm is exploited to design the new control structure and it is shown that the proposed control method ensures uniformly ultimately bounded attitude tracking.

The paper is organized as follows: Section II provides the dynamic and kinematic model of the satellite. The problem statement and the open-loop error system dynamics are introduced in Section III. In Section IV and V, both standard robust control and the newly proposed control developments are presented. Numerical results are shown in Section VI. Finally, Section VII presents some concluding remarks.

II. MODEL FORMULATION

A. Dynamic Model

Motivated by the need to obtain the dynamic and kinematic model of the rigid spacecraft, two frames denoted by $I = \{x_I, y_I, z_I\}$ and $\mathcal{B} = \{x_B, y_B, z_B\}$ are utilized. Let I be the inertial reference frame and the origin of this orthogonal frame is located in the center of the earth. The other frame \mathcal{B} is the body-fixed frame attached to the center of mass of the satellite. There are also reaction wheels, as actuator mechanisms, located on each axis of the body-fixed frame to control the attitude of the rigid spacecraft. The dynamic model of the satellite can be expressed as follows [20]:

$$J\dot{\omega} = -\omega^\times J\omega + \tau + \tau_d \quad (1)$$

where $J \in \mathbb{R}^{3 \times 3}$ is positive-definite, constant, symmetric inertia matrix, $\omega(t) \in \mathbb{R}^3$ is the angular velocity of the body-fixed frame with respect to the inertial reference frame. $\tau(t) \in \mathbb{R}^3$ is the torque input control vector and $\tau_d \in \mathbb{R}^3$ is a bounded disturbance vector, and the notation $\zeta^\times, \forall \zeta = [\zeta_1 \ \zeta_2 \ \zeta_3]^T$ represents the skew-symmetric matrix:

$$\zeta^\times = \begin{bmatrix} 0 & -\zeta_3 & \zeta_2 \\ \zeta_3 & 0 & -\zeta_1 \\ -\zeta_2 & \zeta_1 & 0 \end{bmatrix} \quad (2)$$

Property 1: The inertia matrix can be lower and upper bounded by the following inequalities:

$$j_1 \|\xi\|^2 \leq \xi^T J \xi \leq j_2 \|\xi\|^2 \quad \forall \xi \in \mathbb{R}^3 \quad (3)$$

Where $j_1, j_2 \in \mathbb{R}$ are some positive constants, and $\|\cdot\|$ denotes the standard Euclidean norm.

Remark 1: The disturbance vector $\tau_d(t) = [\tau_{d1}(t), \tau_{d2}(t), \tau_{d3}(t)]^T$ can be upper bounded as follows:

$$\|\tau_d\| \leq \xi_{td} \quad (4)$$

B. Kinematic Model

In this this work, kinematics of the satellite will be described using unit quaternions, due to their nonsingular and computationally effective representation. According to the Euler's Theorem, any rotation matrix can be defined uniquely by a rotation angle $\vartheta(t) \in \mathbb{R}$ about an appropriate unit vector

$k(t) \in \mathbb{R}^3$. Thus, based on a given $(\vartheta, k) \in \mathbb{R}^4$, an alternative parametrization of the attitude can be obtained by four-parameter unit quaternions as follows [20]:

$$q_0(t) \triangleq \cos\left(\frac{1}{2}\vartheta\right) \quad (5)$$

$$q_v(t) \triangleq k \sin\left(\frac{1}{2}\vartheta\right) \quad (6)$$

In Equations (5) and (6), $q(t) = \{q_0(t), q_v(t)\} \in \mathbb{R} \times \mathbb{R}^3$ denotes the unit quaternion defining the orientation of the body-fixed frame \mathcal{B} with respect to the inertial frame I , subject to the constraint

$$q_v^T q_v + q_0^2 = 1 \quad (7)$$

The rotation matrix $R(q_0, q_v) \in SO(3)$ that brings I onto \mathcal{B} can be calculated as

$$R = (q_0^2 - q_v^T q_v)I_3 + 2q_v q_v^T - 2q_0 q_v^\times \quad (8)$$

where $I_3 \in \mathbb{R}^{3 \times 3}$ represents 3×3 identity matrix. Hence, the differential equation describing the attitude kinematics of the satellite can be expressed by using unit quaternions as follows [21]:

$$\dot{q}_0 = -\frac{1}{2} q_v^T \omega \quad (9)$$

$$\dot{q}_v = \frac{1}{2} (q_v^\times \omega + q_0 \omega) \quad (10)$$

Equations (9) and (10) can be modified as

$$\dot{q} = \frac{1}{2} \Sigma(q) \omega \quad (11)$$

where $\Sigma(q) = [\Sigma_0^T, \Sigma_v^T]^T \in \mathbb{R}^{4 \times 3}$ with $\Sigma_0 = -q_v^T$ and $\Sigma_v = q_v^\times + q_0 I_3$ respectively. The angular velocity of the body-fixed frame with respect to the inertial frame expressed in the body-fixed frame can be obtained according to Equations (9) and (10) in the following form:

$$\omega = 2(q_0 \dot{q}_v - q_v \dot{q}_0) - 2q_v^\times \dot{q}_v \quad (12)$$

III. PROBLEM STATEMENT AND QUATERNION ERROR DYNAMICS

In order to express the desired attitude of the satellite, another body-fixed reference frame $\mathcal{B}_d = \{x_{B_d}, y_{B_d}, z_{B_d}\}$ is defined. The orientation of this frame with respect to the inertial frame can be defined by the desired unit quaternion $q_d(t) \triangleq \{q_{0d}(t), q_{vd}(t)\} \in \mathbb{R} \times \mathbb{R}^3$ with a similar constraint given in Equation (7):

$$q_{vd}^T q_{vd} + q_{0d}^2 = 1 \quad (13)$$

The rotation matrix that brings inertial frame I onto the desired reference body-fixed frame \mathcal{B}_d can be calculated as

$$R_d = (q_{0d}^2 - q_{vd}^T q_{vd})I_3 + 2q_{vd} q_{vd}^T - 2q_{0d} q_{vd}^\times \quad (14)$$

The relation between the desired unit quaternion and the angular velocity of the desired body-fixed reference frame with respect to the inertial frame expressed in desired frame $\omega_d(t) \in \mathbb{R}^3$ can be stated as follows:

$$\dot{q}_{0d} = -\frac{1}{2}q_{vd}^T \omega_d \quad (15)$$

$$\dot{q}_v = \frac{1}{2}(q_v^\times \omega + q_0 \omega) \quad (16)$$

Through the help of $\Sigma_d(q) = [\Sigma_{0d}^T, \Sigma_{vd}^T]^T \in \mathbb{R}^{4 \times 3}$ with $\Sigma_{0d} = -q_{vd}^T$ and $\Sigma_{vd} = q_{vd}^\times + q_{0d}I_3$ respectively, Equations (15-16) can be written in a compact form as

$$\dot{q}_d = \frac{1}{2}\Sigma_d(q)\omega_d \quad (17)$$

Utilizing Equations (15-16), the desired angular velocity can be obtained as:

$$\omega_d = 2(q_{0d}\dot{q}_{vd} - q_{vd}\dot{q}_{0d}) - 2q_{vd}^\times \dot{q}_{vd} \quad (18)$$

In order to achieve the control objective, the attitude of the body-fixed frame \mathcal{B} should track the desired body-fixed frame \mathcal{B}_d . To describe this objective, an attitude tracking error term $\tilde{R}(e_0, e_v) \in \mathbb{R}^{3 \times 3}$, defining the mismatch, stated in the following as performance criteria

$$\tilde{R} \triangleq RR^T = (e_0^2 - e_v^T e_v)I_3 + 2e_v e_v^T - 2e_0 e_v^\times \quad (19)$$

where the quaternion tracking error $e(t) \triangleq \{e_0(t), e_v(t)\} \in \mathbb{R} \times \mathbb{R}^3$ can be represented explicitly as follows with a similar constraint given in Equation (7).

$$e_0 = q_0 q_{0d} + q_v^T q_{vd} \quad (20)$$

$$e_v = q_{0d} q_v - q_0 q_{vd} + q_v^\times q_{vd} \quad (21)$$

$$e_v^T e_v + e_0^2 = 1 \quad (22)$$

Note that according to the Equation (19), the control goal will be achieved as the mismatch term converges to the identity matrix as follows

$$\lim_{t \rightarrow \infty} \tilde{R} \rightarrow I_3 \quad (23)$$

It is obvious that Equation (23) will be guaranteed if the following condition is satisfied

$$\|e_v(t)\| \rightarrow 0 \Rightarrow |e_0| \rightarrow 1 \quad (24)$$

and according to Equation (22)

$$0 \leq \|e_v(t)\| \leq 1, \quad 0 \leq |e_0(t)| \leq 1 \quad (25)$$

The angular velocity tracking error can also be defined by the use of Equation (19) in the following form

$$\tilde{\omega} = \omega - \tilde{R}\omega_d \quad (26)$$

Based on the previous formulations, specifically, using Equation (1), (9-10), (15-16), (20-21) and (26) The open loop tracking error dynamics of the satellite to be controlled can be obtained as follows

$$J\dot{\tilde{\omega}} = -(\tilde{\omega} + \tilde{R}\omega_d)^\times J(\tilde{\omega} + \tilde{R}\omega_d) + J(\tilde{\omega}^\times \tilde{R}\omega_d - \tilde{R}\dot{\omega}_d) + \tau + \tau_d \quad (27)$$

$$\dot{e}_v = \frac{1}{2}(e_v^\times + e_0 I_3)\tilde{\omega} \quad (28)$$

$$\dot{e}_0 = -\frac{1}{2}e_v^T \tilde{\omega} \quad (29)$$

Remark 2: It is supposed that both $q_{0d}(t)$ and $q_{vd}(t)$ and their first two time derivatives are bounded. Thus, $\omega_d(t)$ and its derivative are bounded for all time.

Equation (28) can be modified with the use of $T(e_0, e_v) \in \mathbb{R}^{3 \times 3}$ as defined below

$$T \triangleq e_v^\times + e_0 I_3 \quad (30)$$

$$\dot{e}_v = \frac{1}{2}T\tilde{\omega} \quad (31)$$

Taking the time derivative of (31) and premultiplying both sides of the resulting equation by $T^{-T}JT^{-1}$

$$J^* \ddot{e}_v = \frac{1}{2}J^* \dot{T} \tilde{\omega} + \frac{1}{2}P^T J \dot{\tilde{\omega}} \quad (32)$$

can be obtained where $J^*(e_v, e_0) \in \mathbb{R}^{3 \times 3}$ and $P(e_v, e_0) \in \mathbb{R}^{3 \times 3}$ are defined as follows:

$$J^* \ddot{e}_v = \frac{1}{2}J^* \dot{T} \tilde{\omega} + \frac{1}{2}P^T J \dot{\tilde{\omega}} \quad (33)$$

$$J^* \triangleq P^T J P \quad (34)$$

After substituting (27) into (32), the following open loop error dynamics can be attained

$$J^* \ddot{e}_v + C^* \dot{e}_v + N^* - \tau_d^* = \tau^* \quad (35)$$

where the new terms $\tau^* \in \mathbb{R}^3$, $\tau_d^* \in \mathbb{R}^3$, $C^*(e_v, e_0, \dot{e}_v) \in \mathbb{R}^{3 \times 3}$ and $N^*(e_v, e_0, \dot{e}_v, \omega_d, \dot{\omega}_d) \in \mathbb{R}^3$ are defined as

$$\tau^* \triangleq \frac{1}{2}P^T \tau \quad (36)$$

$$\tau_d^* \triangleq \frac{1}{2}P^T \tau_d \quad (37)$$

$$C^* \triangleq -J^* \dot{P}^{-1} P - 2P^T (J P \dot{e}_v)^\times P \quad (38)$$

$$N^* \triangleq P^T [(P\dot{e}_v)^{\times} J\tilde{R}\omega_d] + P^T \left[(\tilde{R}\omega_d)^{\times} P\dot{e}_v \right] - \frac{1}{2} P^T J [(2P\dot{e}_v)^{\times} \tilde{R}\omega_d - \tilde{R}\dot{\omega}_d] + \frac{1}{2} P^T \left[(\tilde{R}\omega_d)^{\times} J\tilde{R}\omega_d \right] \quad (39)$$

The following property will be utilized in the subsequent controller design and analysis sections

Property 2: The inertia and the centripetal- Coriolis matrices satisfy the following skew-symmetric property

$$\xi^T \left(\frac{1}{2} J^* - C^* \right) \xi = 0 \quad \forall \xi \in \mathbb{R}^3 \quad (40)$$

Remark3: Note that the Jacobian matrix in Equation (30) can be invertible, if the following condition is satisfied

$$\det(T) = e_0(t) \neq 0, \quad \forall t \in [0, \infty) \quad (41)$$

To guarantee Equation (41), initial conditions should be restricted that $e_0(0) \neq 0$ and the proposed control method should also provide $e_0(t) \neq 0$. It is obvious from Equation (24) and (20) that the desired trajectory can be initialized to ensure that $e_0(0) \neq 0$.

IV. ROBUST CONTROL DEVELOPMENT

In this section, the objective is to design a robust attitude-tracking controller for the open-loop error dynamics given in Equation (35) under the assumption that the satellite inertia matrix and disturbance vector are unknown. To quantify the mismatch, the parameter estimation error, $\tilde{\theta} \in \mathbb{R}^6$ and the disturbance estimation error, $\tilde{\tau}_d^* \in \mathbb{R}^3$ are defined as

$$\tilde{\theta} \triangleq \theta - \hat{\theta} \quad (42)$$

$$\tilde{\tau}_d^* = \tau_d^* - \hat{\tau}_d^* \quad (43)$$

where $\hat{\theta}$ and $\hat{\tau}_d^*$ are the best guess-estimates of the unknown vector of inertia parameters $\theta \in \mathbb{R}^6$ and the disturbance vector $\tau_d^* \in \mathbb{R}^3$ respectively.

In order to facilitate the subsequent development, a filtered tracking error $r(t) \in \mathbb{R}^3$ is expressed as follows:

$$r \triangleq \dot{e}_v + \alpha e_v \quad (44)$$

where $\alpha \in \mathbb{R}^{3 \times 3}$ is a positive-definite, constant, diagonal control gain matrix.

A. Robust Control Design

Based on the open-loop error system dynamics given in Equation (35) and the subsequent stability analysis, the control torque input is designed as follows:

$$\tau^* = -\hat{F} - Kr - v_r - \frac{e_v}{(1 - e_v^T e_v)^2} \quad (45)$$

where $K \in \mathbb{R}^{3 \times 3}$ is a constant, positive-definite, diagonal control gain matrix and $\hat{F}(e_v, e_0, \dot{e}_v, \omega_d, \dot{\omega}_d) \in \mathbb{R}^3$ is defined as

$$\hat{F} \triangleq Y(\cdot)\hat{\theta} + \hat{\tau}_d^* \quad (46)$$

The first term $Y(e_v, e_0, \dot{e}_v, \omega_d, \dot{\omega}_d)\hat{\theta}$ is formed based on the following parameterization

$$Y(\cdot)\theta \triangleq J^* \alpha \dot{e}_v + C^* \alpha e_v - N^* \quad (47)$$

Hence, the resulting mismatch term can be defined as

$$\tilde{F} \triangleq F - \hat{F} = Y\tilde{\theta} + \tilde{\tau}_d^* \quad (48)$$

where F contains the unknown vector of inertia parameters and the disturbance vector as follows:

$$F = Y\theta + \tau_d^* \quad (49)$$

Based on the boundedness assumption of the disturbance vector as indicated in Remark 1, Property 1, the boundedness property of the rotation matrixes and with the use of Equation (39), the mismatch term $\tilde{F}(e_v, e_0, \dot{e}_v, \omega_d, \dot{\omega}_d) \in \mathbb{R}^3$ can be upper bounded in the following way [22]

$$\|\tilde{F}\| \leq \rho_1(e_v, e_0, \dot{e}_v, \omega_d, \dot{\omega}_d) + \rho_2(\cdot) = \rho(\cdot) \quad (50)$$

where $\rho(\cdot) \in \mathbb{R}$ denotes positive bounding constant and ρ_1, ρ_2 are positive, scalar, known bounding functions related with the parameter estimation error and the disturbance estimation error with residuals respectively. In Equation (45), the robust term, $v_r(t) \in \mathbb{R}^3$ is designed for attenuation of the mismatch and can be defined as

$$v_r = \frac{\rho^2 r}{\rho \|r\| + \varepsilon} \quad (51)$$

where $\varepsilon \in \mathbb{R}$ is an arbitrarily small positive design constant.

Taking the time derivative of Equation (44), premultiplying both sides of that equation by J^* and substituting Equation (35) and (44) for \dot{e}_v into the resulting equation, the following expression can be obtained

$$J^* \dot{r} = -C^* r + F + \tau^* \quad (52)$$

After substituting Equation (45) into Equation (52), the final closed-loop error system can be obtained in the following form:

$$J^* \dot{r} = -C^* r + \tilde{F} - Kr - v_r - \frac{e_v}{(1 - e_v^T e_v)^2} \quad (53)$$

where \tilde{F} was defined in Equation (48).

B. Stability Analysis

Theorem1: Given the closed-loop error dynamics in Equation (53), the robust control law proposed in Equation (45) ensures uniformly ultimately bounded attitude tracking in the sense that

$$\|e_v(t)\| \rightarrow \gamma_1 \exp(-\gamma_2 t) + \gamma_3, \quad \gamma_1, \gamma_2, \gamma_3 \in \mathbb{R} \quad (54)$$

provided that the initial conditions are selected to satisfy

$$e_0(0) \neq 0 \quad (55)$$

Proof: To prove Theorem 1, a nonnegative function $V_1(t) \in \mathbb{R}$ is defined as follows:

$$V_1 = \frac{1}{2} [e_v^T e_v / (1 - e_v^T e_v)] + \frac{1}{2} r^T J^* r \quad (56)$$

Note that the function $V_2(t)$ can be upper and lower bound as

$$\lambda_1 \|z\|^2 \leq V_1(t) \leq \lambda_2 \|z\|^2 \quad (57)$$

where $\lambda_1, \lambda_2 \in \mathbb{R}$ are known positive bounding constants and $z(t) \in \mathbb{R}^6$ is defined as

$$z \triangleq \left[e_v^T / \sqrt{1 - e_v^T e_v} \quad r^T \right]^T \quad (58)$$

After taking the time derivative of Equation (56), using Equations (44), (33), (53) and Property 2, the following expression for the time derivative of $V_1(t)$ can be obtained

$$\dot{V}_1 = -\frac{e_v^T \alpha e_v}{(1 - e_v^T e_v)^2} - r^T K r - r^T v_r + r^T \tilde{F} \quad (59)$$

Substituting Equation (51) into Equation (59) and with the use of the definition given in Equation (58) and the inequality given in Equation (50), the expression in Equation (59) can be upper bound

$$\dot{V}_1 \leq -\beta \|z\|^2 + \rho \|r\| - \frac{\rho^2 \|r\|^2}{\rho \|r\| + \varepsilon} \quad (60)$$

where $\beta = \lambda_{\min}\{\alpha, K\} \in \mathbb{R}$. after mathematical manipulations, Equation (60) can be written as follows:

$$\dot{V}_1 \leq -\beta \|z\|^2 + \varepsilon \quad (61)$$

The inequality given in Equation (57) can be applied to lower bound $\|z\|^2$ as

$$\|z\|^2 \geq \frac{1}{\lambda_2} V_1(t) \quad (62)$$

Hence, the inequality in Equation (61) can be written in the following form

$$\dot{V}_1(t) \leq -\sigma V_1(t) + \varepsilon \quad (63)$$

where $\sigma = \frac{\beta}{\lambda_2} \in \mathbb{R}$. The following expression can be found when linear differential inequality is solved

$$V_1(t) \leq V_1(0) \exp(-\sigma t) + \frac{\varepsilon}{\sigma} [1 - \exp(-\sigma t)] \quad (64)$$

From Equations (56) and (64), it can be shown that $r(t) \in \mathcal{L}_\infty$. Equation (44) can be used to obtain $e_v(t), \dot{e}_v(t) \in \mathcal{L}_\infty$. Equations (22), (25) and (28) reveals that $\tilde{\omega}(t) \in \mathcal{L}_\infty$. Equation (26) shows $\omega(t) \in \mathcal{L}_\infty$. Hence, it can be proved that the control signal $\tau^* \in \mathcal{L}_\infty$. Standard signal chasing arguments can be employed to show that all other signals remain bounded.

From the inequalities in Equation (57) and (64), it can be concluded that

$$\|z\|^2 \leq \frac{\lambda_2}{\lambda_1} \|z(0)\|^2 \exp\{-\sigma t\} + \frac{\varepsilon}{\sigma \lambda_1} \quad (65)$$

Hence, it can be seen from Equation (65) that the objective given in Equation (54) is achieved.

V. ROBUST CONTROL REFORMULATION

In this section, the goal is to improve the robustness properties against sensor contamination through the redesign of the control structure proposed in (45) and thus to improve the performance under the assumption of measurement noise, parametric uncertainties and unknown disturbances.

Notice that the first term $\hat{F}(\cdot)$ of the proposed controller introduced in Equation (45) is formulated in terms of the error terms obtained by the use of measurement values. However, it constitutes the aforementioned complications such as computational burden of on-line computation requirement and sensor contamination. Hopefully, the following control structure can reduce these drawbacks by reformulating the term $\hat{F}(\cdot)$ as a function of the desired attitude, angular velocity and acceleration terms.

Based on the open-loop dynamics in Equation (35), and the subsequent stability analysis, the control torque input is designed as follows:

$$\tau^* = -\hat{F}_d - K r - v_r - \frac{e_v}{(1 - e_v^T e_v)^2} \quad (66)$$

where $K \in \mathbb{R}^{3 \times 3}$ is a constant, positive-definite, diagonal control gain matrix, the term $v_r(t)$ is defined as in Equation (51) with a bounding constant yet to be designed and $\hat{F}_d(e_v, e_0, \dot{e}_v, \omega_d, \dot{\omega}_d) \in \mathbb{R}^3$ is defined as

$$\hat{F}_d \triangleq Y_d(\cdot) \hat{\theta} + \hat{\tau}_d^* \quad (67)$$

The term $Y_d(\omega_d, \dot{\omega}_d) \hat{\theta}$ is formed based on the following parameterization

$$Y_d \theta = -\frac{1}{2} J \dot{\omega}_d - \frac{1}{2} \omega_d^x J \omega_d \quad (68)$$

After substituting Equation (66) into Equation (52) and adding and subtracting the term $Y_d \theta$ to the right hand side of the resulting equation, the following expression for the closed-loop error system can be obtained

$$J^* \dot{r} = -C^* r + \psi - K r - v_r - \frac{e_v}{(1 - e_v^T e_v)^2} \quad (69)$$

where the mismatch term $\psi(e_v, e_0, \dot{e}_v, \omega_d, \dot{\omega}_d) \in \mathbb{R}^3$ and $\tilde{Y}(e_v, e_0, \dot{e}_v, \omega_d, \dot{\omega}_d) \in \mathbb{R}^3$ are defined as follows

$$\psi = \tilde{Y} + Y_d \tilde{\theta} + \tilde{\tau}_d^* \quad (70)$$

$$\tilde{Y} = Y \theta - Y_d \theta \quad (71)$$

Based on the same assumptions given for the inequality in Equation (50), the mismatch term $\psi(e_v, e_0, \dot{e}_v, \omega_d, \dot{\omega}_d) \in \mathbb{R}^3$ can be upper bounded in the sense that

$$\|\psi\| \leq \rho_3(e_v, e_0, \dot{e}_v, \omega_d, \dot{\omega}_d) + \rho_4(\cdot) = \rho_5(\cdot) \quad (72)$$

where $\rho_5(\cdot) \in \mathbb{R}$ denotes positive bounding constant and ρ_3, ρ_4 are positive, scalar, known bounding functions related with the parameter estimation error and the disturbance estimation error with residuals respectively.

Theorem 2: Given the closed-loop error dynamics in Equation (69), the robust control law proposed in Equation (66) ensures uniformly ultimately bounded attitude tracking in the sense that

$$\|e_v(t)\| \rightarrow \gamma_4 \exp(-\gamma_5 t) + \gamma_6, \quad \gamma_4, \gamma_5, \gamma_6 \in \mathbb{R} \quad (73)$$

provided that the initial conditions are selected to satisfy

$$e_0(0) \neq 0 \quad (74)$$

Proof: To prove Theorem 2, nonnegative function $V_2(t) \in \mathbb{R}$ is defined as

$$V_2 = \frac{1}{2} [e_v^T e_v / (1 - e_v^T e_v)] + \frac{1}{2} r^T J^* r \quad (75)$$

Using similar mathematical manipulations presented in the previous section, the time derivative of the function $V_2(t)$ can be obtained as follows:

$$\dot{V}_2 = -\frac{e_v^T \alpha e_v}{(1 - e_v^T e_v)^2} - r^T K r - r^T v_r + r^T \psi \quad (76)$$

Equation (76) can be upper bounded as

$$\dot{V}_2 \leq -\beta \|z\|^2 + \rho_5 \|r\| - \frac{\rho_5^2 \|r\|^2}{\rho_5 \|r\| + \varepsilon} \quad (77)$$

where $z(t)$ is defined in Equation (58). The above inequality can be further bounded as follows:

$$\dot{V}_2 \leq -\sigma V_2(t) + \varepsilon \quad (78)$$

The solution of the resulting linear differential inequality is

$$V_2(t) \leq V_2(0) \exp(-\sigma t) + \frac{\varepsilon}{\sigma} [1 - \exp(-\sigma t)] \quad (79)$$

Boundedness of the error signals and the control torque input can be shown by a similar arguments used in the previous

section. From Equations (57) and (79), it can be concluded that

$$\|z\|^2 \leq \frac{\lambda_2}{\lambda_1} \|z(0)\|^2 \exp\{-\sigma t\} + \frac{\varepsilon}{\sigma \lambda_1} \quad (80)$$

Hence, the objective presented in Equation (73) is achieved.

VI. SIMULATION RESULTS

In this section, simulation results are presented to illustrate the performances of the proposed control methods presented in Equation (45) and (66). The inertia matrix of the satellite is selected as follows:

$$J = \begin{bmatrix} 20 & 1.2 & 0.9 \\ 1.2 & 17 & 1.4 \\ 0.9 & 1.4 & 15 \end{bmatrix} \text{ kg m}^2 \quad (81)$$

The initial attitude of the satellite is selected to be

$$q_0(0) = 0.9486 \quad q_v(0) = [0.1826 \quad 0.1826 \quad 0.1826]^T \quad (82)$$

To have a smooth rotation, the desired trajectory was set according to the following desired angular velocity

$$\omega_d = 0.05 [\cos(0.1t) \quad \cos(0.1t) \quad \cos(0.1t)]^T \text{ rad/s} \quad (83)$$

The followings are the initial values of the desired quaternion

$$q_{0d}(0) = 1 \quad q_{vd}(0) = [0 \quad 0 \quad 0]^T \quad (84)$$

The external disturbances are set to be

$$\tau_d = 0.2 [\sin(t) \quad \sin(t) \quad \sin(t)]^T \text{ Nm} \quad (85)$$

Sensor noise is assumed to be zero mean Gaussian noise with 0.004 variance. Estimates of the inertia matrix and the disturbance vector are set to

$$\hat{J} = 0.7J \quad \hat{\tau}_d = 0.2\tau_d \quad (86)$$

The followings are the values of the control gains that are tuned by trial and error until a satisfactory performance is obtained

$$K = \alpha = \text{diag}\{5 \quad 5 \quad 5\} \quad \varepsilon = 0.04 \quad \rho = \rho_5 = 7 \quad (87)$$

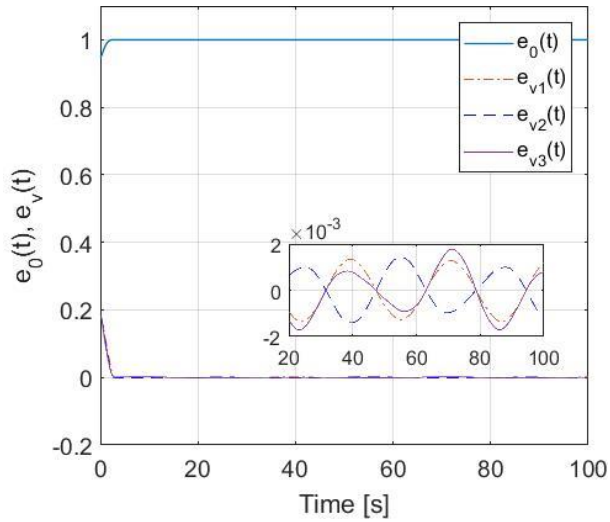


Figure 1. Controller I quaternion tracking errors (parametric uncertainties + disturbance)

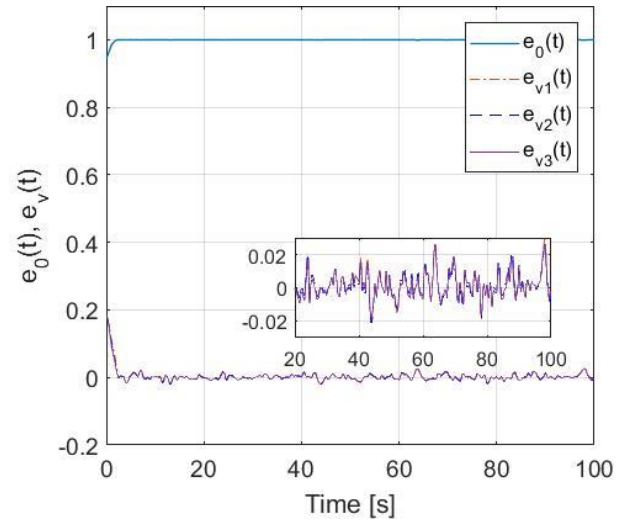


Figure 4. Controller I quaternion tracking error (parametric uncertainties+disturbance+sensor noise)

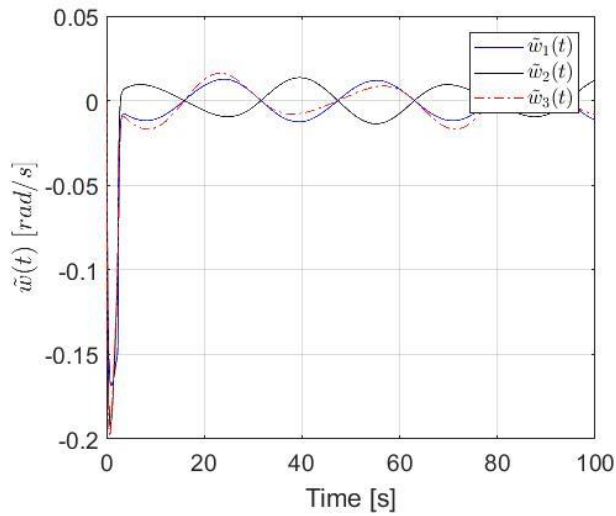


Figure 2. Controller I angular velocity errors (parametric uncertainties + disturbance)

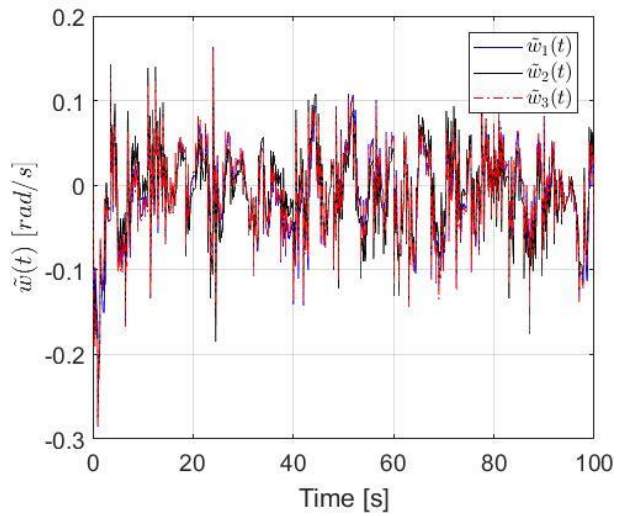


Figure 5. Controller I angular velocity errors (parametric uncertainties + disturbance + sensor noise)

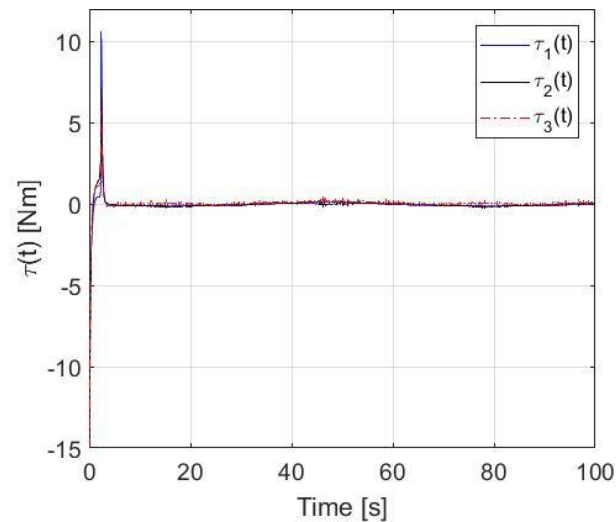


Figure 3. Controller I control input torques (parametric uncertainties + disturbance)

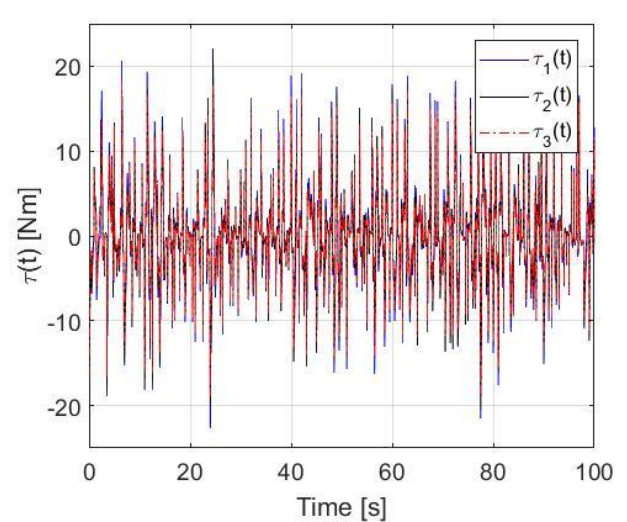


Figure 6. Controller I control input torques (parametric uncertainties + disturbance + sensor noise)

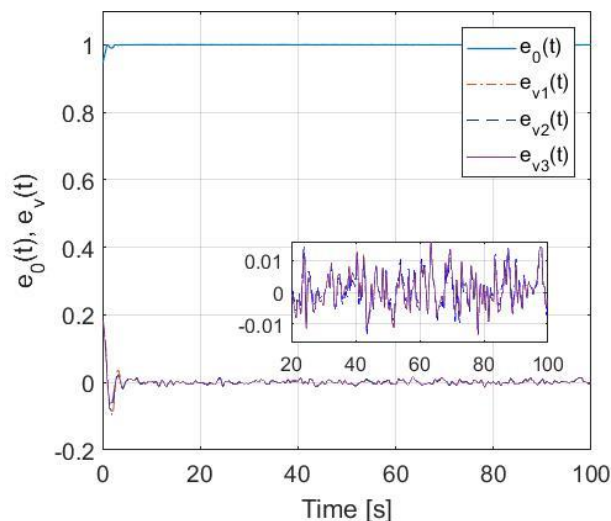


Figure 7. Controller II quaternion tracking errors (parametric uncertainties+disturbance+sensor noise)

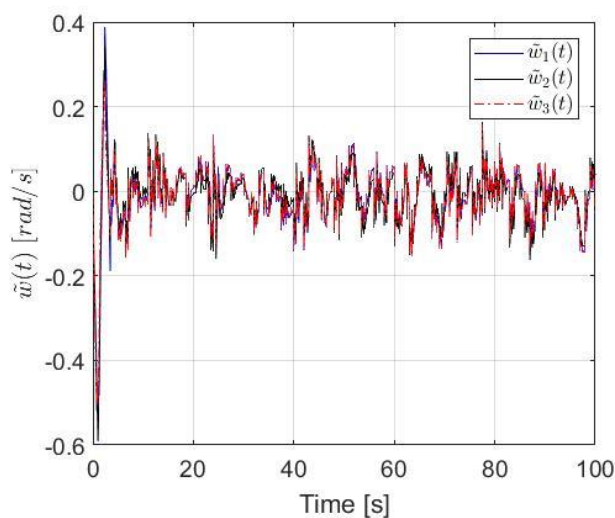


Figure 8. Controller II angular velocity errors (parametric uncertainties+disturbance+sensor noise)

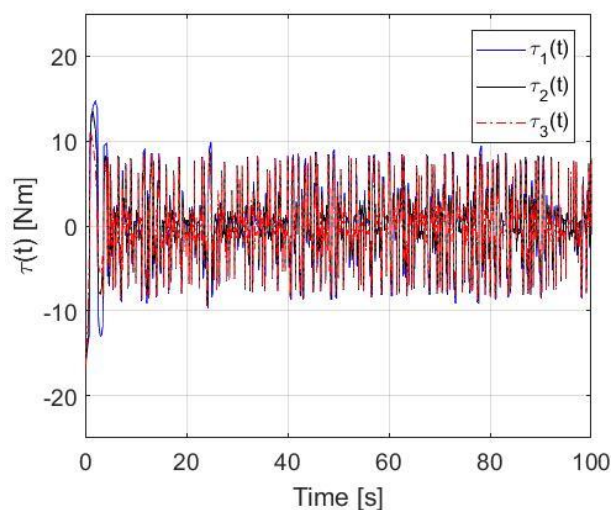


Figure 9. Controller II control input torques (parametric uncertainties+disturbance+sensor noise)

In the first part of the simulation studies, the former robust control method was examined under parametric uncertainties and disturbance effects. Fig. 1 illustrates the quaternion errors of the satellite. Angular velocity errors and the applied control input signals that belong to the same control structure are presented in Figs. 2 and 3 respectively. From Figs. 1 and 2, it can be seen that the control objective stated in the first Theorem was achieved with satisfactory performance and Fig. 3 shows that the control input signals do not exceed 0.5 Nm after 5s. In the second part of the simulation studies, to compare their performances, both control algorithms were run in the presence of parametric uncertainties, external disturbance and sensor noise. Figs. 4-6 shows the results of the conventional robust controller presented earlier and Figs. 7-9 belong to the reformulated control method. From the Figs. 7-9, it was seen that the reformulated robust control method acts quite better than the conventional robust controller and both the error signals and the applied control signals were relatively reduced. During the simulation studies, it has been observed that the advantages of the second controller become more apparent in the case of increased sensor noise.

VII. CONCLUSION

In this paper, two quaternion-based robust control method to solve the attitude tracking control problem of satellite were introduced. The first one is a conventional high-frequency robust control mechanism. It was shown that under parametric uncertainties and extern disturbance effects, it achieves well and provides uniformly ultimately bounded tracking result. However, in case of a sensor noise the controller performance was severely affected. The robust controller was then reformulated to reduce the effects of sensor contamination with less on-line computational requirement. As a future work, a new robust control mechanism can be developed to meet less sensor measurement requirements with a higher performance

REFERENCES

- [1] G. Meyer, *Design and Global Analysis of Spacecraft Attitude Control Systems*, NASA TR R-361, March 1971.
- [2] J. Y. Wen, K. Kreutz-Delgado, *The Attitude Control Problem*, IEEE Transactions on Automatic Control, vol. 36, no. 10, pp. 1148-1162, 1991.
- [3] N. A. Chaturverdi, A. K. Sanyal, N. H. McClamroch, *Rigid-body Attitude Control*, IEEE Control Systems Magazine, vol. 31, no. 3, pp 30-51, 2011.
- [4] M. D. Shuster, *A Survey of Attitude Representations*, Journal of Astronautical Sciences, vol. 41, no.4, pp.439-517, 1993.
- [5] Y. Bai, J. D. Biggs, F. B. Zazzera, N. Cui, *Adaptive Attitude Tracking with Active Uncertainty Rejection*, Journal of Guidance, Control, and Dynamics, vol. 41, no. 2, pp. 550-558, 2018.
- [6] D. Thakur, S. Srikant, M. R. Akella, *Adaptive attitude-Tracking Control of Spacecraft with Uncertain Time-Varying Inertia Parameters*, Journal of Guidance, Control, and Dynamics, vol. 38, no. 1, pp. 41-52, 2015.
- [7] L. Cao, X. L. Chen, Y. Zhao, *Minimum Sliding Mode Error Feedback Control for Fault Tolerant Small Satellite Attitude Control*, Advances in Space Research, vol. 53, no.2, pp. 309-324, 2014.
- [8] A. Sofyali, E. M. Jafarov, *Integral Sliding Mode Control of Small Sattelite Attitude Motion by Purely Magnetic Actuation*, IFAC Proc. Volumes, vol. 47, no.3, pp. 7947-7953, 2014.
- [9] Z-G. Zhou, Y-A. Zhang, X-N. Shi, D. Zhou, *Robust attitude tracking for Rigid Spacecraft with Prescribed Transient Performance*, Int. Journal of Control, vol. 90, Iss. 11, 2017.
- [10] A. Safa, M. Baradarannia, H. Kharrati, S. Khanmohammadi, *Robust Attitude Tracking Control for a Rigid Spacecraft Under Input Delays and Actuator Errors*, Int. Journal of Control, vol. 0, Iss. 0, 2017.

- [11] V. Utkin, J. Guldner, J. Shi, *Sliding Mode Control in Electromechanical Systems*, PA, Philadelphia, 1999.
- [12] J. P. Hespanha, D. Liberzon, A. S. Morse, *Overcoming The Limitations of Adaptive Control by means of Logic-based Switching*, Syst. Contr. Lett., vol. 49, no. 1, pp. 49-65, 2003.
- [13] P. A. Ioannou, J. Sun, *Robust Adaptive Control*, NJ, Upper Saddle River: Prentice-Hall, 1996.
- [14] H. Gui, G. Vukovich, *Global Finite-time Attitude Tracking via Quaternion Feedback*, Syst. Contr. Lett., vol. 97, pp. 176-183, 2016.
- [15] S. Wu, G. Radice, Y. Gao, Z. Sun, *Quaternion-based Finite-time Control for Spacecraft Attitude Tracking*, Acta Astronautica, vol. 69, n0. 1, pp. 48-58, 2011.
- [16] K. Lu, Y. Xia, *Finit-time Fault-Tolerant Control for Rigid Spacecraft with Actuator Saturations*, IET Control Theory & Appl., vol. 7, n0. 11, pp. 1529-1539, 2013.
- [17] A. Behal, W. Dixon, D. M. Dawson, B. Xian, *Lyapunov-Based Control of Robotic Systems*, CRC Press, 2010.
- [18] M. Wood, W. H. Chen, *Attitude Control of Magnetically Actuated Satellites with an uneven Inertia Distribution*, Aerospace Science and Technology, vol. 25, pp. 29-39, 2013
- [19] B. T. Costic, D. M. Dawson, M. S. d. Queiroz, V. Kapila, *Quaternion-Based Adaptive Attitude Tracking Controller Without Velocity Measurements*, Journal of Guidance, Control and Dynamics, vol. 24, no. 6, pp. 1214-1222, 2001.
- [20] B. Wie, *Spacecraft Vehicle Dynamics and Control*, AIAA, 1998.
- [21] P. C. Hughes, *Spacecraft Attitude Dynamics*, Wiley, 1986.
- [22] W. E. Dixon, A. Behal, D. M. Dawson, S. Nagarkatti, *Nonlinear Control of Engineering Systems: A Lyapunov-Based Approach*, MA, Boston: Birkhuser, 2003.

BIOGRAPHIES



JANSET DASDEMİR, received the B.S. degree from the Electrical Engineering Department, Yildiz Technical University, Istanbul, Turkey in 2000, and the M.Sc. and Ph.D. degrees from the same university, in 2002 and 2008 respectively. She was a Post-Doctoral Researcher at LSS-CNRS, France. She is currently involved in research with the Department of Control and Automation Engineering, YTU, Turkey, as an Assistant Professor. Her research interests include robust/adaptive control of non-linear systems, partial state feedback and output feedback

control and cooperative control.

A GaN-Based Synchronous Buck Converter for High Power Laser Diode Drive Applications

A. Ugur, and M. Yilmaz

Abstract—Laser Diodes are the essential components for development of high power laser systems. To operate these devices, highly efficient and high power density, compact, current regulated switching converters are necessary. In this paper, Gallium Nitride (GaN) based synchronous buck converters are studied for the application of laser diode driver. For this purpose, two synchronous buck converters one with Si-based the other one with GaN-based are designed, simulated, tested and compared. With the application of GaN-based semiconductors, 96.6% efficiency and 9.1 W/cm³ power density is achieved for 11A, 28V load at 700 kHz operating frequency.

Index Terms—High power laser diode, Synchronous buck converter, GaN Transistor, power density, efficiency.

I. INTRODUCTION

HIGH POWER LASER SYSTEMS has an increasing demand in several areas such as material processing, drilling, manufacturing, defense applications and consumer electronics. For these systems high-power Continuous Wave (CW) fiber lasers are the ideal technology because of several reason including high efficiency, high reliability, compactness, low cost and simplicity. Due to their advantages, high power fiber lasers are not only replacing other laser systems but also non-laser systems in many applications [1]. On the other hand, fiber lasers are the coherent photon sources based on the excitation of gain medium (doped fiber) with diode pumps namely laser diodes [2]. Therefore; for high power single mode CW fiber laser pumping, high power and high brightness laser diodes are required.

Over the last decades, laser diodes with wavelength from 0.8 μ m to 1 μ m have improved significantly in terms of electrical-to-optical efficiency and compactness [3]. Today, laser diode modules available on the market are capable of 200W optical power output with efficiency up to 65% in very compact packages. On the other hand, although \$/W for laser diode modules decreased significantly lately, a module over 100W optical power still might cost more than 2,000\$.

A. UGUR, is with Department of Electrical Engineering, University of Istanbul Technical University, Istanbul, Turkey, (e-mail: ugurab@itu.edu.tr) 

M. YILMAZ, is with Department of Electrical Eng., University of Istanbul Technical University, Istanbul, Turkey, (e-mail: myilmaz@itu.edu.tr) 

Manuscript received October 16, 2017; accepted January 4, 2018.

DOI: [10.17694/bajece.402018](https://doi.org/10.17694/bajece.402018)

Therefore using reliable drivers for these expensive devices is especially important. Electrically, laser diodes behave like LEDs with higher turn-on threshold voltage therefore driving low power laser diodes is similar to LED drivers. For low power laser diodes, a regulator operating amplifier which controls the current flowing through the laser diode via a sense resistor can be used. A simplified circuitry of a low power laser diode driver is shown in Fig. 1. High power laser diodes on the other hand, are similar to series LED strings applications where switching regulators are necessary to improve efficiency. Buck converters which are used in the industry up to kW power range are ideal for such applications due to the output filter inductor.

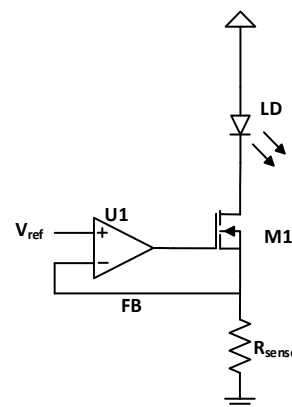


Fig. 1. Simplified circuit for low power laser diode driver

In recent years, switching devices using wide-bandgap (WBG) semiconductor materials such as Gallium Nitride (GaN) and Silicon Carbide (SiC) are improved significantly [4]-[6]. These devices offer very attractive characteristics such as high frequency switching and low on-state resistance which are crucial to achieve compact very efficient power converters. For this reason in this study, synchronous buck converters with GaN and Si based switching devices are designed and compared to understand the feasibility of GaN transistors for laser diode driving applications.

The structure of this paper is as follows: In Section II, the electrical characteristics of laser diodes are studied and the current/voltage requirements are determined. In Section III, the converter designs are presented. This part includes the basics of synchronous buck converter, circuit design, loss estimations of the GaN and Si based devices. In Section IV, the experimental results are shown; performances of the designed converters are compared and evaluated.

II. LASER DIODES

As it was stated, high power laser diodes are essential components for high power laser systems. The current laser diode technology is based on combining multiple emitter semiconductor chips. The performance and rated power summary of several laser diode modules can be found in [7]. Although there are many different high power laser diode modules exist in the market, for simplicity in this study, a 976 nm 90W laser diode module (Fig. 2) for which the test data given in Fig. 3 is taken as a reference.



Fig. 2. 976nm, 90W fiber coupled laser diode module [8]

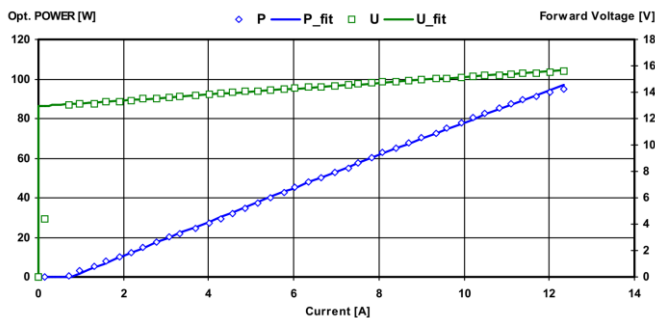


Fig. 3. Test data of a 976nm, 90W fiber coupled laser diode module [8].

The electrical characteristics of such module can be modelled as in Fig. 4, where V_{th} (12.94V) is the threshold voltage and R_s (0.22Ω) is the on resistance of the device [8]. The rated voltage and current values are given as 15.5V and 11.5A respectively which corresponds to 50% electrical-to-optical efficiency.

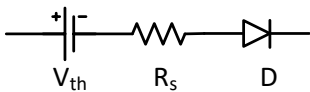


Fig. 4. Electrical model for a high power laser diode module.

Based on these considerations, for the application in this study the power ratings of the converters to be designed is determined as up to 11A/300W output, which covers the electrical needs of many laser diode modules currently available on the market. Specifications of the load assumption are on Table 1.

TABLE I. SPECIFICATIONS OF THE LOAD ASSUMPTION

Rated Current	11 A
Rated Voltage	27 V
Threshold Voltage of the load (V_{th})	21.5 V
On Resistance of the load (R_{on})	0.5 Ω

III. CONVERTER DESIGN

A. Synchronous buck converter basics

Synchronous buck converters are used to step down voltages from higher level to lower level. Basic schematic is given in Fig. 5. The operation principle is as follows: the Q_1 MOSFET is connected to input voltage. When it is turned-on, the current flows from input to output, the current of the inductor increases and energy stored in the inductor. During this time Q_2 MOSFET is off. When Q_1 is turned-off and Q_2 is turned-on, the current flows through Q_2 in reverse direction, the current on the inductor decreases and some of the energy stored on the inductor is transferred to the load. The basic waveforms are given in Fig. 6.

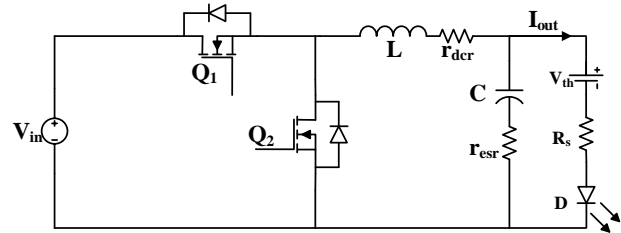


Fig. 5. Synchronous buck converter

The difference between the non-synchronous and synchronous buck converters is that the low side switch is a diode in non-synchronous one whereas it is transistor in the synchronous buck. Since in synchronous buck converter reverse current flow is allowed, efficiency is low compared to non-synchronous buck converter at light load. On the other hand at heavy load, synchronous buck converters have better efficiency due to low conduction losses in the low side switching device, and are preferred over traditional buck converter especially in the applications where the converter is expected to operate with heavy load.

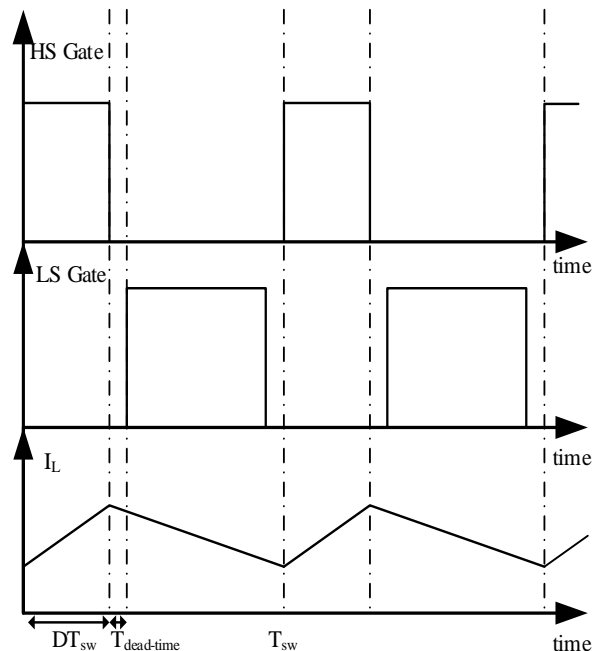


Fig. 6. Synchronous buck converter basic waveforms

B. Consideration of GaN and Si based switching devices

Since there are many parameters which effect the performance of a converter, it is not an easy case to select the transistors. Main performance measures for selecting the semiconductors are the power loss and power dissipation capability. One simple way to compare the semiconductors and to determine the most suitable ones is to use Figure of Merit (FOM). For power converters, the loss is directly related with the on resistance ($R_{DS(on)}$) and gate charge (Q_g) of the transistors. Therefore, comparison of $Q_g \times R_{DS(on)}$ FOM for transistors provide a good measure to estimate performance of the converter with different transistors. In Table 2, comparison of several parameters for the GaN transistor and Si-MOSFETs which are used in this study are given.

TABLE II. COMPARISON OF GaN AND SI BASED SWITCHING DEVICES IMPLEMENTED IN THIS STUDY

	GS61008P	SiJ478DP (HS)	SiJ482DP (LS)
V_{DS}	100V	80V	80V
I_D	90A	60A	60A
$R_{DS(on)}$ ($V_{GS} = 6V$, $T_J = 25^\circ C$)	7 m Ω	7 m Ω	6 m Ω
Normalized on-state resistance ($T_J = 125^\circ C$)	2	1.6	1.6
Q_g ($V_{GS} = 6V$, $T_J = 25^\circ C$, $V_{DS} = 50V$)	12 nC	22 nC	24 nC
Reverse recovery charge (Q_r)	-	36 nC	44 nC
Junction-to-case thermal resistivity (R_{thJC})	0.55 $^\circ C/W$	1.5 $^\circ C/W$	1.3 $^\circ C/W$
Reverse conduction voltage (V_{SD})	2V	0.76V	0.73V

Although the rated voltage and current values are higher for the selected GaN transistor, it has better $Q_g R_{DS(on)}$ FOM compared the Si MOSFETs. As for $R_{DS(on)}$, Si and GaN transistors have similar values at $25^\circ C$ when the gate voltage is 6V. On the other hand, $R_{DS(on)}$ is highly related with the applied V_{GS} voltage. For Si-MOSFETs the conduction losses can be decreased by applying higher turn-on gate voltages, although this leads some more gate drive and switching losses. Unlike Si-MOSFETs, higher gate voltages are not possible for GaN since the absolute maximum gate voltage is specified 7V for these devices. One important point is that, the normalized on-state resistance of GaN transistor selected for this study is higher than the Si counterparts, so at high temperatures, the conduction losses are expected to be higher for GaN transistors.

On the other hand, the gate charge of the GaN transistor is significantly lower than the Si-MOSFETs, which leads lower switching losses, and enables operating at higher frequency.

E-mode GaN transistors do not need intrinsic body diode, therefore reverse recovery losses do not exist. However, in reverse direction GaN transistors have channel resistance which can be modelled as a body diode and this leads higher losses during the dead-time [9]. Therefore dead-time optimization is an important task for these devices. An analysis of the dead-

time for GaN can be found in [10]. In this study two different dead-time is implemented to see the effect of the dead-time to GaN-based prototype.

C. Loss Estimation

In a synchronous buck converter the major losses are as follows:

- High side MOSFET conduction loss
- Low side MOSFET conduction loss
- High side MOSFET switching loss
- High side MOSFET gate charge loss
- High side MOSFET output capacitance loss
- Reverse recovery loss
- Dead-time loss
- Inductor loss

The losses can be estimated by using switching device datasheets [11], [12]. Conduction losses are result of the on-state resistances and can be calculated via Eq. (1) and Eq. (2) for high side and low side transistors.

$$P_{cond_HS} = R_{DS(on)_HS} \times I_{Drms_HS}^2 \quad (1)$$

$$P_{cond_LS} = R_{DS(on)_LS} \times I_{Drms_LS}^2 \quad (2)$$

I_{Drms} is the drain to source RMS current flowing through the MOSFETs and can be approximated as $I_{out} D$ for I_{Drms_HS} and $I_{out} (1-D)$ for I_{Drms_LS} . As on-state resistance increases with temperature, usually iterative calculations are applied. For this study, the maximum operating temperature on-state resistance values are used for a safe estimation.

The switching transitions of the MOSFET during the turn-on are given in Fig. 7.

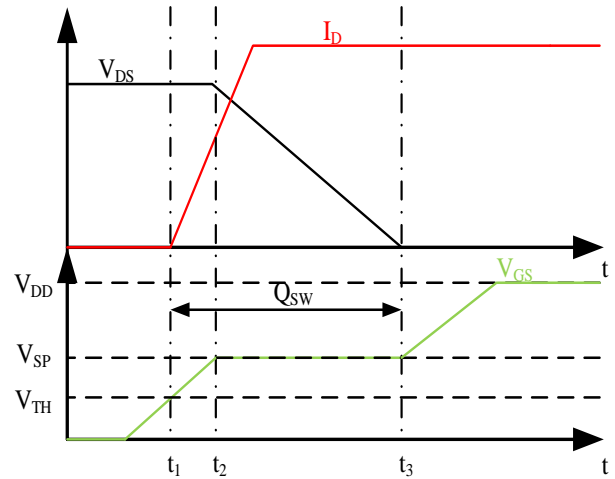


Fig. 7. Switching transitions of a typical MOSFET during turn-on High side MOSFET switching losses can be calculated by using switching gate charge (Q_{Gsw}) and gate currents (I_G) as in Eq. (3).

$$P_{swHS} = \frac{V_{IN} \times I_{OUT}}{2} \times f_{sw} \times \left(\frac{Q_{Gsw}}{I_{GLH}} + \frac{Q_{Gsw}}{I_{GHL}} \right) \quad (3)$$

I_{GHL} and I_{GLH} are the gate currents for high-to-low and low-to-high transitions, respectively. Generally low-side MOSFET switching loss is neglected as it is low compared to other losses.

Gate charge loss of the high side MOSFETs is expressed as in Eq. (4).

$$P_{GHS} = Q_G \times V_{Gate} \times f_{sw} \quad (4)$$

where Q_G is total gate charge and V_{Gate} is the driver's gate voltage. Loss due to the output capacitance (C_{OSS}) of the high-side switching device can be calculated with Eq. (5).

$$P_{COSS} = C_{OSS} \times V_{IN}^2 \times f_{sw} / 2 \quad (5)$$

The reverse recovery loss is calculated by using the reverse recovery charge (Q_{RR}) via Eq. (6).

$$P_{DRR} = Q_{RR} \times V_{IN} \times f_{sw} \quad (6)$$

The dead-time loss is calculated via Eq. (7).

$$P_{DT} = T_d \times V_{SD} \times f_{sw} \times I_{OUT} \quad (7)$$

Here T_d is dead-time, V_{SD} is reverse voltage on the low-side MOSFET when both switches are off.

Finally, the inductor loss is a result of equivalent series resistance of the inductor ($R_{ESR(L)}$) and described as in Eq. (8).

$$P_{Ind} = R_{ESR(L)} \times I_{OUT}^2 \quad (8)$$

Then total loss of the converter can be expressed as in Eq. (9).

$$P_{TOTAL} = P_{cond_HS} + P_{cond_LS} + P_{sw_HS} + P_{GHS} + P_{DRR} + P_{DT} + P_{COSS} + P_{Ind} \quad (9)$$

D. Specifications of the Converters

The selection of the size of the inductor is straight forward and can be calculated for 30% peak-to-peak ripple current at maximum current via Eq. (10). The converters are designed for an operating frequency 500 kHz.

$$L = \frac{V_{OUT} \times (V_{IN} - V_{OUT})}{0.3 \times I_{OUT} \times V_{IN} \times f_{sw}} \quad (10)$$

The output capacitor size has been selected for a 1% output current ripple (I_{ripple}). This ripple corresponds to $I_{ripple} R_s$ voltage ripple (V_{ripple}) at the output. The maximum ESR of the capacitor is calculated with Eq. (11).

$$R_{cap_esr} = \frac{V_{ripple}}{I_{OUT}} \quad (11)$$

This is the maximum ESR value for ripple selection. The output capacitance can be calculated by using Eq. (12).

$$C_{OUTmin} = \frac{\Delta I_L}{8 \times I_{OUT} \times f_{sw} \times V_{ripple}} \quad (12)$$

Based on these considerations, 6.8uH inductor and 2x10uF ceramic capacitors at the output have been selected. Using ceramic capacitors has two advantages: first, they occupy less space on PCB which helps size reduction; second, low ESR reduces the output ripple. The details of the designed converters are given in Table 3.

TABLE III. SPECIFICATIONS OF THE DESIGNED CONVERTERS

	Si-Si synchronous buck converter	GaN-GaN synchronous buck converter
HS transistor	Sij478DP	GS61008P
LS transistor	Sij482DP	GS61008P
Inductor	6.8uH	6.8uH
Output Capacitor	2 x 10uF	2 x 10uF
Gate Driver	UCC27211	LM5113
Gate Voltage	12V	5V
Gate Resistors	4.7	$R_{on}=4.7, R_{off}=1$

In Fig. 8, the LT-Spice simulation model has been given. In the simulation model, the capacitor and inductor ESR values have been included with small parasitic inductances on the high di/dt loop. As it can be seen from Fig. 9, the current ripple on the laser diode is below 1% with and the inductor current ripple is around 30%.

E. Efficiency comparison of GaN and Si based synchronous buck converters

Efficiency comparison has been done at 60% duty cycle operation and for 11A output current.

For Si-Si based synchronous buck converter 97.7% and 97.3% efficiency has been calculated for 400 kHz and 500 kHz operation respectively and the distribution of the calculated loss has been shown in Fig. 10. Note that, the dead-time has been taken as 20 ns for this converter.

For GaN-GaN based synchronous buck converter estimated efficiency for 10 ns and 20 ns dead-time has been given Table 4. For this converter, the distributions of the losses are given in Fig. 11 and Fig. 12.

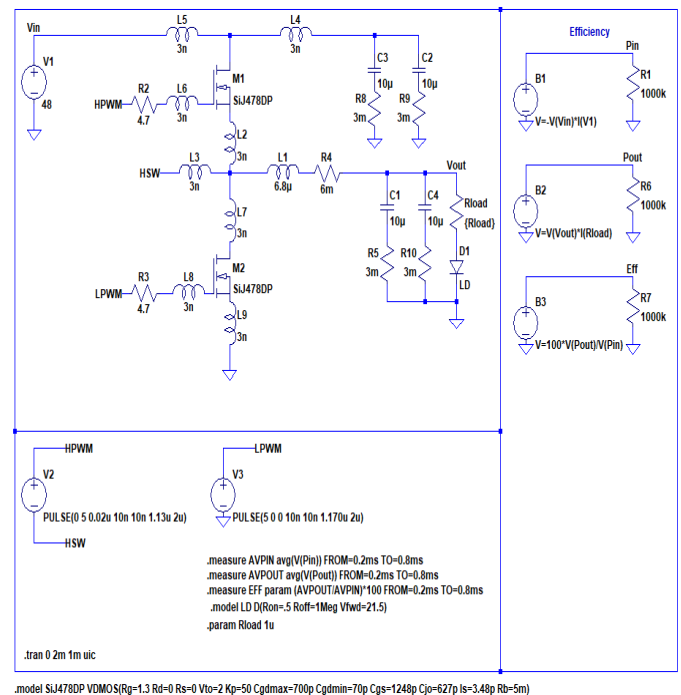


Fig. 8. Simulation model of the synchronous buck converter

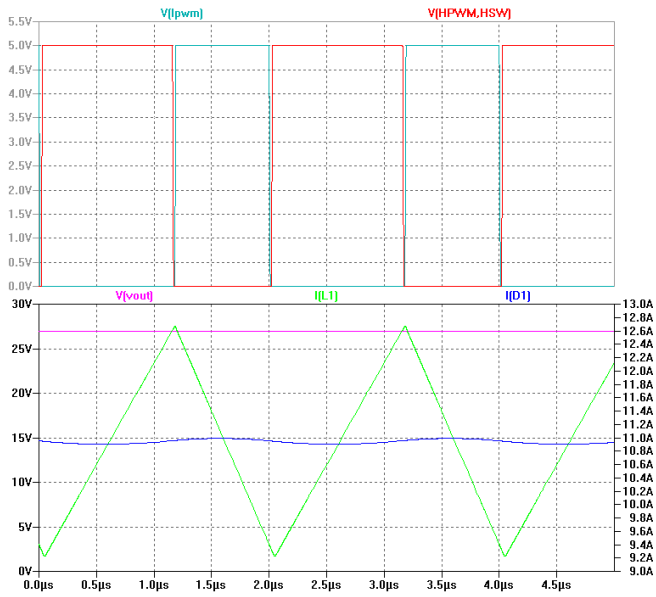


Fig. 9. Simulation results of the synchronous buck converter

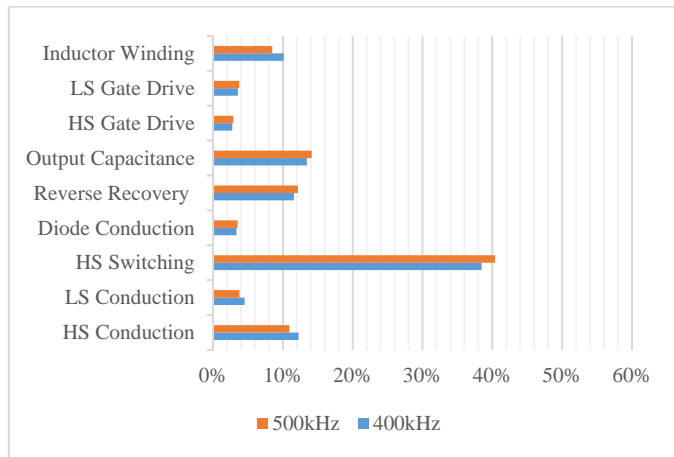


Fig. 10 Si-Si synchronous buck converter estimated loss distribution.

TABLE IV. CALCULATED EFFICIENCY FOR GaN-GaN BASED SYNCHRONOUS BUCK CONVERTER

Frequency [kHz]	Dead-time [ns]	Calculated Efficiency
400	20	98.3%
500	20	97.9%
600	20	97.6%
700	20	97.4%
400	10	98.2%
500	10	97.8%
600	10	97.5%
700	10	97.2%

According to the calculations slightly better efficiency is expected in GaN-based prototype due to reduced switching charge of GaN transistors. Please note that, as expected diode conduction loss is more in GaN-based synchronous buck converter, although its effect to the total loss has been reduced with 10 ns dead-time as in Fig. 12.

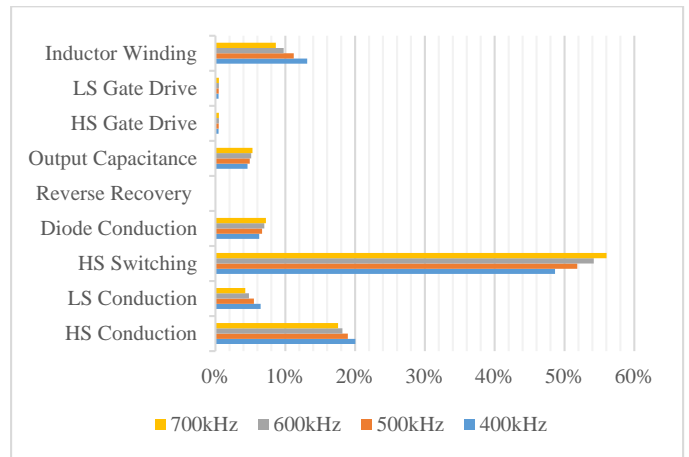


Fig. 11. GaN-GaN synchronous buck converter estimated loss distribution with 20ns dead-time

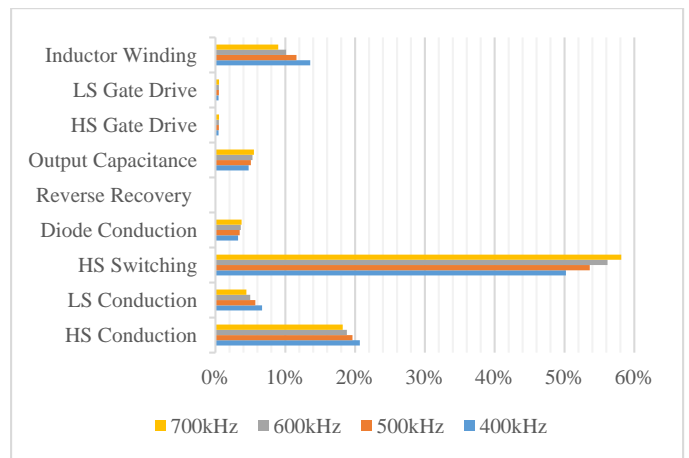


Fig. 12. GaN-GaN synchronous buck converter estimated loss distribution with 10ns dead-time.

IV. EXPERIMENTAL RESULTS

The converters are designed on very compact 30x100x1mm PCBs (Fig. 13) based on the specifications given in Table 3. During the tests forced air cooling is applied with fans. A photo of the test bench can be seen on Fig. 14. An electronic load is used to output of the converters.

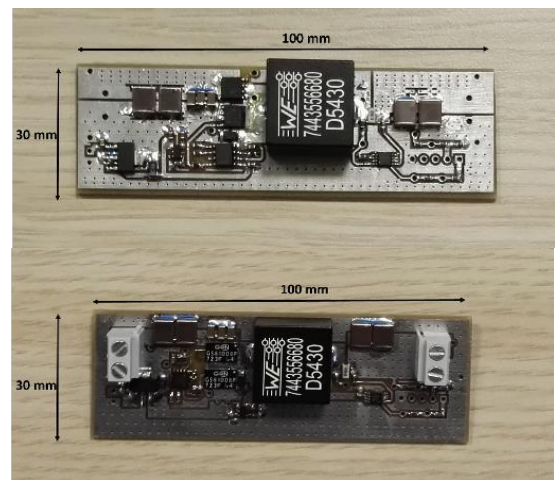


Fig. 13. Si-Si (Top) and GaN-GaN synchronous buck converter prototypes

The experimental results with 11A 60% duty cycle are shown in Table 5 for GaN-GaN prototype and in Table 6 for Si-Si prototype. At 400 kHz and 500 kHz very similar efficiency values have been measured which shows that at these frequencies Si-MOSFETs can still provide very good results in terms of efficiency. However, with the application of GaN switching devices, it is possible to implement higher operating frequencies. As it can be seen in Table 5 at 700 kHz with 10 ns 96.6% efficiency has been measured which is almost the same as in Si-based converter at 500 kHz.

On the other hand, as it can be seen in Fig. 15 and Fig. 16, the classical power loss estimation that is applied in this study provide limited results which suggests that the circuit parasitics are very effective although the circuit layout is designed as proposed in [13] and therefore should be taken into account for the cooling design.

Another observation is that for Gallium Nitride based prototype, the efficiency difference between 10 ns and 20 ns dead-time is up to 0.4%, which shows that dead-time optimization is necessary for these converters. In Fig. 17 and Fig. 18, the V_{DS} voltages of the high-side and low-side transistors are shown for different dead-time values. One important point is that although too long dead-time increases the losses, having too short can cause power input to ground short circuit which leads shoot through effect or can prevent the zero voltage turn-on of the low side MOSFET which results in reduced efficiency [10]. In this study, optimization of the dead-time is not considered however 10ns dead-time provided good results.

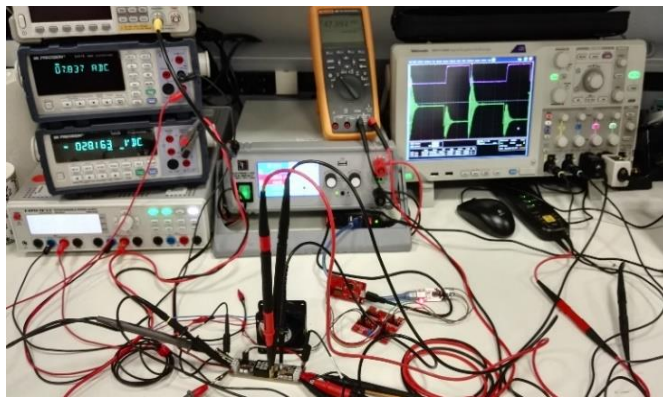


Fig. 14. Experimental setup

TABLE V. EXPERIMENTAL RESULTS OF THE GaN-GaN PROTOTYPE

Frequency [kHz]	Dead-time [ns]	Calculated Efficiency
400	20	97.0%
500	20	96.8%
600	20	96.6%
700	20	96.2%
400	10	97.4%
500	10	97.2%
600	10	97.0%
700	10	96.6%

TABLE VI. EXPERIMENTAL RESULTS OF THE SI-SI PROTOTYPE

Frequency [kHz]	Dead-time [ns]	Measured Efficiency
400	20	96.9%
500	20	96.7%

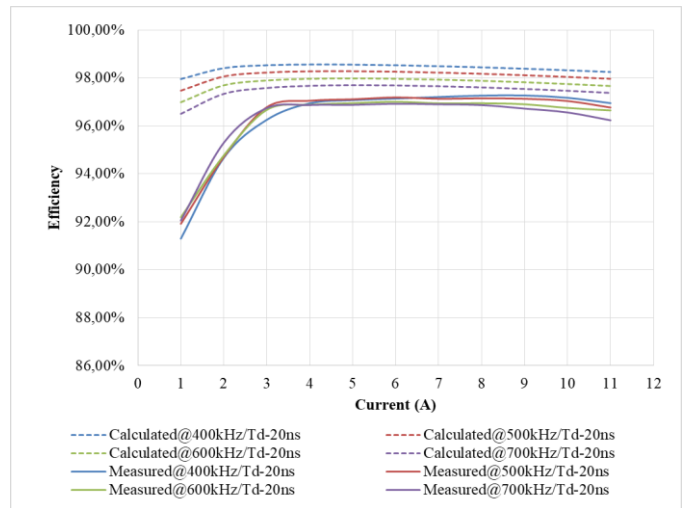


Fig. 15. Comparison of measured and calculated efficiencies for GaN-based synchronous buck converter with 20ns dead-time

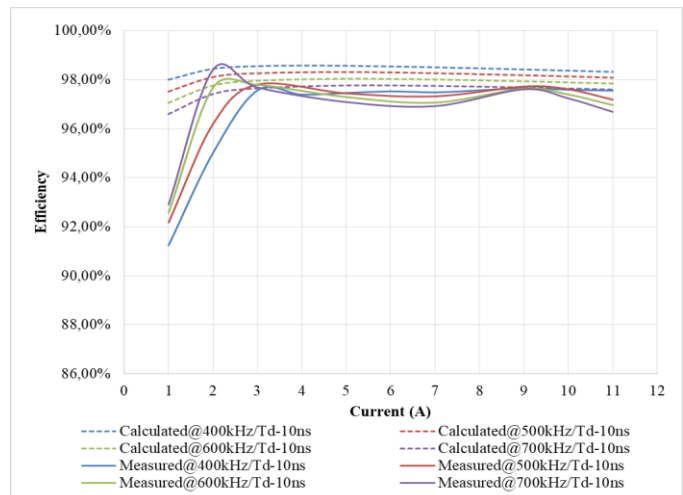


Fig. 16. Comparison of measured and calculated efficiencies for GaN-based synchronous buck converter with 10ns dead-time.



Fig. 17. GaN-based prototype high-side (green) and low-side (purple) V_{DS} voltage waveforms and overshoot at 500kHz/20 ns dead-time with 8A load.

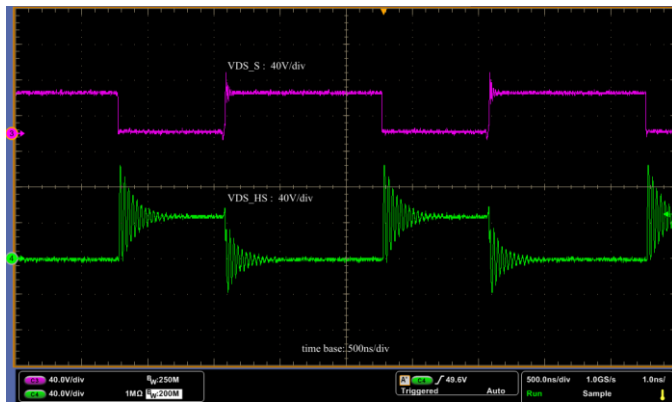


Fig. 18. GaN-based prototype high-side (green) and low-side (purple) V_{DS} voltage waveforms and overshoot at 500kHz/10 ns dead-time with 8A load.

V. CONCLUSION

In this study, compact, high efficient and power density synchronous buck converters are studied for high power laser diode drive applications. For this purpose, two synchronous buck converters one with Si-based the other one with GaN-based are designed, simulated, tested and compared. With the use of GaN switching devices, 96.6% efficiency at 700 kHz is measured and without cooling and control circuitry 9.1 W/cm³ power density is achieved for an 11A/300W prototype which can be used for most of the high power laser diodes on the market. On the other hand, it is seen that optimization of the dead-time is necessary for GaN based synchronous buck converters to reduce the losses. The results shows that, GaN transistors are very promising semiconductor devices and can promote efficiency of the synchronous buck converters for high power laser diode drive applications.

REFERENCES

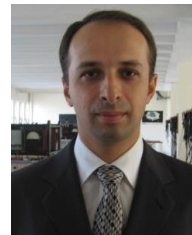
- [1] D.A.V. Kliner, "nLIGHT alta: A versatile next-generation fiber laser platform for kW materials processing", in *Proc. of the 84th Int. Conf. on Laser Mater. Process.*, Jan. 2016. pp. 1-7.
- [2] J. Wallace, "Photonics Products: High-power Fiber Lasers: Kilowatt-level fiber lasers mature", *Laserfocusworld.com*, 2018. [Online]. Available: <http://www.laserfocusworld.com>. [Accessed: 24- Jan- 2018].
- [3] L. Bao; J. Bai; K. Price; M. Devito; M. Grimshaw; W. Dong; X. Guan; S. Zhang; H. Zhou; K. Bruce; D. Dawson; M. Kanskar; R. Martinsen; J. Haden (2013). "Reliability of high power/brightness diode lasers emitting from 790 nm to 980 nm." in *Proc. of SPIE*, Vol. 8605, pp. 86050N-1.
- [4] J. Millan, P. Godignon, X. Perpina, A. Perez-Tomas, J. Rebollo, "A Survey of Wide Bandgap Power Semiconductor Devices," *IEEE Trans. Power Electron.*, vol. 29, no.5, pp. 2155-2163, May 2014.
- [5] M. Ishida, T. Ueda, T. Tanaka and D. Ueda, "GaN on Si Technologies for Power Switching Devices," *IEEE Trans. on Electron Devices*, vol. 60, no.10, pp.3053-3059, Oct 2013.
- [6] X. Huang, Z. Liu, Q. Li and F. C. Lee, "Evaluation and Application of 600V GaN HEMT in Cascode Structure," *IEEE Trans. Power Electron.*, vol. 29 no. 5, pp. 2453-2461, May 2014.
- [7] M. Kanskar, L. Bao, J. Bai, Z. Chen, D. Dahlen, M. DeVito, W. Dong, M. Grimshaw, J. Haden, X. Guan, M. Hemenway, K. Kennedy, R. Martinsen, J. Tibbals, W. Urbanek, S. Zhang (2014, March). "High reliability of high power and high brightness diode lasers", in *Proc. of SPIE*, March 2014, Vol. 8965, pp. 896508.
- [8] DILAS, "976nm, 90W, conduction-cooled, fiber-coupled diode laser module", www.dilas.com, 2018 [Online]. Available: http://dilas.com/assets/media/products/DILAS_SE_Module-976nm-90W_HS2-PM10_TD.pdf [Accessed:24-Jan-2018].
- [9] GaN Systems, "Bottom-side cooled 100V E-mode GaN transistor," GS61008P datasheet, Rev. 180111.

- [10] D. Han and B. Sarlioglu, "Deadtime Effect on GaN-Based Synchronous Boost Converter and Analytical Model for Optimal Deadtime Selection," *IEEE Trans. Power Electron.*, vol. 31, no. 1, pp. 601-612, Jan. 2016.
- [11] Fairchild, Appl. Note AN-6005.
- [12] Microchip, Appl. Note AN-1471.
- [13] D. Reusch and J. Styrdom, "Understanding the Effect of PCB Layout on Circuit Performance in a High-Frequency Gallium-Nitride-Based Point of Load Converter," *IEEE Trans. Power Electron.*, vol.29, no.4, pp.2008-2015, April 2014.

BIOGRAPHIES



ABDULKERIM UGUR, received the B.Sc. degree in Electrical and Electronics Engineering from Middle East Technical University, Ankara, Turkey, in 2009 and M.Sc. degree in Electrical Engineering from the Istanbul Technical University, Istanbul, Turkey in 2012. Currently he is a Ph.D. student at Istanbul Technical University. His research interests include power electronics and hardware design.



MURAT YILMAZ received the B.Sc. degree from Electrical Engineering Department, Istanbul Technical University (ITU), Istanbul, Turkey, in 1995 and the M.Sc. and Ph.D. degrees from the same university, 1995 and 2005, respectively.

He is currently an Assistant Professor at the Istanbul Technical University. His research interests power electronics and electrical machine design, control, optimization and reliability modeling in motor drives and electric drive vehicles including electric, hybrid and plug-in electric vehicles.

Publication Ethics

The journal publishes original papers in the extensive field of Electrical-electronics and Computer engineering. To that end, it is essential that all who participate in producing the journal conduct themselves as authors, reviewers, editors, and publishers in accord with the highest level of professional ethics and standards. Plagiarism or self-plagiarism constitutes unethical scientific behavior and is never acceptable.

By submitting a manuscript to this journal, each author explicitly confirms that the manuscript meets the highest ethical standards for authors and coauthors

The undersigned hereby assign(s) to *Balkan Journal of Electrical & Computer Engineering* (BAJECE) copyright ownership in the above Paper, effective if and when the Paper is accepted for publication by BAJECE and to the extent transferable under applicable national law. This assignment gives BAJECE the right to register copyright to the Paper in its name as claimant and to publish the Paper in any print or electronic medium.

Authors, or their employers in the case of works made for hire, retain the following rights:

1. All proprietary rights other than copyright, including patent rights.
2. The right to make and distribute copies of the Paper for internal purposes.
3. The right to use the material for lecture or classroom purposes.
4. The right to prepare derivative publications based on the Paper, including books or book chapters, journal papers, and magazine articles, provided that publication of a derivative work occurs subsequent to the official date of publication by BAJECE.
5. The right to post an author-prepared version or an official version (preferred version) of the published paper on an internal or external server controlled exclusively by the author/employer, provided that (a) such posting is noncommercial in nature and the paper is made available to users without charge; (b) a copyright notice and full citation appear with the paper, and (c) a link to BAJECE's official online version of the abstract is provided using the DOI (Document Object Identifier) link.



ISSN: 2147- 284X
Vol: 6
No:1
Year: February 2018

CONTENTS

- A. Tarhan, and M.A. Sağ,** , COSMIC Solver: A Tool for Functional Sizing of Java Business Applications, **1-8**
- A.Serbes,** A Method for Estimating Chirp Rate of a Linear Frequency Modulated Signal, **9-12**
- I.Turker,** Evaluation of the Turkish Highway Network Analysis with Traffic Data, . **13-19**
- O. Coşkun, and K. Avcı,** FPGA Schematic Implementations and Comparison of FIR Digital Filter Structures, **20-28**
- M. A. Şen, and M. Kalyoncu,** Optimal Tuning of PID Controller Using Grey Wolf Optimizer Algorithm for Quadraped Robot, **29-35**
- S. Muratoğlu Çürük,** Performance of MAP Channel Estimator in Power Line Communication with OFDM under Impulsive Noise, **36-41**
- N. Ekren,** Researches on Anti-reflection Coating (ARC) Methods Used in PV Systems, **42-46**
- S. Biricik,** Design of Unified Power Quality Conditioner for Power Quality Improvement in Distribution Network, **47-52**
- J. Dasedemir,** Quaternion-Based Robust Satellite Attitude Tracking Control, **53-61**
- A. Ugur, and M. Yilmaz,** A GaN-Based Synchronous Buck Converter for High Power Laser Diode Drive Applications, **62-68**

BALKAN JOURNAL OF ELECTRICAL & COMPUTER ENGINEERING

(An International Peer Reviewed, Indexed and Open Access Journal)

Contact

Istanbul Technical University
Department of Electrical Engineering,
Ayazaga Campus, Maslak, Istanbul-Turkey

Web: <https://www.bajece.com>
<http://dergipark.gov.tr/bajece>
e-mail: editor@bajece.com

